# $n(p)$-InP–$n$-$In_2O_3$–$P_2O_5$–Pd diode structures as potential sensors for near-infrared radiation, moisture, and hydrogen

S. V. Slobodchikov and Kh. M. Salikhov

*A. F. Ioffe Physicotechnical Institute, Russian Academy of Sciences, St. Petersburg*
(Submitted August 26, 1999)
Pis'ma Zh. Tekh. Fiz. **25**, 72–78 (December 26, 1999)

Diode structures based on $n(p)$-InP with intermediate $n$-$In_2O_3$ and $P_2O_5$ layers were fabricated by electrochemical deposition of Pd. It is shown that when exposed to pulses of water vapor the photo-emf of the structures varies by 60–400% and in the presence of $H_2$ it can vary by 1.5–2 orders of magnitude. These $n(p)$-InP–$n$-$In_2O_3$–$P_2O_5$–Pd structures are potential sensors for near-infrared radiation, moisture, and hydrogen. © *1999 American Institute of Physics.* [S1063-7850(99)02812-8]

The development of gas analyzers using various semiconductor diode structures is of considerable interest for monitoring systems in industry, agriculture, and ecology. In some of our previous studies we showed that changes in the photoelectric characteristics of the diode structures, such as the photo-emf, lead to a substantial improvement in the sensitivity of the sensor, particularly for the detection of hydrogen.[1–3]

In the present paper we report results of investigations of $n(p)$-InP-based palladium-contact diode structures as potential triple-purpose sensors, i.e., for detecting near-infrared radiation, moisture, and hydrogen.

The diode structures were fabricated using $n$-InP crystals with $n=1\times10^{16}\,\mathrm{cm}^{-3}$ and $p$-InP with $p=5\times10^{18}\,\mathrm{cm}^{-3}$. The preliminary stage involved the well-developed process of cold etching of the substrate surface. First, the surface was cleaned systematically with acetone, sulfuric acid, and an $H_2SO_4+H_2O_2+H_2O$ solution (1 min), it was then polished in Br (5%)+$CH_3COOH$ (95%) etchant, and these cleaning operations were then repeated. At the second stage the Pd was deposited electrochemically from an electrolyte containing $PdCl_2$, $Na_2PO_4\cdot12H_2O$, and $C_6H_5COOH$. The process was carried out at 5–60° and a current density of $1\,\mathrm{mA/cm}^2$ giving a Pd layer ~400Å thick. The Ohmic contacts were applied to the $n$-InP by electrochemical deposition of nickel and to the $p$-InP be deposition of Ag/Zn alloy.

It follows from the published data[4–6] that the important components of the intermediate layer between Pd and $n(p)$-InP are the oxides of indium and phosphorus: the first is the highly conducting semiconductor $n$-$In_2O_3$ having the band gap $E_G\approx3.6$ eV, and the second is an insulator with the postulated band gap $E_G=8$ eV. A structure containing the oxides $n$-$In_2O_3$ and $P_2O_5$ was also obtained by electrochemical etching in Ref. 6 and our previous studies of the electrical and photoelectric characteristics of these structures heat for a long time in air[7] identified the important role of these two oxides in the current transfer mechanism. The spectral photosensitivity of the structures (Fig. 1a) is determined by the photocarrier generation in the $n(p)$-InP substrate (Fig. 1b), i.e., embraces the spectral range $\lambda=0.6$–$1\,\mu$m with $\lambda_{max}=0.8\,\mu$m. The results of the pulsed action of water vapor and hydrogen were as follows.

For $n$-InP-based structures exposed to 0.5 ppm $H_2$ the photo-emf decreases by 1.5–2 orders of magnitude (curves *1* and *2* in Fig. 1). The pulsed action of water vapor increases the photo-emf by 100–400% when the humidity increases from 30% to 100%.

For the structures having a $p$-InP substrate the photo-emf increases by 200–300% under the action of an $H_2$ pulse (100%) whereas water vapor increases the photo-emf by 50–70% in the short- and long-wavelength parts of the spectrum

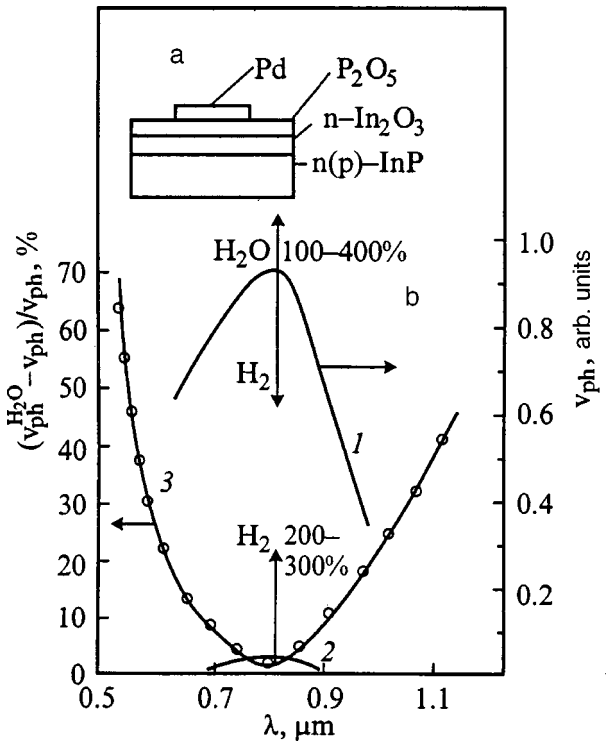


FIG. 1. a — Schematic of diode structure; b: *1* — spectral curve of photo-emf, *2* — spectral curve of $n$-InP–$n$-$In_2O_3$–$P_2O_5$–Pd structure after admitting 0.5 pm $H_2$; *3* — increase in photo-emf (%) under pulsed action of water vapor as a function of the wavelength of the exciting light, $p$-InP–$n$-$In_2O_3$–$P_2O_5$–Pd structure.

 © 1999 American Institute of Physics

and barely changes it at $\lambda_{max}$ (curve *3*, Fig. 1b).

We shall now discuss possible mechanisms for changes in the current transport which are responsible for this high sensitivity to moisture and hydrogen.

The photo-emf at low signal levels can be approximately given by

$$V_{ph} \approx I_{ph} R_0, \tag{1}$$

where $I_{ph}$ is the short-circuit current and $R_0$ is the zero-bias resistance. The change in the photo-emf must be a consequence of a change in one or other of these parameters or a preferential change in one of these parameters. We know that $P_2O_5$ is a strong absorber of water vapor and this should change the properties of the oxide and, which is very important, should change the characteristics of the *n*-$In_2O_3$–$P_2O_5$ and $P_2O_5$–Pd heterojunctions. Experience has shown that the forward and return currents change negligibly under the action of a water vapor ''pulse.'' We therefore assume that the increase in the photo-emf is mainly caused by an increase in $I_{ph}$, i.e., a change in the characteristics of the nonequilibrium minority carriers. Taking into account the intermediate $P_2O_5$ layer, the photocurrent may be expressed in the form

$$I_{ph} = \frac{I_{ph\,0}}{1 + D\sigma_{n,p} f_s \exp(b_{n,p}\chi^{1/2}\delta)}, \tag{2}$$

where $I_{ph\,0}$ is the photocurrent of a Schottky diode without an intermediate layer, $D$ is the density of bound states at the *n*-$In_2O_3$–$P_2O_5$ heterojunction, $\sigma_{n,p}$ are the cross sections for trapping of minority carriers, $b_{n,p}$ are the tunneling coefficients, $\chi_{n,p}$ is the semiconductor–insulator barrier height, and $\delta$ is the thickness of the $P_2O_5$ oxide. When water vapor is absorbed, it is unlikely that the transmission coefficient $b_{n,p}\chi_{n,p}^{1/2}\delta$ of the oxide $P_2O_5$ will change appreciably. However, a radical change is predicted for the pre-exponential factor $D\sigma_{n,p}f_s$ which reflects the recombination characteristics of the minority carriers. We can postulate that in the absence of a water vapor pulse, the recombination flux of minority carriers to bound states of density $D$, located at the *n*-$In_2O_3$–$P_2O_5$ heterojunction will be high. In expression (2) we then have $D\sigma_{n,p}f_s \exp(b_{n,p}\chi_{n,p}^{1/2}\delta) > 1$. Under the action of a vapor pulse $D$ decreases substantially, which increases the lifetime of the minority carriers $\tau_{n,p}$. A possible mechanism for this change is determined by the interaction of $H_2O$ molecules with bound heterojunction states. According to some data,[8] no dissociation of $H_2O$ molecules is observed when $H_2O$ is adsorbed on an InP surface, although some partial dissociation cannot be eliminated. We know that the absorption of water causes some deterioration in the characteristics of $P_2O_5$ as an insulator, in particular, increasing the conductivity. Bearing in mind these factors, we can postulate that the molecular absorption of $H_2O$ leads to loosening of the oxide lattice and the formation of new ''defect'' states at the heterojunction and in the $P_2O_5$ bulk. These new states suppress the influence of the initial states, lowering their concentration $D$. Since we can assume that in this process $D \sim (1/N_0)$, where $N_0$ is the concentration of absorbed molecules at the heterojunction, then

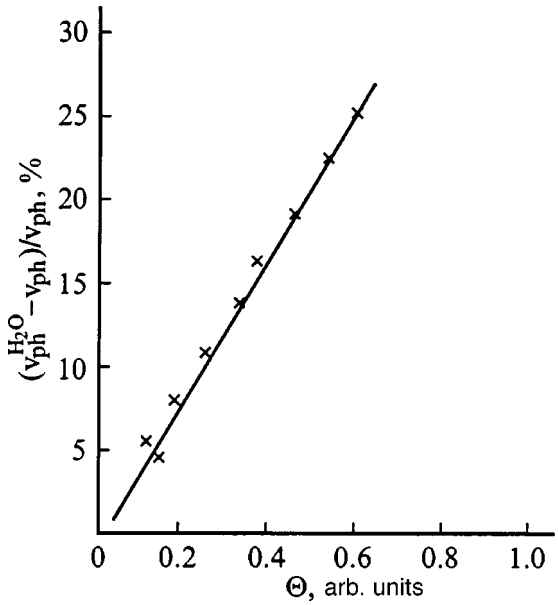


FIG. 2. Change in photo-emf (%) as a function of the water vapor concentration, for *p*-InP–*n*-$In_2O_3$–$P_2O_5$–Pd structure.

$$I_{ph} \sim \frac{I_{ph\,0} N_0}{\sigma_{n,p} f_s \exp(b_{n,p}\chi_{n,p}^{1/2}\delta)}, \tag{3}$$

i.e., the photo-emf should be proportional to the water vapor concentration. Figure 2 shows the corresponding linear characteristic.

It can be seen from Fig. 3 that the relaxation times of the photo-emf pulse which records the water vapor pulse for *p*-InP-based structures are approximately the same for the ascending and descending branches at 1–2 s. For the *n*-InP structures the descending branch may have an elongated relaxation tail of 60 s. Structures of this type probably have additional deep trapping centers.

The change in the photo-emf under the pulsed action of $H_2$, i.e., an increase for *p*-InP structures and a decrease for *n*-InP structures, is similar to the behavior of the photo-emf

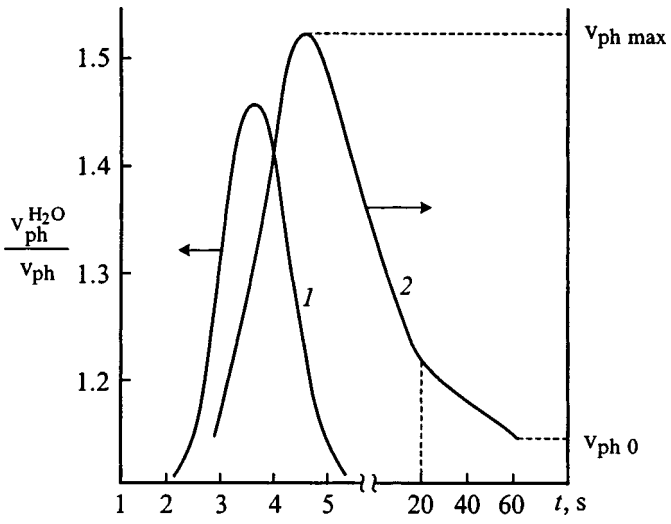


FIG. 3. Photo-emf pulses recording water vapor ''pulses'': *1* — *p*-InP structure, *2* — *n*-InP structure.

in $n(p)$-Si structures[9] and is determined by the change in the height of the Schottky barrier. Experiments to measure the relaxation times of the return current and the photo-emf after an $H_2$ pulse in $p$-InP structure showed an opposite symmetrical change in these characteristics. The dependence of the photo-emf on the electrical characteristics is given by

$$V_{\mathrm{ph}} \sim \frac{kT}{q} \ln\left[\frac{I_{\mathrm{ph}}}{I_{p0}\exp(-bp\chi_p^{1/2}\delta)} + 1\right]. \quad (4)$$

From this it follows directly that a decrease in the dark return current defined by $I_{p0}\exp(-bp\chi_p^{1/2}\delta)$ leads to an increase in the photo-emf and conversely.

These results show that it is possible to use an $n(p)$-InP–$n$-$In_2O_3$–$P_2O_5$–Pd structure to fabricate a triple-purpose detector, for near-infrared radiation, moisture, and hydrogen. However, it is quite clear that in order to improve the efficiency of these multipurpose detectors, both the technological characteristics of the structure and the electrical characteristics of its constituent elements must be optimized.

The authors are deeply grateful to A. M. Marinova for assistance with the fabrication technology for the structures.

[1] G. G. Kovalevskaya, L. Kratena, M. M. Meredov, A. M. Marinova, and S. V. Slobodchikov, Pis'ma Zh. Tekh. Fiz. **15**(12), 55 (1989) [Sov. Tech. Phys. Lett. **15**, 478 (1989)].
[2] G. G. Kovalevskaya, A. M. Marinova, and S. V. Slobodchikov, Zh. Tekh. Fiz. **59**(11), 155 (1989) [Sov. Phys. Tech. Phys. **34**, 1327 (1989)].
[3] S. V. Slobodchikov, G. G. Kovalevskaya, M. M. Meredov, A. V. Pentsov, E. V. Russu, and Kh. M. Salikhov, Pis'ma Zh. Tekh. Fiz. **17**(15), 1 (1991) [Sov. Tech. Phys. Lett. **17**, 535 (1991)].
[4] K. M. Geib and C. M. Wilmsen, J. Vac. Sci. Technol. **17**, 952 (1980).
[5] J. F. Wager, D. L. Ellsworth, S. M. Goodnick, and C. M. Wilmsen, J. Vac. Sci. Technol. **19**, 513 (1981).
[6] D. H. Lauglin and C. M. Wilmsen, Appl. Phys. Lett. **37**, 915 (1980).
[7] M. M. Meredov, G. G. Kovalevskaya, E. V. Russu, and S. V. Slobodchikov, Fiz. Tekh. Poluprovodn. **26**, 1590 (1992) [Sov. Phys. Semicond. **26**, 893 (1992)].
[8] G. J. Hughes, T. P. Humphreys, V. Montgomery, and R. N. Williams, Vacuum **31**, 539 (1981).
[9] G. G. Kovalevskaya, M. M. Meredov, E. V. Russu, Kh. M. Salikhov, and S. V. Slobodchikov, Zh. Tekh. Fiz. **63**(2), 185 (1993) [Tech. Phys. **38**, 149 (1993)].

Translated by R. M. Durham

# Angular dependence of the signal in nonlinear polarization spectroscopy under conditions of noncollinear excitation by partially polarized radiation

A. V. Gavrilenko and I. I. Gancherenok

*Belarus State University, Minsk*
(Submitted June 16, 1999)
Pis'ma Zh. Tekh. Fiz. **25**, 79–82 (December 26, 1999)

The light-induced anisotropy tensor of initially isotropic media is calculated for the case of partially nominally polarized radiation. An analytic expression is obtained for the first time for the signal in a noncollinear nonlinear polarization spectroscopy system with a polarization-incoherent pump wave. © *1999 American Institute of Physics.* [S1063-7850(99)02912-2]

In Ref. 1 we showed that the dependence of the signal on the angle of convergence $\theta$ of the probe and pump waves can be studied theoretically in a noncollinear nonlinear polarization spectroscopy (NPS) system. Although the analytic dependence of the signal intensity on the angle $\theta$ derived in this study was obtained under various assumptions, it provided a quantitative interpretation of the experimental data from Refs. 2 and 3. Moreover, the nonmonotonicity of the function $I(\theta)$ suggests that in addition to diagnostic applications, a noncollinear NPS system may also be used for effective spectroscopic investigations.[1,4]

This angular dependence was derived in Ref. 1 for completely polarized pump and probe radiation, however, this approximation does not ideally satisfy all the experimental conditions. Moreover, when studying weak effects, the difference between the degree of polarization of the radiation and its limiting value may be of the same order of smallness as the effects being studied. At the same time, the degree of polarization may serve as an additional experimental parameter (for example, for control measurements).

The aim of the present study is to obtain an analytic expression for the NPS signal in the general case of an arbitrary degree of polarization of the pump wave and an arbitrary angle of convergence of the interacting waves.

We shall follow a conventional scheme for our investigations: the light-induced anisotropy tensor $\hat{\kappa}$ is a contraction of the light-induced anisotropy tensors with the unit vectors $\mathbf{u}_P$ and $\mathbf{u}_A$, characterizing the action of the polarizer and the analyzer in the NPS system, and $\mathbf{u}_A^* \hat{\kappa} \mathbf{u}_P$ is the intensity of the transmitted signal $I = Kz^2 |\mathbf{u}_A^* \hat{\kappa} \mathbf{u}_P|^2$. Here we have $K = \frac{9}{16}(\omega_1^2/c^2 n_1^2) |\chi_{1221}|^2 |E_{10}|^2 |E_0|^4$, $\omega_1$ is the frequency of the probe wave, $\chi_{1221}$ is the component of the third-order nonlinear optical susceptibility tensor, $E_{10}$ and $E_0$ are the amplitudes of the probe wave (initial value) and the pump wave, $n_1$ and $c$ are the refractive index at frequency $\omega_1$ and the velocity of light in vacuum, $z$ is the distance covered by the probe wave in a medium with light-induced anisotropy, and an asterisk denotes complex conjugation. A more detailed description of this procedure can be found in Refs. 5–7.

The tensor $\hat{\kappa}$ is defined in terms of the beam tensor $\hat{\Phi}$, introduced by Fedorov[8] as follows:[9]

$$\hat{\kappa} = \hat{I} + C_1 \hat{\Phi} + C_2 \hat{\Phi}^*, \tag{1}$$

where $\hat{I}$ is the unit tensor, and $C_1$ and $C_2$ are expressed in terms of the components of the nonlinear susceptibility tensor.[8] Using the expression for the beam tensor in the general case of partially polarized radiation,[7] we obtain the light-induced anisotropy tensor as follows:

$$\hat{\kappa} = \hat{I} + I_0 \left[ \left( \frac{1-p}{2} \right) C\hat{I} + p(C_1 \mathbf{e}_0 \otimes \mathbf{e}_0^* + C_2 \mathbf{e}_0^* \otimes \mathbf{e}_0) - \frac{1-p}{2} C \hat{\tau}_n \right], \tag{2}$$

where $I_0 = |E_0|^2$, $C = C_1 + C_2$, $p$ is the degree of polarization, $\mathbf{e}_0$ is the normalized electric field strength vector of the pump wave, $\hat{\tau}_n = \mathbf{n}_0 \otimes \mathbf{n}_0$, $\mathbf{n}_0$ is the unit vector of the normal of the pump wave, and the symbol $\otimes$ denotes the Kronecker (dyadic) product of the vectors.

In accordance with the classification of media presented in Ref. 8, the tensor (2) corresponds to an absorbing anisotropic medium possessing intrinsic gyrotropy.

We shall subsequently assume that the polarizer and analyzer are characterized by the real unit vectors $\mathbf{u}_P$ and $\mathbf{u}_A$. We shall assume that within the cell dimensions the distance $z$ is related to the pump beam width parameter $l$ by $z = l/\sin\theta$. The final formula for the intensity of the NPS signal then has the form:

$$I = \frac{Kl^2}{4 \sin^2 \theta} \left[ \left( -\frac{C}{2} \sin 2\alpha \sin^2 \theta + pC \cos 2\eta \left( \cos\theta \sin 2\varphi \cos 2\alpha - \frac{\sin 2\alpha \cos 2\varphi}{2} \times (1 + \cos^2 \theta) \right) \right)^2 + p^2 S^2 \sin^2 2\eta \cos^2 \theta \right], \tag{3}$$

where the angular parameter $\alpha$ determines the orientation of the polarizer axis relative to the vector $\mathbf{a}_0$ of the orthonormalized basis $\mathbf{a}_0$, $\mathbf{b}_0$, $\mathbf{n}_0$, related to the normal $\mathbf{n}_0$ and the phase plane of the pump wave, and the angles $\eta$ and $\varphi$ define the ellipticity and the polarization azimuth of the

 © 1999 American Institute of Physics

strong wave in this basis, respectively, $S=C_1-C_2$, and we assume that the parameters $C_1$ and $C_2$ are real.[4]

For completely unpolarized pump radiation ($p=0$) the intensity of the NPS signal is

$$I \propto \sin^2 \theta \sin^2 2\alpha. \quad (4)$$

In the particular cases of a completely polarized strong wave with linear or circular polarization, expression (3) yields the corresponding expressions from Ref. 1 which explain the experimentally observed dependence $\cot^2\theta$. We merely note that in expression (11) from Ref. 1, the first term in large brackets should have the factor 1/4 and the corresponding changes should be introduced into formula (12).

An analysis of expression (3) suggests an experimental geometry which can simplify the interpretation of the experimental data under conditions of appreciable depolarization. A convenient geometry has the polarizer axis positioned in the direction of the vector $\mathbf{a}_0$ (the angle $\alpha$ is 0), or orthogonal to this direction (the angle $\alpha$ is $\pi/2$). The recording device then records the signal:

$$I \propto [C^2 \cos^2 2\eta \sin^2 2\varphi + S^2 \sin^2 2\eta] \cot^2 \theta, \quad (5)$$

which is determined by the polarization state of the high-power wave and the angle of convergence of the probe and pump waves. In this case, the degree of polarization is merely a calibration parameter.

To sum up, we have derived for the first time an analytic expression for the NPS signal in a noncollinear geometry. Explicit dependences of the intensity on the angle of convergence of the interacting waves, the position of the polarizer and the analyzer relative to the direction of excitation, and the state and degree of polarization of the pump wave have been obtained.

This work was partially supported under the project INTAS-Belarus 97-0207.

[1] A. V. Lavrinenko and I. I. Gancherenok, Opt. Spektrosk. in press (1999).
[2] G. Zizak, J. Lanauze, and J. D. Winefordner, Appl. Opt. **25**, 3242 (1986).
[3] K. Nyholm, R. Fritzon, and M. Alden, Opt. Lett. **18**, 1672 (1993).
[4] I. I. Gancherenok, *Nonlinear Photoanisotropy of Isotropic Resonant Media and its Spectroscopic Applications*, Dissertation for Doctorate of Physical-Mathematical Sciences [in Russian], Minsk, (1997), 273 pp.
[5] I. I. Gancheryonok, Jpn. J. Appl. Phys., Part 1 **231**, 3862 (1992).
[6] I. I. Gancheryonok, Rev. Laser Eng. **20**, 813 (1992).
[7] I. I. Gancheryonok and A. V. Lavrinenko, Opt. Applic. **25**(2), 93 (1995).
[8] F. I. Fedorov, *Theory of Gyrotropy* [in Russian], Nauka i Tekhnika, Minsk (1976), 456 pp.
[9] I. I. Gancheryonok, Jpn. J. Appl. Phys., Part 1 **31**, 3564 (1992).

Translated by R. M. Durham

# Analysis of the fundamental absorption edge in amorphous hydrogenated carbon films

A. V. Vasin, L. A. Matveeva, and A. M. Kutsaĭ

*Institute of Semiconductor Physics, National Academy of Sciences of Ukraine, Kiev*
*Institute of Supraresistant Materials, National Academy of Sciences of Ukraine, Kiev*
(Submitted June 16, 1999)
Pis'ma Zh. Tekh. Fiz. **25**, 83–87 (December 26, 1999)

Optical spectroscopy was used to study the high-energy region of the fundamental absorption edge in films of amorphous hydrogenated carbon obtained for various deposition parameters. The slope of the absorption edge was analyzed using the slope of the linear Tauc dependence. The results of the optical spectroscopy were compared with the Raman light scattering data and the content of bound hydrogen in the films. A correlation is established between the slope of the absorption edge, the deposition parameters, and the structure of the films. © *1999 American Institute of Physics.* [S1063-7850(99)03012-8]

Films of amorphous hydrogenated carbon are of considerable practical interest because of their broad spectrum of mechanical, electrical, and optical properties, which depend on the deposition conditions. For instance, it has been shown[1–3] that because of their transparency in the near infrared, high mechanical strength, and chemical inertness, hydrogenated carbon films can be used as protective antireflection coatings for infrared radiation detectors and solar cells.

Films of amorphous hydrogenated carbon were deposited on glass and silicon substrates from a mixture of methane and hydrogen gas activated with an rf (13.5 MHz) discharge in a planar reactor. The variable deposition parameters were the gas mixture composition and the self-bias potential $V_{sb}$ of the electrode-susceptor at a constant working pressure of 0.8 Torr.

The spectral dependence $\alpha(h\nu)$ was investigated in the energy range 1.4–4.5 eV using a SPECORD M 400 spectrophotometer. Raman scattering spectra of the carbon films were excited using the 514 nm argon laser line and were analyzed from the point of view of the intensity ratio of the *D* and *G* bands.[4–6] The content of bound hydrogen was estimated by analyzing the intensities of the hydrocarbon stretching vibration bands in the range 2700–3200 $cm^{-1}$ (Ref. 7). The infrared spectra were recorded using a SPECORD M80 spectrophotometer.

Unlike ordered solid graphite, films of amorphous hydrogenated carbon have semiconducting properties which are found in the presence of a band gap. The band gap is usually determined by a linear extrapolation of the Tauc dependence[8]

$$\alpha \cdot h\nu = B \cdot t(h\nu - E_g)^2,$$

where $\alpha$ is the absorption coefficient, $h\nu$ is the photon energy, $E_g$ is the optical band gap, and *B* is the slope of the absorption edge.

The inset to Fig. 1 shows the Tauc dependence for a film obtained for the self-bias $U_{sb} = -300$ V and the gas mixture composition $CH_4$30% + $H_2$70%. Also plotted is the dependence of the coefficient *B* on the deposition parameters. The dependence of *B* on the self-bias potential generally shows the same trend for different gas mixture compositions. For values of $U_{sb}$ greater than $-100$ V, the slope of the absorption edge increases steeply. A further increase in the self-bias weakly influences *B*. The fact that the dependences of *B* on $U_{sb}$ show the same general behavior for various gas mixture compositions suggests that the self-bias potential principally determines the slope of the absorption edge.

The Raman scattering spectra of the films comprised a broad axisymmetric band near 100–1700 $cm^{-1}$ typical of amorphous carbon films.[4,5] The results of a computer analysis of the spectra were used to estimate the intensity ratio of the *D* and *G* bands $I_D/I_G$. Figure 2 gives the ratios $I_D/I_G$ (curve *1*, left-hand scale) and also the content of bound hydrogen in films (Fig. 2, right-hand scale) prepared using various self-biases and a constant concentration of gas mixture $CH_4$30% + $H_2$70%.

From an analysis of these results we can isolate the following main correlations: the tendency of the slope *B* of the fundamental absorption edge to increase with increasing $U_{sb}$ is accompanied by an increase in the relative intensity of the *D*-band and a reduction in the bound hydrogen content in the film.

As has already been established,[5,6] the optical properties of hydrogenated carbon films near the fundamental absorption edge are determined by the graphite-like fraction. From this viewpoint we can postulate that the slope of the absorption edge is determined by the density of $\pi$-electron states participating in the optical absorption in this energy range. These experimental results can be explained in terms of the following concepts. At low discharge powers ($U_{sb} \leqslant -100$ V), because of the low degree of dissociation of the methane molecules, a large quantity of bound hydrogen is incorporated into the film. This bound hydrogen impedes the growth of graphite-like nanocrystallites so that the size of the ordered regions remains small[5] ($\leqslant 1$ nm). The small number of atoms in the ordered system is responsible for the low density of electron states and thus the broadened absorption edge. At high discharge powers the degree of dissociation of the methane molecules increases which helps to en-

 © 1999 American Institute of Physics

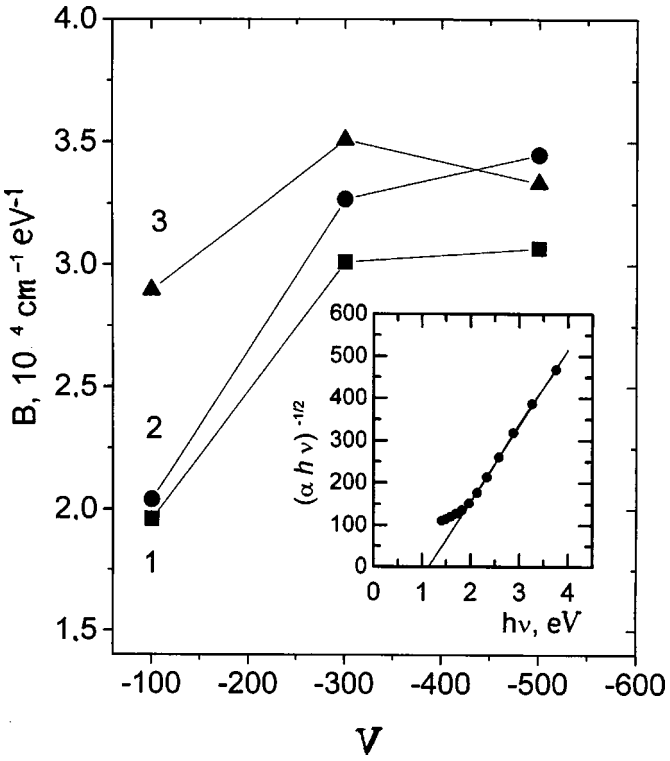


FIG. 1. Slope $B$ of the absorption edge as a function of the self-bias potential for films deposited using various gas mixture compositions: *1* — $CH_4$30% + $H_2$70%; *2* — $CH_4$50% + $H_2$50%; *3* — $CH_4$70% + $H_2$30%; the inset shows a typical Tauc dependence for *a*-C:H films.

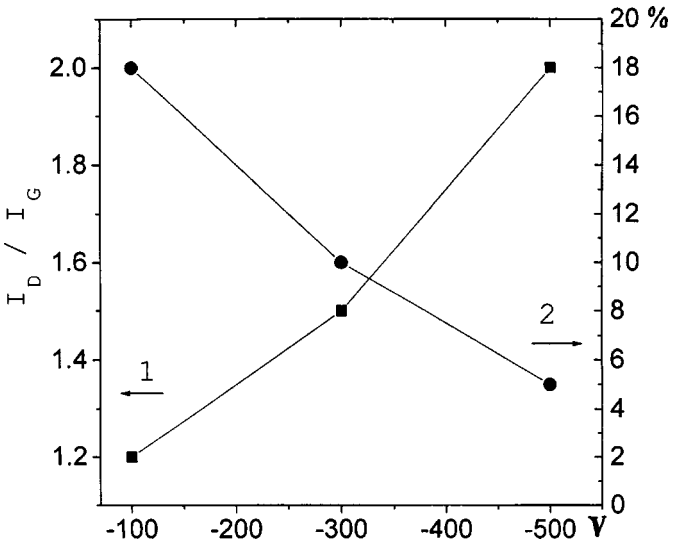


FIG. 2. Dependence of the intensity ratio of the $D$ and $G$ bands on the self-bias potential (left-hand scale) — *1*; content of bound hydrogen as a function of self-bias potential (right-hand scale) — *2*.

large the graphite-like nanocrystallites. The associated increase in the density of electron states accounts for the steeper absorption edge.

To sum up, we have established that when amorphous hydrogenated carbon films are obtained by plasma-chemical deposition, the main process parameter determining the degree of broadening of the absorption edge is the discharge power which determines the quantity of bound hydrogen and the size of the graphite-like nanocrystallites. In this case, the slope of the absorption edge is determined by the density of $\pi$-electron states.

[1] A. H. Lettington, Philos. Trans. R. Soc. London A **342**, 193 (1993).
[2] J. Robertson, Philos. Trans. R. Soc. London A **342**, 277 (1993).
[3] L. S. Aivazova, N. V. Novicov, S. I. Khandozhko *et al.*, J. Chem. Vapor Dep. **6**(1), 52 (1997).
[4] R. O. Dillon, J. A. Woollam, and V. Karkanant, Phys. Rev. B **29**, 3482 (1984).
[5] Hisao-chu Tsai and D. B. Bogy, J. Vac. Sci. Technol. A **5**, 3287 (1987).
[6] M. A. Tamor, J. A. Haire, C. H. Wu *et al.*, Appl. Phys. Lett. **54**, 123 (1989).
[7] B. Dischler, A. Bubenzer, and P. Koidi, Solid State Commun. **48**(2), 105 (1983).
[8] J. Tauc, R. Grigorovici, and A. Vancu, Phys. Status Solidi **15**, 627 (1966).

Translated by R. M. Durham

# Optical method of determining the components of the relative displacement vector

A. P. Vladimirov, V. I. Mikushin, and A. L. Lisin

*Institute of Machine Sciences, Urals Branch of the Russian Academy of Sciences, Ekaterinburg*
(Submitted October 19, 1998; resubmitted June 30, 1999)
Pis'ma Zh. Tekh. Fiz. **25**, 88–94 (December 26, 1999)

The theory of a laser interference method of determining in real time the relative displacement of two scattering objects in space is put forward and an experimental verification is described.
© *1999 American Institute of Physics.* [S1063-7850(99)03112-2]

## 1. INTRODUCTION

We are familiar with the method of determining the absolute displacements of a surface based on a real-time analysis of the interference pattern obtained by superposing a speckle field and a reference field[1] and also with the method of determining the relative displacements along the normal to the surface based on an interference comparison of two identical speckle fields.[2] In the present study, as a development of these methods[1,2] we describe the theory and an experimental verification of a method of determining the components of the relative displacement vector.

## 2. THEORY

Let us assume that a source of coherent radiation positioned at a point **s** (Fig. 1) illuminates two three-dimensional diffusers *1* and *2* comprising a set of point scatterers distributed randomly in regions $V_1$ and $V_2$ near points $\mathbf{R}_{01}$ and $\mathbf{R}_{02}$. We then assume that waves having random amplitudes and phases arrive at point **q** in the free field from these point scatterers. We shall neglect multiple scattering of the waves and the difference in their polarizations. Assuming that $\mathbf{u}_1$ and $\mathbf{u}_2$ are the displacement vectors of diffusers *1* and *2*, we express the total complex amplitude of the scattered radiation at point **q** as follows:

$$\begin{aligned} A(\mathbf{q}) &= A_1(\mathbf{q}) + A_2(\mathbf{q}) \\ &= \sum_{i=1}^{N} |a_i| \exp\{i\varphi_i + ik[|\mathbf{L}_{s1}(\mathbf{R}_i+\mathbf{u}_1)| + |\mathbf{L}_{q1}(\mathbf{R}_i+\mathbf{u}_1)|]\} \\ &\quad + \sum_{j=1}^{M} |a_j| \exp\{i\varphi_j + ik[|\mathbf{L}_{s2}(\mathbf{R}_j+\mathbf{u}_2)| + |\mathbf{L}_{q2}(\mathbf{R}_j+\mathbf{u}_2)|]\}, \end{aligned} \tag{1}$$

where $A_1(\mathbf{q})$ and $A_2(\mathbf{q})$ are the total complex amplitudes of the waves scattered from regions $V_1$ and $V_2$, respectively, $|a_i|$ and $\varphi_i$ are the modulus and random phase of the complex amplitude of the wave arriving at point **q** from the $i$th scatterer, $M$ and $N$ are the number of scatterers in regions $V_1$ and $V_2$, respectively, $k$ is the wave number, $|\mathbf{L}_{s1}(\mathbf{R}_i+\mathbf{u}_1)|$ is the distance between the radiation source and the point scatterer having the coordinate $\mathbf{R}_i+\mathbf{u}_1$ for the first diffuser, $|\mathbf{L}_{q1}(\mathbf{R}_i+\mathbf{u}_1)|$ is the distance between the point $\mathbf{R}_i+\mathbf{u}_1$ and the observer, and $|\mathbf{L}_{s2}(\mathbf{R}_j+\mathbf{u}_2)|$ and $|\mathbf{L}_{q2}(\mathbf{R}_j+\mathbf{u}_2)|$ are similar distances for the second diffuser.

Assuming that the sizes of the regions $V_1$ and $V_2$ and also the displacements of the diffusers are small compared with the distances between the point scatterers and the points **s** and **q**, we expand $|\mathbf{L}_{s1}(\mathbf{R}_i+\mathbf{u}_1)|$ and $|\mathbf{L}_{s2}(\mathbf{R}_j+\mathbf{u}_2)|$ near the points $\mathbf{s}, \mathbf{R}_{01}$ and $\mathbf{s}, \mathbf{R}_{02}$, respectively, and $|\mathbf{L}_{q1}(\mathbf{R}_i+\mathbf{u}_1)|$ and $|\mathbf{L}_{q2}(\mathbf{R}_j+\mathbf{u}_2)|$ near the points $\mathbf{q}, \mathbf{R}_{01}$ and $\mathbf{q}, \mathbf{R}_{02}$, respectively, allowing only for the first-order derivatives. We have:

$$\begin{aligned} |\mathbf{L}_{s1}(\mathbf{R}_i+\mathbf{u}_1)| &= \rho_{s1} + \mathbf{l}_{s1}(\mathbf{r}_i+\mathbf{u}_1), \\ |\mathbf{L}_{q1}(\mathbf{R}_i+\mathbf{u}_1)| &= \rho_{q1} + \mathbf{l}_{q1}(\mathbf{r}_i+\mathbf{u}_1), \\ |\mathbf{L}_{s2}(\mathbf{R}_j+\mathbf{u}_2)| &= \rho_{s2} + \mathbf{l}_{s2}(\mathbf{r}_j+\mathbf{u}_2), \\ |\mathbf{L}_{q2}(\mathbf{R}_j+\mathbf{u}_2)| &= \rho_{q2} + \mathbf{l}_{q2}(\mathbf{r}_j+\mathbf{u}_2), \end{aligned} \tag{2}$$

where $\rho_{s1}$ and $\rho_{s2}$ are the distances from the point **s** to points $\mathbf{R}_{01}$ and $\mathbf{R}_{02}$, respectively, $\rho_{q1}$ and $\rho_{q2}$ are the distances from points $\mathbf{R}_{01}$ and $\mathbf{R}_{02}$ to the point **q**, respectively, $\mathbf{l}_{s1}$ and $\mathbf{l}_{s2}$ are unit vectors directed from the points $\mathbf{R}_{01}$ and $\mathbf{R}_{02}$ to the radiation source, respectively, $\mathbf{l}_{q1}$ and $\mathbf{l}_{q2}$ are unit vectors directed from the points $\mathbf{R}_{01}$ and $\mathbf{R}_{02}$, respectively, to the point **q**, and $\mathbf{r}_i$ and $\mathbf{r}_j$ are the coordinates of the point scatterers relative to the points $\mathbf{R}_{01}$ and $\mathbf{R}_{02}$, respectively.

We then find the intensity of the scattered radiation $I$ at point **q**. Subsequently omitting the coordinate **q**, we then have:

$$I = |A|^2 = I_1 + I_2 + A_1A_2^* + A_1^*A_2, \tag{3}$$

where $I_1$ and $I_2$ are the radiation intensities at point **q** in the absence alternately of diffusers *2* and *1*, respectively.

We transform the expression $A_1A_2^*$ using expressions (1) and (2) which gives:

$$\begin{aligned} A_1A_2^* = \exp\{ik[&\rho_{s1} + \rho_{q1} + \mathbf{u}_1(\mathbf{l}_{s1}+\mathbf{l}_{q1}) - \rho_{s2} - \rho_{q2} \\ &- \mathbf{u}_2(\mathbf{l}_{s2}+\mathbf{l}_{q2})]\} \cdot N \cdot M \cdot \tilde{A}_n \cdot \tilde{A}_m^*, \end{aligned} \tag{4}$$

where $\tilde{A}_n$ and $\tilde{A}_m^*$ are the arithmetical means of $|a_n|\exp\{i[\varphi_n + k\mathbf{r}_n(\mathbf{l}_{s1}+\mathbf{l}_{q1})]\}$ and $|a_m|\exp\{-i[\varphi_m - k\mathbf{r}_m \times (\mathbf{l}_{s2}-\mathbf{l}_{q2})]\}$, respectively, $n=1,\ldots,N$, $m=1,\ldots,M$. Similarly for $A_1^*A_2$ we have:

 © 1999 American Institute of Physics

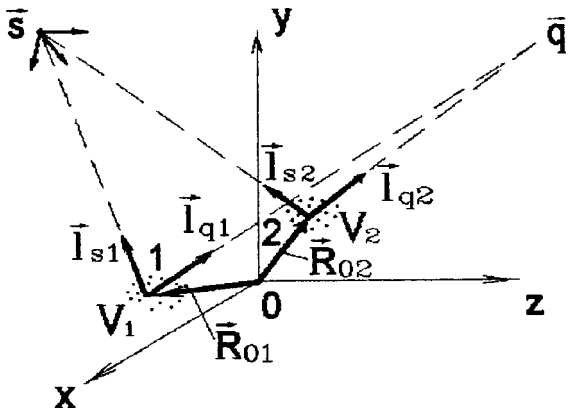


FIG. 1. System of coordinates and notation.

$$A_1^* A_2 = \exp\{-ik[\rho_{s1}+\rho_{q1}+\mathbf{u}_1(\mathbf{l}_{s1}+\mathbf{l}_{q1})-\rho_{s2}-\rho_{q2} - \mathbf{u}_2(\mathbf{l}_{s2}+\mathbf{l}_{q2})]\}\cdot N\cdot M\cdot \tilde{A}_n^*\cdot \tilde{A}_m. \quad (5)$$

Assuming that for fairly large $M$ and $N$: $\tilde{A}_n\tilde{A}_m^* = \tilde{A}_n^*\tilde{A}_m = \tilde{I}_{12}$ and $\mathbf{l}_{s1}=\mathbf{l}_{s2}=\mathbf{l}_s$, $\mathbf{l}_{q1}=\mathbf{l}_{q2}=\mathbf{l}_1$, which can be achieved in practice using systems of mirrors, we have instead of Eq. (3):

$$I = I_1 + I_2 + 2\cdot I_{1,2}\cdot\cos\{k[\Delta\rho+\Delta\mathbf{u}(\mathbf{l}_s+\mathbf{l}_q)]\}, \quad (6)$$

where $I_{1,2}=N\cdot M\cdot\tilde{I}_{12}$, $\Delta\rho=\rho_{s1}+\rho_{q1}-\rho_{s2}-\rho_{q2}$, and $\Delta\mathbf{u}=\mathbf{u}_1-\mathbf{u}_2$ is the vector of the relative displacements of the diffusers. For $\Delta\rho=$ const and $\Delta\mathbf{u}\neq 0$, formula (6) describes a periodic change in intensity as a result of the displacements of the diffusers. It follows from formula (6) that

$$(\mathbf{l}_s+\mathbf{l}_q)\Delta\mathbf{u}=\Delta N\cdot\lambda, \quad (7)$$

where $\Delta N = N - N_0$, $N_0$ and $N$ are the orders of the fringes at the observation point before and after the relative displacement of the diffusers by $\Delta\mathbf{u}$ and $\lambda$ is the wavelength.

### 3. EXPERIMENT

In order to check formula (7), we carried out an experiment in which the relative displacements of the diffusers were produced by periodic loading of a cylinder.

A hollow cylinder *1* (Fig. 2) made of D16 aluminum alloy, having inner and outer diameters of 21.7 and 24.8 mm, respectively and a length of 65 mm, was mounted coaxially together with a solid cylinder *3*, 77 mm long and 30 mm in diameter between rigid screw clamps *5*. Periodic loading was achieved by heating the solid cylinder *3* with an electric coil and then allowing it to cool naturally after the voltage had been switched off. A 20 mm thick ceramic plate was inserted between the cylinders for thermal insulation.

A laser beam *6* was split into two beams by a semitransmitting mirror *7* and a mirror *8* directed these beams onto the surface of the object, parallel to each other and along the normal to the surface (parallel to the *z* axis). The dimensions of the illuminated sections of the surface were of the order of 0.3 mm and the distance $l_0$ between these illuminated sections was 12.3 mm. A lens *9* of 61 mm focal length focused the beams onto the surface. Two matched pairs of scattered beams *10*, *11* and *12*, *13* reflected at angles $\beta_{x1}=138°$ and $\beta_{x1}=50°$ to the *x* axis and at an angle of 90° to the *y* axis, were produced by beams from the mirror *8* and the semitransmitting mirror *7*, and these were directed toward phototransistors *14*. The signals from the phototransistors were fed via an adapter *15* to an IBM PC/AT 16 computer for digital analysis. We used a $\lambda=0.6328\,\mu$m, 1.6 mW LGN207A helium–neon laser. The deformation of the cylinder was also monitored using a standard strain gauge *17* incorporated in an SIP-250 system. The distance $l_1$ between the strain gauge probes was 50 mm. The signals from the strain gauge were also fed into the computer.

Taking into account the angles of illumination and observation, from formula (7) we obtain relationships to determine the components of the relative displacement vector:

$$\Delta u_x = \lambda(0.698\Delta N_2 - 0.738\Delta N_1),$$

$$\Delta u_z = \lambda(0.271\Delta N_2 + 0.313\Delta N_1), \quad (8)$$

where $\Delta N_1$ and $\Delta N_2$ are the changes in the orders of the fringes corresponding to the angles of observation $\beta_{x1}$ and $\beta_{x2}$.

Figure 3 shows typical time-varying signals from the phototransistors and the strain gauge. The magnitudes of the signals are given in pixels of the computer monitor screen. A change in the strain gauge signal by 30 pixels corresponded to a relative displacement $\Delta l$ of the strain gauge probes by 3.5 $\mu$m.

Figure 4 gives the relative strains $\varepsilon_{xx}$, determined by the optical method using the formula $\varepsilon_{xxo}=\Delta u_x/l_0$ as a function

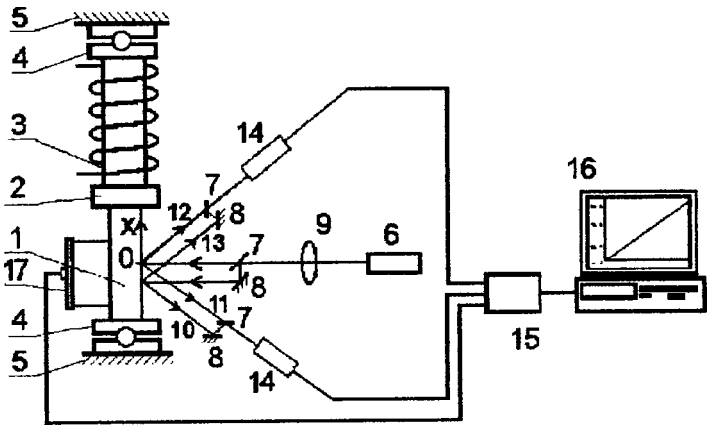


FIG. 2. Schematic showing loading of the object and optical system.

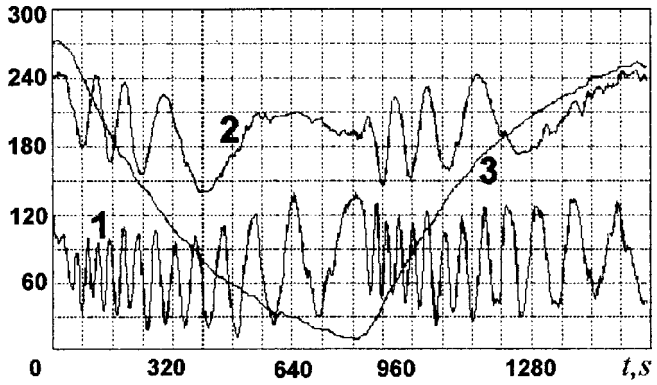


FIG. 3. Time dependences of the signals from the phototransistors (*1*, *2*) and the strain gauge (*3*).

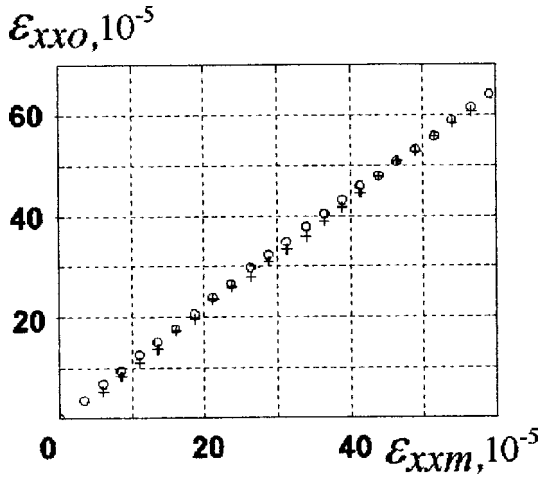


FIG. 4. Dependence of the strain $\varepsilon_{xx0}$ determined by the optical method on the strain $\varepsilon_{xxm}$ determined using the strain gauge: ○ — loading, + — unloading.

of the strains determined using the strain gauge readings from the formula $\varepsilon_{xxm}=\Delta l/l_1$. The values of $\Delta u_x$ were determined graphically by smoothing the experimental time dependence of the orders of the fringes $\Delta N_1$ and $\Delta N_2$ taking into account the signs of the fringe orders. The values of $\Delta N_1$ were assigned a minus sign and those of $\Delta N_2$ a plus sign from physical reasoning based on observations of the direction of displacement of the fringes during the experiment.

Note that the maximum relative displacement $\Delta u_z$ was 1.3 $\mu$m. The deviation of the experimental curve from unit slope in Fig. 4 was within 9%, and the difference in the readings of the optical detector for different parts of the surface was within 4%.

## CONCLUSIONS

The method of determining relative displacements considered in the present study has some similarities with holographic interferometry. If the directions of illumination of the scattering sections and the directions of observation of the scattered radiation are the same, the theoretical relationship between the displacement and the order of the fringes agrees with the same formula in holographic interferometry. The sensitivity of the methods is also the same. Since the change in the fringe pattern within the region of overlap of nonidentical speckles is analyzed in the proposed method, the limiting continuously measurable displacements depend on the relative displacement of the speckles and the decorrelation of the speckles caused by the displacement of the diffusers.

Good agreement was obtained between the relative displacements measured by the optical method and using a strain gauge. At present, the sensitivity of this optical method is inferior to that of the most sensitive strain gauges. However, the method is a noncontact one and can be used to determine all three component of the relative displacement vector.

[1] N. G. Vlasov, V. M. Ginzburg, and A. E. Shtan'ko, Author's Certificate No. 554467 [in Russian], Byull. Izobret. No. 14, (1977).
[2] B. B. Gorbatenko, I. S. Klimenko, V. P. Ryabukho, and L. A. Surmenko, Author's Certificate No. 1374042 [in Russian], Byull. Izobret. No. 6, (1988).

Translated by R. M. Durham

## ERRATA

# Erratum: Separation of germanium and silicon oxides by plasma-chemical deposition of germanosilicate glass in a moving plasma column [Tech. Phys. Lett. 25, 530–532 (1999)]

K. M. Golant and I. V. Nikitin

*Scientific Center of Fiber Optics, Institute of General Physics, Academy of Sciences, Moscow*

[S1063-7850(99)03212-7]

The correct author's name is **I. V. Nikolin**. We apologize for this error and are reprinting the article in its entirety.

# Separation of germanium and silicon oxides by plasma-chemical deposition of germanosilicate glass in a moving plasma column

K. M. Golant and I. V. Nikolin

*Scientific Center of Fiber Optics, Institute of General Physics, Russian Academy of Sciences, Moscow*
(Submitted April 5, 1999)
Pis'ma Zh. Tekh. Fiz. **25**, 55–61 (July 12, 1999)

The optical transmission spectrum of germanosilicate glass deposited by surface plasma chemical vapor deposition on the inner surface of a quartz tube revealed interference resonances typical of multilayer dielectric coatings with alternating refractive indices. It is shown that this effect can be attributed to the longitudinal inhomogeneity of the plasma composition and specifically to an axial shift of the concentration maxima of germanium and silicon oxide. As a plasma having a nonuniform composition moves along the tube, a layer of glass is formed with a strong transverse germanium concentration gradient. It is established that in surface plasma chemical vapor deposition the axial separation of the regions of deposition of the silicon and germanium oxides increases if the glass is synthesized under conditions of oxygen deficiency.
© *1999 American Institute of Physics.* [S1063-7850(99)01107-6]

Surface plasma chemical vapor deposition (SPCVD) is used to synthesize quartz-glass preforms for fiber-optical waveguides.[1] In this method, layers of pure and doped $SiO_2$ are deposited on the inner surface of a section of quartz glass tube whose volume is periodically filled with a chemically active plasma. This periodic filling is accomplished by varying the length of a steady-state plasma column which is created and sustained in the tube by microwave energy transported by surface plasma waves.[2] The length of the column (distance between the point of application of the microwave field and the point of plasma detachment) is regulated by varying the power supplied to the plasma.

In SPCVD, silicon dioxide is synthesized by passing silicon tetrachloride mixed with oxygen through a moving plasma column. When the reagents enter the discharge zone, gas-phase SiO molecules are formed as a result of the plasma-chemical interaction between $SiCl_4$ and oxygen molecules excited by electron impact. The process of glass formation on the walls of the tube terminates, where the SiO adsorbed from the gas phase is oxidized to give $SiO_2$ by heterogeneous addition of oxygen. The chlorine released as a result of the reactions and the excess oxygen are removed by the pumping system.

Here we report some characteristic features of the formation of germanosilicate glass by this method. In the experiments we synthesized and investigated glass coatings 200 $\mu$m thick deposited on the inner surface of a quartz tube having an outer diameter of 20 mm and a wall thickness of 2 mm. An $O_2+SiCl_4+GeCl_4$ mixture was passed into the tube at a total pressure of around 0.2 Torr. Each reagent was supplied via a separate RRG-9 gas flow rate regulator which measured each component of the gas mixture to within 1%. The coatings were deposited by periodically moving a plasma along a 25 cm long section of the tube. The velocity and amplitude of the displacement of the plasma column front was controlled using a feedback system which controls

 © 1999 American Institute of Physics

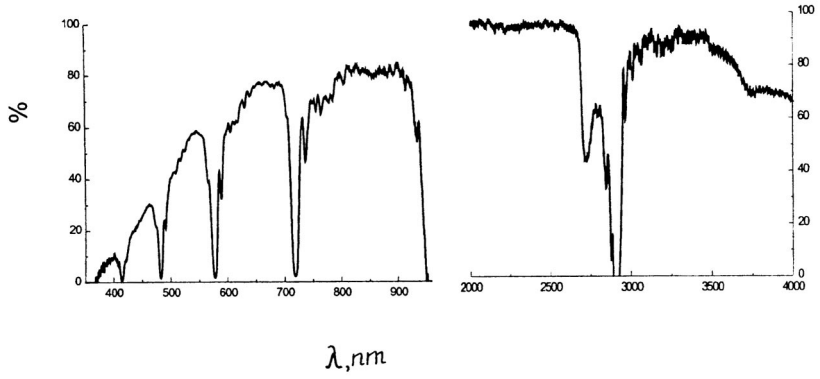


FIG. 1. Transmission spectrum of a germanosilicate glass coating 200 $\mu$m thick deposited on the inner surface of a quartz glass tube by SPCVD. The measurements were made using an S2000 Ocean Optics Inc. spectrometer at 350–940 nm and using a Perkin–Elmer Fourier spectrometer at 2000–4000 nm.

the microwave power supplied to the plasma. The chloride flow rate and the plasma displacement velocity were such that a 200 $\mu$m thick coating was obtained after 400 plasma passes. The temperature of the tube walls was stabilized at around 1200 °C by means of an electrical furnace and was monitored with an optical pyrometer. During the deposition process we observed temperature fluctuations in the range of $\pm 50$ °C about a given value, which were synchronous with the periodic motion of the plasma column and caused by the internal plasma heating of the tube. The deposition process was carried out with a flow rate ratio $SiCl_4/GeCl_4 = 10{:}1$, which corresponds to a $GeO_2$ content in the resultant glass of around 10 mol.% assuming 100% efficiency of implanting silicon and germanium atoms in the glass. After the end of the deposition process, the tube together with the layer of germanosilicate glass deposited on the inside was cut into transverse sections. These transverse sections were used as samples to obtain transmission spectra and were examined by electron microscopy.

A characteristic feature of the optical transmission spectrum of the deposited glass is its contrast interference structure (Fig. 1) which indicates that the refractive index distribution exhibits regular variations over the coating thickness. From the spectral position of the peaks we can readily establish that these correspond to different interference orders of the same periodic refractive-index structure with the fundamental interference order at the wavelength $\lambda_0 \approx 2.9$ $\mu$m.

Figure 2 shows a photograph of a transverse section of the deposited layer of germanosilicate glass obtained using a scanning electron microscope. The light bands correspond to sections of the glass having an increased germanium content. It can be seen that the periodic structure responsible for the observed transmission spectrum of the coating can be attributed to germanium concentration peaks repeated from one layer to another, which increase the refractive index of the glass. Note that, judging by Fig. 2, the thickness of the germanium-enriched layers is small and is at least an order of magnitude less than the period of the structure ($\approx 1$ $\mu$m for the deposition regime described above). We used the method of characteristic matrices[3] to model the transmission spectrum of a structure formed by ''thick'' dielectric layers of thickness $d$ separated by ''thin'' dielectric layers of high refractive index. The fundamental interference order for which the transmission coefficient of this structure has a minimum corresponds to the condition $d = \lambda_0/2n$ where $n$ is the refractive index of the glass in the thick layer. For $\lambda_0 \approx 2.9$ $\mu$m and $n \approx 1.45$ (undoped quartz glass) we obtain the estimate $d \approx 0.98$ $\mu$m which shows good agreement with the period of the layered structure shown in Fig. 2. If the total number of structure periods is 200 and the thickness of the thin germanium-enriched layers is of the order of 0.1 $\mu$m, the refractive index of the thin layers would have to be 1.55–1.6 to produce a contrast interference spectrum such as that shown in Fig. 1. Since the refractive index increment of quartz glass caused by introducing 10 mol.% $GeO_2$ does not exceed 0.014, it must be concluded that the $SiO_2$ and $GeO_2$ are substantially stratified at the glass formation stage in SPCVD. We note that the observed effect is too great to be a consequence of variations in the germanium content caused by the periodic temperature fluctuations of the tube walls noted above.

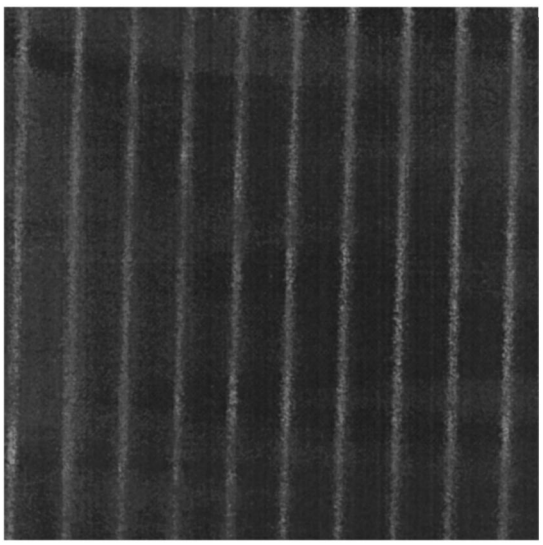

FIG. 2. Electron image of the transverse cross section of a deposited coating, which illustrates the periodic spatial variation of the germanium distribution. The period of the structure is 1 $\mu$m.

 © 1999 American Institute of Physics

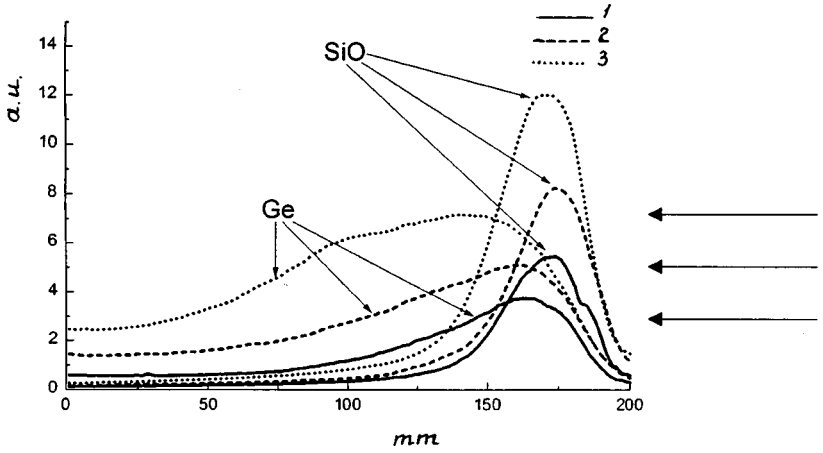


FIG. 3. Intensity distribution of the emission lines of SiO molecules and Ge atoms along a chemically active plasma at various oxygen partial pressures. The excess of oxygen in the gas mixture over that required by stoichiometry to oxidize all the silicon and germanium atoms is: *1* — a factor of 6.5; *2* — a factor of 4; and *3* — a factor of 2.6. The abscissa is directed from the exciter toward the point of plasma quenching.

Direct confirmation of a layering effect at the stage where the chlorides are converted to the gas phase is provided by the distribution curves of SiO molecules and Ge atoms in the plasma, obtained by local emission optical spectroscopy (Fig. 3). In the experiments we measured the intensity distributions of the 425 nm (SiO molecular band[4]) and the 327 nm spectral lines (Ge atomic line[5]) along the plasma column. Apart from variations in the parameters of the plasma electron component (density and temperature), the radiation intensities of the bands correspond to the concentrations of emitting particles. It can be seen from Fig. 3 that the maxima of the axial distributions of SiO and Ge are shifted relative to each other and the shift increases as the oxygen partial pressure decreases. As a result of this shift, the gaseous medium above the deposition zone is a section of plasma having a highly nonuniform composition. On its right-hand side some distance from the microwave exciter, predominantly $SiO_2$ is deposited whereas on the left-hand side it is predominantly $GeO_2$ (Fig. 2). The periodic motion of this inhomogeneous deposition zone relative to the tube results in the formation of a layered structure in the deposited layer.

Note that the thermodynamic characteristics of SiO and GeO differ substantially. For instance, the sublimation temperature of GeO at normal pressure is only 710 °C (Ref. 6), i.e., even at high pressure it is far below the characteristic temperature maintained during the deposition of quartz glass in the SPCVD process (1000–1200 °C). This can explain the ''pulling'' of Ge from the deposition zone into the depth of the plasma column. Quite clearly, this effect is intensified when there is an oxygen deficiency because the rate of heterogeneous oxidation of GeO to form $GeO_2$ is reduced.

To conclude we note that this layering effect in SPCVD is evidently typical not only of germanosilicate glass but also of other $SiO_2$-based systems in which the active radicals forming the glass are produced in different parts of the deposition zone. By varying the ratio of the reagent flow rates, we can control the parameters of these layered structures so that this effect can be used to produce quartz-glass optical interference filters.

For the optical measurements we used apparatus from the central pool of spectroscopic equipment of the Russian Academy of Sciences and we should like to thank the director, V. G. Plotnichenko, for making this possible. The authors would also like to thank S. V. Lavrishchev for the electron microscopic analyses of the samples and Prof. A. S. Biryukov for valuable comments.

This work was partially supported by the Russian Fund for Fundamental Research (Project No. 98-02-16361).

[1] D. Pavy, M. Moisan, S. Saada, P. Chollet, P. Leprince, and J. Marrec, in *Proceedings of the 12th European Conference on Optical Communication*, Barcelona, 1986, pp. 19–22.
[2] M. Moisan, C. Beaudry, and P. Leprince, IEEE Trans. Plasma Sci. **PS-3**(2), 55 (1975).
[3] M. Born and E. Wolf, *Principles of Optics*, 4th ed. (Pergamon Press, Oxford, 1969; Nauka, Moscow, 1970, 885 pp.).
[4] K. P. Huber and G. Herzberg, *Molecular Spectra and Molecular Structure*, Vol. 4 *Constants of Diatomic Molecules* [Russ. transl., Nauka, Moscow, 1984, 365 pp.].
[5] C. H. Corliss and W. R. Bozeman, *Experimental Transition Probabilities for Spectral Lines of Seventy Elements* (U.S. Government Printing Office, Washington, D.C., 1962; Mir, Moscow, 1968, 561 pp.).
[6] *Handbook of Physical Quantities* edited by I. S. Grigor'ev and E. Z. Meĭlikhov [in Russian], Énergoatomizdat, Moscow (1991), 1232 pp.

Translated by R. M. Durham

# Generation of subnanosecond superradiance pulses in the short-wavelength part of the millimeter range

M. I. Yalandin, V. G. Shpak, S. A. Shunaĭlov, M. R. Ul'maskulov, N. S. Ginzburg, I. V. Zotova, A. S. Sergeev, A. D. R. Phelps, A. W. Cross, K. Ronald, and S. M. Wiggins

*Institute of Electrophysics, Urals Branch of the Russian Academy of Sciences, Ekaterinburg*
*Institute of Applied Physics, Russian Academy of Sciences, Nizhniĭ Novgorod*
*Strathclyde University, Glasgow, UK*
(Submitted July 12, 1999)
Pis'ma Zh. Tekh. Fiz. **25**, 1–7 (December 12, 1999)

Results of a simulation are presented and experimental observations of the generation of superradiance pulses in the 4 and 2 mm wavelength ranges as a result of the rectilinear motion of a subpicosecond high-current electron beam through a periodic retarding system are described. In the 4 mm range the microwave pulse power reached 10–15 MW with a duration of 150 ps. © *1999 American Institute of Physics.* [S1063-7850(99)00112-3]

Theoretical and experimental investigations of the generation of ultrashort electromagnetic pulses in the 8 mm range as a result of superradiance effects are described in Refs. 1–4. Various superradiance mechanisms have been studied, including cyclotron, undulator, and Čerenkov. A maximum radiation power of up to 60 MW in 300 ps pulses was achieved for the Čerenkov mechanism when a subnanosecond electron beam formed by a high-current RADAN accelerator[5] was injected into a periodic retarding structure. Synchronous interaction took place with the first reciprocal harmonic of the wave $E_{01}$. The direction of the wave group velocity was the opposite of the translational motion of the particles. A strong (up to 5 T) static magnetic field generated by a superconducting solenoid was used to achieve pulse-periodic operation at an accelerator cycle frequency up to 25 Hz.

The present paper describes the results of the next stage of the investigations in which we observed the generation of subpicosecond superradiance pulses in the short-wavelength part of the millimeter range at frequencies of 75 and 150 GHz. In these experiments we used our previous experience of studying short-wavelength relativistic backward-wave tubes supplied by electron beams of several nanoseconds duration which can produce steady-state generation.[6]

As in our previous experiments in the 8 mm range,[4] an accelerator based on a RADAN 303 high-voltage generator with a subnanosecond slicer was used to inject an electron beam having a duration of 0.5–1.5 ns, 0.5–1.5 kA current, and electron energy up to 250 keV (Ref. 5). A tubular cross-section beam was generated in a magnetically insulated coaxial vacuum diode having a graphite explosive-emission cathode. A Tektronix 7250 digitizing oscilloscope and an S7-19 high-speed oscilloscope having recording bands of 7 and 5 GHz, respectively, were used to record the subnanosecond signals from the voltage (capacitive probe), beam current (Faraday cup), and microwave power detectors (hot-carrier germanium detector).

The high-current electron beams were transported through the interaction space in the static magnetic field of a superconducting magnet or a pulsed solenoid of up to 5 T. The working space was a section of a corrugated waveguide having seventeen corrugation periods. The depth of the corrugation decreased smoothly over the final periods, ensuring matching with the output electrodynamic channel. At the cathode end, the interaction space was bounded by a supercritical constriction and after being reflected from this, the generated electromagnetic pulse was emitted in the direction of the electron translational motion. For the experiments in the 4 mm range the average waveguide diameter was 3.75 mm and the corrugation period was selected as 1.7 mm with a depth of 0.37 mm. As in the investigations of relatively long-pulse generators,[6] for the experiments in the 2 mm range these geometric dimensions were halved.

The generation process was first modeled using the KARAT code.[7] The geometry of the system was selected to correspond to the real experimental conditions (Fig. 1). Thus, the modeling included the formation of the electron pulse in the magnetically insulated coaxial diode. We assumed that the cathode has unlimited emissivity and the current in the working space was determined self-consistently. For the configuration shown in Fig. 1, which corresponds to the experi-

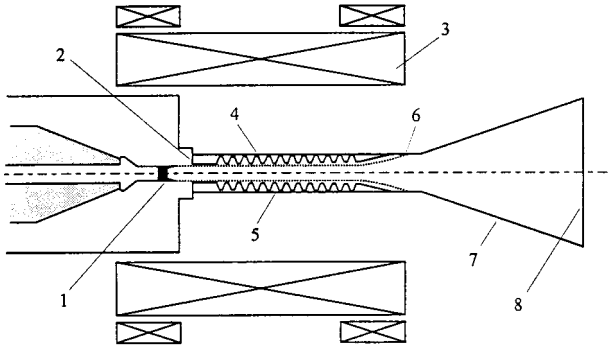


FIG. 1. Schematic of experiment: *1* — cathode, *2* — anode unit, *3* — superconducting solenoid windings, *4* — vacuum chamber, *5* — corrugated retarding system, *6* — electron beam collector, *7* — horn antenna, and *8* — vacuum microwave window.

 © 1999 American Institute of Physics

mental conditions in the 4 mm range, when a 250 kV voltage pulse was fed into the coaxial supply line, the current in the working space reached 800 A which was in good agreement with the experimental data. Figure 2a gives the calculated time dependence of the radiation power, which indicates that as an electron bunch passes through the corrugated waveguide, it emits a short electromagnetic pulse having a half-height duration of less than 150 ps and a peak power up to 30 MW (it should be noted that the power averaged over the high-frequency period is half the instantaneous power shown in Fig. 2). In this case, the output radiation had the structure of an $E_{01}$ wave with a central frequency of 75 GHz.

Figure 2b shows the results of modeling the radiation in the 2 mm structure. It should be noted that in the calculations the duration of the electron pulse was not reduced proportionately with the reduction in the wavelength and the length of the interaction space. For this reason the output radiation consists of a main pulse having a maximum peak power up to 15 MW and a series of subsequent peaks of lower amplitude. According to the results of the modeling, the duration of the electron pulse should be reduced to 0.2–0.3 ns to isolate the main pulse. At this stage of the experimental investigations, the duration of the electron pulse was not reduced because a decrease in the duration of the accelerating voltage pulse using a clipping spark gap would involve an appreciable drop in the amplitude of the accelerating voltage.

Figure 3a shows an oscilloscope trace of the microwave pulse in the 4 mm range. It can be seen that the pulse rise time does not exceed 120 ps. The angular distribution of the radiation corresponded to the excitation of the $E_{01}$ mode. Measurements of the absolute peak power were made by integrating over the angular distribution of the readings from

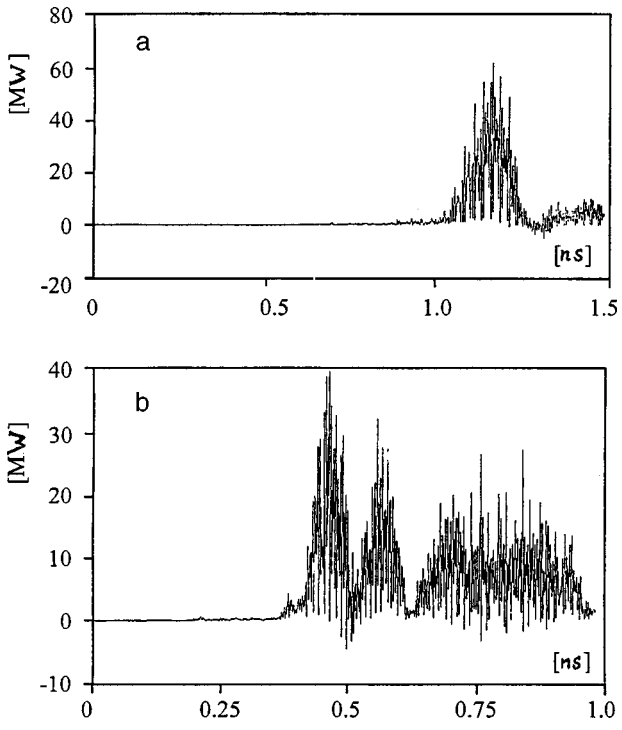


FIG. 2. Numerical simulation of the generation of superradiance pulses in the 75 GHz range (a) and in the 150 GHz range (b).

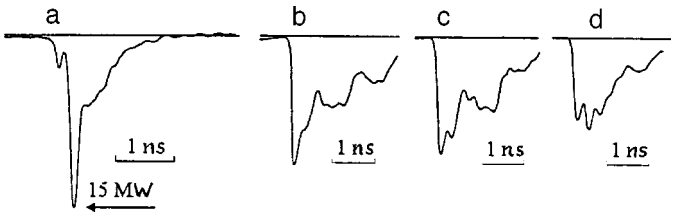


FIG. 3. Subnanosecond microwave pulse in the 75 GHz range (a) and change in the profile of microwave pulses in the 150 GHz range as the duration increases and the amplitude of the beam current pulse decreases (b–d).

a detector which was calibrated using a 4 mm relativistic backward-wave tube having a pulse duration of 3 ns (Ref. 8) and a calorimeter whose design is similar to that described in Ref. 9. From these measurements the peak power of the radiation pulses can be estimated as 10–15 MW. These pulses were generated using a cathode accelerating voltage of 250 kV, an injection current of 800 A, an electron beam duration of 0.6–0.7 ns, and a guiding magnetic field of 3.5 T. It should be noted that because of constraints on the pass band of the cable delay line of the oscilloscopes, the fundamental characteristics (rise time, duration, and amplitude) of a short $\sim$150 ps pulse were significantly distorted in the experiments. In this context, this estimate of the peak power should be regarded as the lower limit of the real value. The high peak power of the electromagnetic pulses was also confirmed by the observation of rf breakdown of air when radiation was concentrated in a circular cross-section, conical receiving horn having an exit diameter of 8 mm. However, unlike the experiments in the 8 mm range,[4] the observation of microwave breakdown in the field of the $E_{01}$ wave at 75 GHz prevents us from making any additional estimates of the peak power because of the lack of experimental data on the breakdown strength of air for $\sim$100 ps pulses.

In order to generate microwave pulses in the 150 GHz range, the electron energy was reduced to 180–200 keV. This was required for a cathode 1.2 mm in diameter to prevent any loss of current caused by strong collimation of the beam on entry to the retarding structure, whose drift channel had a diameter of only 1.5 mm. A reduction in the accelerating voltage reduces the transverse velocities of the electrons emitted by the cathode. It is important to note that a transporting field of 2.5 T was used in the experiments with pulses in the 150 GHz range. Figure 3b shows a 150 GHz microwave pulse obtained under conditions when only the electrons emitted at the tip of the accelerating pulse can interact synchronously with the wave $E_{01}$. The measured rise time of the microwave pulse was 75 ps which coincided with the frequency limit of the S7-19 oscilloscope tube. These data were consistent with the numerical calculations (Fig. 2b), which for 150 GHz predicted a half-height duration of 70 ps. However, calibrating the oscilloscope, the cable delay line, and other components of the channel using a 100 ps test pulse showed that the amplitude of the signal from the microwave detector was by a factor of least 2.5. No absolute calibration of the microwave detector was made in the 2 mm range. However, assuming that the deterioration in the detec-

tor sensitivity on transition from the 4 mm to the 2 mm range is approximately the same as that on transition from the 8 mm to the 4 mm range, a lower estimate of the peak power of the 2 mm radiation may be 5–10 MW.

In our experiments the duration of the beam current pulse could be increased by simultaneously increasing the accelerating voltage but this was accompanied by a partial loss of current as a result of collimation. The microwave pulses thus obtained are shown in Figs. 3c and 3d. As a result, in accordance with the numerical modeling data (see Fig. 2b), the generated radiation is a series of several pulses. On account of the frequency constraints of the measuring system we postulate that the percent modulation of the pulses is far greater than that shown in Figs. 3c and 3d.

This work was supported by the RFBR, Grant No. 98-02-17308.

[1] N. S. Ginzburg, I. V. Zotova, A. S. Sergeev, I. V. Konoplev, A. D. R. Phelps, A. W. Cross, S. J. Cooke, V. G. Shpak, M. I. Yalandin, S. A. Shunailov, and M. R. Ulmaskulov, Phys. Rev. Lett. **78**, 2365 (1997).
[2] N. S. Ginzburg, I. V. Zotova, Yu. V. Novozhilova, A. S. Sergeev, M. R. Ul'maskulov, V. G. Shpak, S. A. Shunaĭlov, M. I. Yalandin, A. D. R. Phelps, A. W. Cross, and S. J. Cooke, Izv. Vyssh. Uchebn. Zaved, Prikl. Nelin. Dinam. **6**(1), 38 (1998).
[3] V. G. Shpak, M. I. Yalandin, S. A. Shunailov, N. S. Ginzburg, I. V. Zotova, A. S. Sergeev, A. D. R. Phelps, A. W. Cross, and S. M. Wiggins, Dokl. Akad. Nauk **365**(1), 50 (1999).
[4] N. S. Ginzburg, Yu. V. Novozhilova, A. S. Sergeev, M. R. Ul'maskulov, V. G. Shpak, S. A. Shunaĭlov, M. I. Yalandin, A. D. R. Phelps, A. W. Cross, and S. M. Wiggins, V. Khi, K. Ronald, and V. P. Tarakanov, Pis'ma Zh. Tekh. Fiz. **24**(18), 7 (1998) [Tech. Phys. Lett. **24**, 709 (1998)].
[5] V. G. Shpak, S. A. Shunailov, M. R. Ulmaskulov, M. I. Yalandin, I. V. Pegel, and V. P. Tarakanov, in *Proceedings of the 11th Conference on High Power Particle Beams, BEAMS'96* (Prague, Czech Republic, 1996), pp. 913–916.
[6] N. M. Bykov, S. D. Korovin, G. A. Mesyats, V. G. Shpak, and M. I. Yalandin, Pis'ma Zh. Tekh. Fiz. **11**, 541 (1985) [Sov. Tech. Phys. Lett. **11** (1985)].
[7] V. P. Tarakanov, *User's Manual for Code KARAT*, Berkley Research Associates, Springfield, VA (1992).
[8] M. I. Yalandin, G. A. Mesyats, V. G. Shpak, G. T. Smirnov, and S. A. Shunailov, in *Proceedings of the SPIE International Symposium on Intense Microwave Pulses, Los Angeles, CA, 1993*, Proc. SPIE **1872**, 333 (1993).
[9] N. M. Bykov, V. P. Gubanov, A. V. Gunin, S. D. Korovin, V. V. Rostov, and M. I. Yalandin, Prib. Tekh. Éksp. No. 6, 107 (1987).

Translated by R. M. Durham

# Characteristic features of the amplification of short electromagnetic pulses during propagation along steady-state electron beams

N. S. Ginzburg, I. V. Zotova, and A. S. Sergeev

*Institute of Applied Physics, Russian Academy of Sciences, Nizhniĭ Novgorod*
(Submitted July 26, 1999)
Pis'ma Zh. Tekh. Fiz. **25**, 8–15 (December 12, 1999)

Specific characteristics of the amplification of short electromagnetic pulses propagating along a steady-state nonequilibrium electron beam whose group velocity differs from the particle translational velocity are studied. It is shown that as a result of one of the pulse leading edges being continuously supplied with electrons having no initial modulation, a high level of amplitude is achieved, substantially exceeding the saturation level for the amplification of quasisteady-state signals. © *1999 American Institute of Physics.* [S1063-7850(99)00212-8]

At present serious attention is being paid to the use of superradiance effects[1–7] to generate ultrashort electromagnetic pulses. In particular, the generation of pulses having a peak power of 60 MW and duration of 300 ps in the 8 mm range and 10–15 MW and 150 ps in the 4 mm range using this mechanism is described in Refs. 5–7. Similar pulses were generated as a result of the rectilinear motion of a 220 keV, 1.5 kA, 0.8 ns electron bunch produced by the RADAN high-current accelerator with a subnanosecond slicer, through a retarding structure in the form of a weakly corrugated waveguide. In this context it is of considerable interest to study the possibility of further increasing the peak power of pulses and reducing their effective duration. It will be shown subsequently that this possibility can be realized as a result of the propagation and amplification of pulses in a steady-state active medium formed by a nonequilibrium electron beam. A necessary condition is that the pulse group velocity should differ from the translational velocity of the particles to ensure that one of the pulse leading edges is continuously supplied with electrons having no initial modulation (apart from the noise component).

In the present paper the characteristics of the amplification of short electromagnetic pulses are studied using a Čerenkov traveling-wave-tube amplifier with a quasi-cw electron beam under phase-synchronism conditions

$$\omega = hV_{\parallel}, \tag{1}$$

where $\omega$ is the frequency, $h$ is the longitudinal wave number of the synchronous harmonic of the field, and $V_{\parallel}=\beta_{\parallel}c$ is the electron translational velocity.

We express the longitudinal component of the electric field of the synchronous wave in the form

$$E_z = \mathrm{Re}\{E_z^s(\mathbf{r}_\perp)A(z,t)\exp[i\omega t - uhz]\}, \tag{2}$$

where $E_z^s(\mathbf{r}_\perp)$ is the transverse field distribution which coincides with one of the modes of the electrodynamic system, $A(z,t)$ is the complex amplitude of the field which varies slowly with respect to time and the longitudinal coordinate, and the carrier frequency $\omega$ is taken to be the exact phase-matching frequency. Then, using the following as independent variables

$$Z = z\omega/c, \quad \zeta = (\omega/c)(t - z/V_{\parallel})(1/V_{gr} - 1/V_{\parallel})^{-1},$$

the amplification of the electromagnetic pulses by the electron beam under the phase-synchronism conditions (1) may be described using the system of equations:

$$\left[\frac{\partial}{\partial Z} + \frac{\partial}{\partial \zeta}\right]\alpha = J, \quad J = G\frac{1}{\pi}\int_0^{2\pi} e^{-i\theta}d\theta_0,$$

$$\frac{\partial \gamma}{\partial Z} = -\mathrm{Re}\,(\alpha e^{i\theta}), \tag{3}$$

$$\frac{\partial \theta}{\partial Z} = \frac{1}{\sqrt{1-\gamma^{-2}}} - \frac{1}{\sqrt{1-\gamma_0^{-2}}}$$

with the boundary conditions

$$\alpha|_{Z=0} = \alpha_0(\zeta)e^{i\delta\zeta}, \quad \theta|_{Z=0} = \theta_0 \in [0, 2\pi], \quad \gamma|_{Z=0} = \gamma_0.$$

Here the following dimensionless variables and parameters are introduced: $\alpha = eAE_{s_z}(R_0)/mc\omega$ is the amplitude of the longitudinal wave component synchronous with the beam ($R_0$ is the injection radius), $\theta = \omega t - hz$ is the phase of the electrons relative to this wave, $E = mc^2\gamma$ is the electron energy, $V_{gr} = \beta_{gr}c$ is the wave group velocity, $G$ is a parameter proportional to the beam current and the electron–wave coupling impedance, the function $\alpha_0(\zeta)$ defines the initial profile of the electromagnetic pulse, and $\delta = \omega_s - \omega/\omega \times (\beta_{gr}^{-1} - \beta_{\parallel}^{-1})$ describes the detuning of the input signal frequency $\omega_s$ from the carrier frequency.

In order to illustrate characteristic features of the mechanism for the amplification of short electromagnetic pulses propagating along a steady-state electron beam, Fig. 1 shows the characteristics of the electrons $\zeta = \mathrm{const}$ and the wave $\zeta = Z + \mathrm{const}$ on the $(Z,\zeta)$ plane (to be specific we assume that the particle translational velocity is higher than the wave group velocity). Let us assume that an electromagnetic pulse of initial duration $T$ is incident on the system. It can be seen from the diagram that over the entire interaction length the

 © 1999 American Institute of Physics

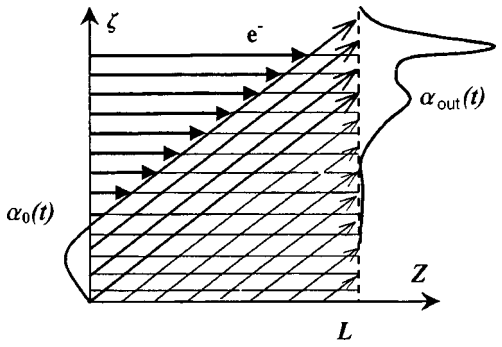


FIG. 1. Diagram showing characteristic features of the amplification of short electromagnetic pulses propagating along a steady-state electron beam. The straight lines give the characteristics of the electron beam $\zeta = \text{const}$ and the electromagnetic pulse $\zeta = Z + \text{const}$.

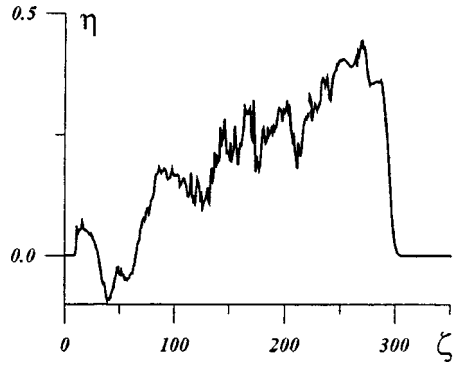


FIG. 3. Energy transfer efficiency for electrons involved in amplifying the electromagnetic pulse.

trailing edge of the electromagnetic pulse $\zeta = Z + T$ will intersect the characteristics of electrons which ideally have no initial modulation, and this should increase the field at the pulse trailing edge, as will be shown subsequently.

Figure 2a shows the space–time distribution of the amplitude of the rf field obtained by means of a numerical simulation of Eq. (3) when a rectangular electromagnetic pulse is applied to the system and the frequency of the incident signal coincides with the exact phase-synchronism frequency $\delta = 0$. It can be seen that at the trailing edge of the electromagnetic pulse the field amplitude increases considerably faster than in its central section, for which this amplitude is limited by factors characteristic of the amplification of steady-state monochromatic signals (capture of electrons by the wave, and so on). At the same time, the trailing edge of the electromagnetic pulse is continuously supplied with

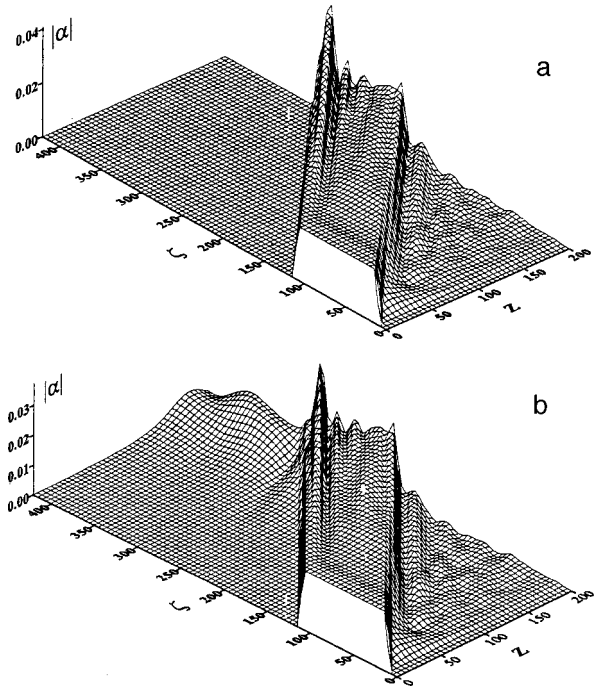


FIG. 2. Space–time evolution of the pulse amplitude during propagation in an ideal electron beam exhibiting no noise modulation: $G = 2.5 \times 10^{-4}$, $\gamma_0 = 1.4$ (a). The same in the presence of noise modulation $r = 0.03$ (b).

''fresh'' electrons which accelerate its leading edge. As a result, the mechanisms for saturation of the amplitude growth of this trailing edge are considerably weaker. It can be seen from Fig. 2a that the maximum amplitude of the central part of the pulse is 0.025 whereas for a normalized length of the working space $L = 200$, the maximum amplitude of the pulse at the trailing edge reaches 0.04 for an input amplitude of 0.02. This amplitude may be increased further by increasing the length of the working space, but this is accompanied by a reduction in the duration of the main pulse. It is important to stress that Fig. 2a corresponds to the situation when the initial signal level $\alpha_0$ exceeds the saturation level in terms of steady-state theory (in this case this level is 0.01). Nevertheless, the peak amplitude gain is $\sim 2$ and the power gain is therefore $\sim 4$. Note that when a weaker input signal is applied and the amplification process includes a linear stage, the gain may be considerably higher. Another possible method of increasing the gain involves detuning the frequency of the incident electromagnetic pulse $\omega_s$ from the exact phase-synchronism frequency $\omega$. A numerical simulation shows that for the optimum detuning parameter $\delta = -0.1$ and a given length of interaction space the peak amplitude of the output pulse reaches 0.06.

Figure 3 shows the energy transfer efficiency for electrons involved in amplifying the electromagnetic pulse. It can be seen that for some fractions the efficiency exceeds 40%. Note that for the selected parameters the efficiency for the amplification of steady-state signals is of the order of 15%.

This mechanism for the amplification of radiation at the pulse leading edge may be impeded by the buildup of intrinsic noise inevitably present in a beam, which must lead to modulation of the electron beam with a phase uncorrelated with that being amplified by the signal. In order to simulate the influence of noise, the initial phase of the electrons was defined as $\theta|_{Z=0} = \theta_0 + r\cos[\theta_0 + \varphi(\zeta)]$, where the modulation amplitude $r$ was assumed to be constant and the phase $\varphi$ was randomized over time. Figure 2b shows the space–time distribution of the field allowing for the amplification of the noise. It can be seen that if the initial amplitude of the electromagnetic pulse being amplified is fairly high, then although the influence of the noise reduces the peak amplitude of the pulse by 10–15%, the amplification process is never-

theless still fairly efficient. Note that the influence of noise can be reduced by introducing some detuning of the pulse frequency from the carrier frequency.

To conclude, we shall estimate the possibility of amplifying a 300 ps, 40 MW, 38 GHz pulse in an amplifier based on the Čerenkov interaction mechanism. Let us assume that the interaction space is a waveguide 1 cm in diameter and 25 cm long, partly filled with a dielectric of permittivity $\varepsilon \sim 3$. The thickness of the dielectric insert is 0.2 cm. For a particle energy of 200 keV, current 200 A, and an injection radius of 0.15 cm, the coupling parameter is $G = 2.5 \times 10^{-4}$ (Ref. 7). In terms of dimensionless variables, the initial signal amplitude is $\alpha_0 = 0.02$, the pulse duration is $T \sim 100$, and the normalized length of the interaction space is $L \sim 200$. According to Fig. 2a, the peak power can be amplified four times over this length, i.e., the output pulse power may reach 160 MW. At the same time, the effective pulse duration must be reduced (to 50 ps at half-height). Note that the peak power of the microwave pulse is higher than the electron beam power of 40 MW, but this does not contradict the energy conservation law because some slippage of the electromagnetic pulse relative to the electrons occurs during the amplification process, so that different fractions of the electron beam contribute to the increase in the peak pulse amplitude. Although the efficiency of each fraction is relatively high (Fig. 3), it is still less than unity.

In practical terms this process may be implemented by synchronizing two RADAN accelerators[8,9] one forming a subnanosecond electron beam by using slicers and the other generating a beam of 4–5 ns duration. The first accelerator is used to generate the superradiance pulses and the second to amplify them. Naturally, periodic retarding structures in which the electron beam interacts with a slow spatial harmonic may be used as the retarding system. A similar 35 GHz amplifier was described in Ref. 10. It can be deduced from an analysis of the dispersion diagrams that in an amplifier using the first positive spatial harmonic, the particle translational velocity is higher than the wave group velocity and, as follows from the preceding analysis, the amplitude of the field should increase appreciably at the leading edge of the electromagnetic pulse, rather than at the trailing edge.

This work was supported by the RFBR, Grant No. 98-02-17308.

The authors are grateful to M. I. Yalandin for stimulating discussions.

[1] R. H. Bonifacio, C. Maroli, and N. Piovella, Opt. Commun. **68**, 369 (1988).
[2] R. H. Bonifacio, N. Piovella, and B. W. J. McNeil, Phys. Rev. A **44**, 3441 (1991).
[3] D. A. Jaroszynski, R. J. Bakker, A. F. G. van der Meer, D. Oepts, and P. W. van Amersfoort, Phys. Rev. Lett. **70**, 3412 (1993).
[4] N. S. Ginzburg, A. S. Sergeev, I. V. Zotova *et al.*, Phys. Rev. Lett. **78**, 2365 (1997).
[5] N. S. Ginzburg, Yu. V. Novozhilova, A. S. Sergeev *et al.*, Pis'ma Zh. Tekh. Fiz. **24**(18), 7 (1998) [Tech. Phys. Lett. **24**, 709 (1998)].
[6] V. G. Shpak, M. I. Yalandin, N. S. Ginzburg, I. V. Zotova, A. D. R. Phelps, A. W. Cross, and S. M. Wiggins, Dokl. Akad. Nauk **365**(1), 50 (1999).
[7] N. S. Ginzburg, I. V. Zotova, Yu. V. Novozhilova *et al.*, Izv. Vyssh. Uchebn. Zaved. Prikl. Nelin. Dinam. **6**(1), 38 (1998).
[8] M. I. Yalandin, V. G. Shpak, S. A. Shunailov, and M. R. Ulmaskulov, in *Proceedings of the XVII-th International Symposium on Discharges and Electrical Insulation in Vacuum, Berkeley, CA*, 1996, Vol. 2, pp. 635.
[9] V. G. Shpak, S. A. Shunaĭlov, M. R. Ul'maskulov *et al.*, Pis'ma Zh. Tekh. Fiz. **22**(7), 65 (1996) [Tech. Phys. Lett. **22**, 297 (1996)].
[10] A. S. Elchaninov, S. D. Korovin, G. A. Mesyats, V. V. Rostov, V. G. Shpak, and M. I. Yalandin, in *Proceedings of the Sixth International Conference on High-Power Particle Beams, BEAMS-86, Kobe, Japan, 1986*, pp. 552–555.

Translated by R. M. Durham

# Observation of anomalous transmission of x-rays in tungsten single crystals

I. K. Bdikin, S. I. Bozhko, V. N. Semenov, I. A. Smirnova, V. G. Glebovskiĭ, S. N. Ermolov, and V. Sh. Shekhtman

*Institute of Solid-State Physics, Russian Academy of Sciences, Chernogolovka*
(Submitted July 27, 1999)
Pis'ma Zh. Tekh. Fiz. **25**, 16–21 (December 12, 1999)

Results of observations of the anomalous transmission of x-rays in tungsten single crystals are presented. The dislocation density $(2-4)\times 10^5\ \mathrm{cm}^{-2}$ was determined from an analysis of the dynamic diffraction characteristics. © *1999 American Institute of Physics.* [S1063-7850(99)00312-2]

Studies of the formation of an x-ray wave field in crystals (effects of dynamic scattering theory) are currently of topical interest[1,2] although the first observations of anomalous transmission were made more than fifty years ago. The necessary high degree of structural perfection is only achieved for a limited number of crystals, such as silicon, germanium, and related families; almost no observations of dynamic effects have been made in metals. Studies of anomalous transmission in transition metals are of considerable interest, particularly tungsten which has a simple structure and high absorption coefficient.

The growth of perfect single crystals of refractory metals presents difficulties because of the low defect formation energy and the stringent constraints on the level of temperature gradients. Modern methods of preparing tungsten single crystals can produce samples having a dislocation density of less than $10^5\ \mathrm{cm}^{-2}$, and these were successfully synthesized at the Institute of Solid-State Physics of the Russian Academy of Sciences. In the present study we obtained experimental results which indicate that dynamic diffraction effects are observed in tungsten crystals having a high degree of structural perfection.

Tungsten single crystals of 99.95% purity were grown by electron-beam zone refining.[3] The single-crystal ingots underwent plastic deformation followed by recrystallization annealing at 2500 °C in vacuum. Plates measuring $20\times 10\times 3\ \mathrm{mm}^3$ were then prepared by electric-spark cutting, mechanical grinding, and electropolishing such that the broad face of the plates coincided with the (110) plane to within $\pm 0.1°$.

A classical system (Fig. 1a) was used to record the anomalous transmission of x-rays (Borrmann effect). A fine-focus tube having a focus measuring $50\times 50\ \mu\mathrm{m}^2$ was used as a source of a diverging x-ray beam. The distance between the sample and the photographic film was 10 cm and that between the source and the sample was 18 cm (Fig. 1a). An asymmetric extraction geometry (the distance between the source and the sample is not equal to that between the sample and the photographic film) was used to eliminate focusing of diffracted rays over the radiation spectrum. The forward transmitted beam $T$ (Fig. 1c) and the (110) reflection of the diffracted beam $R$ were recorded on the photographic film (Fig. 1b). Rocking curves were recorded in a dispersion-free system using a perfect silicon single crystal as the monochromator. Angular scanned topograms were obtained in the $\Theta-2\Theta$ scanning regime.

Figure 1 gives results of x-ray topographic studies of a tungsten crystal. The image in the forward beam is a shadow of the sample, which has the same profile (Fig. 1c). The fine vertical double lines on this shadow are the image of the characteristic Cu$K\alpha_{1,2}$ radiation transmitted by the crystal. Similar lines can be seen in the $R$ diffraction direction (Fig. 1b). These lines shift along the surface of the samples as it rotates. A diffractometric analysis of the waves propagating in the $R$ and $T$ directions (Fig. 2a and 2b) shows that the intensities ($T$) of the diffracted and forward transmitted beam are the same.

Calculations using kinematic theory show that for copper radiation and a sample thickness of 0.3 mm ($\mu t\sim 98$) the absorption is $10^{43}$. With the available radiation sources (no more than $10^7-10^8$ pulse/s) it is impossible to obtain a recordable transmission intensity.

A diverging x-ray beam is one where the angles of incidence of the x-rays on the sample differ for different parts of the sample. Thus, for a given wavelength the diffraction conditions are satisfied along a certain line on the surface of the sample. In the case of dynamic diffraction (perfect crystal), at points where the diffraction conditions are satisfied we observe amplification of the intensity in the transmitted beam, which is the same in the $R$ and $T$ directions. In the kinematic approximation (crystal containing defects), the intensity is suppressed. The fact that the transmitted radiation is recorded and the radiation intensity is the same in the diffracted and forward transmitted beams, together with the observation of amplification of the characteristic Cu$K\alpha_{1,2}$ radiation intensity in these directions indicate that the diffraction is of a dynamic nature. The observation of splitting of these beams into a Cu$K\alpha_{1,2}$ doublet and the shift as the sample rotates indicate that these beams are of diffraction origin and are not a topological characteristic of the sample.

Effects associated with the dynamic propagation of x-rays can only be observed in crystals for which the distance between dislocations does not exceed the extinction length $L$. Calculations for the (110) Cu$K\alpha$ reflection for a defect-free tungsten crystal give $L=1.7\ \mu$m, i.e., the critical dislocation density is $N=1/L^2=3.5\times 10^7\ \mathrm{cm}^{-2}$.

 © 1999 American Institute of Physics

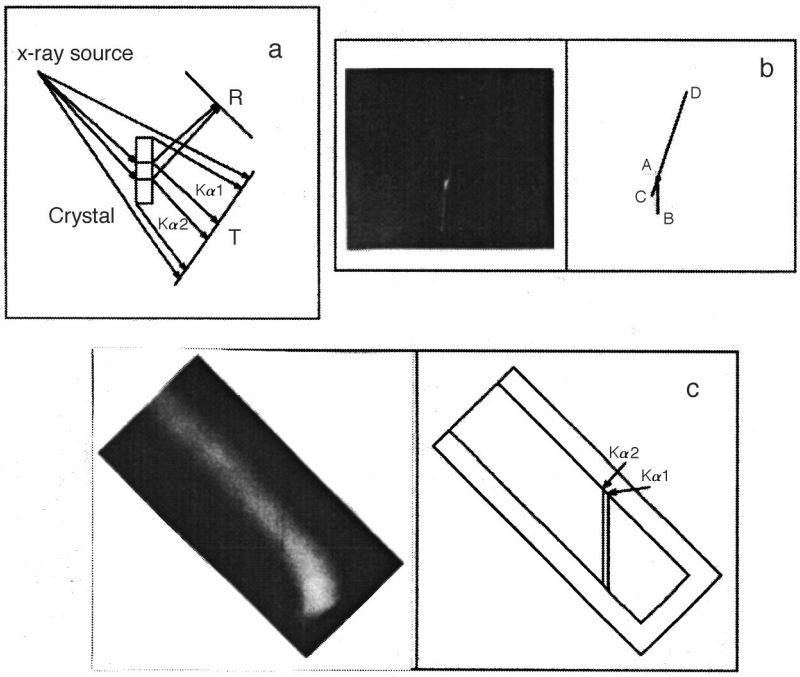


FIG. 1. Topograms of a tungsten single crystal, (110) reflection, Cu$K\alpha$ radiation: a — schematic of experiment, b — $R$ direction, the line $CD$ gives the image from the crystal edge in the continuous spectrum, the line $AB$ corresponds to the characteristic Cu$K\alpha_{1,2}$ lines; c — $T$ direction.

In order to determine the type of defects which predominate in our crystal and their density we recorded rocking curves for the (110) reflection in Bragg and Laue geometries and measured the interference damping factor $\mu_i$. In Laue geometry the width of the rocking curve is 34″, whereas in Bragg geometry the rocking curve is narrower and its width is 73″. The calculated values for these widths in a defect-free crystal[4] are 5.5″ and 48.6″ in Laue and Bragg geometries, respectively. Hence, the broadening of the rocking curves in a real crystal compared with a defect-free crystal is around 25″ for both rocking curves. Measurements of the absorption coefficient for diffracted molybdenum radiation give $\mu_i = 464.4\,\mathrm{cm}^{-1}$, while the calculations for a defect-free crystal give a value 25% lower, $369.2\,\mathrm{cm}^{-1}$.

The difference between the measured values of the rocking curve width and the coefficient of interference absorption from the calculated values for a defect-free crystal can be used to determine the dislocation density in our crystal. Estimates of the dislocation density using the width of the rocking curve[5] give $N = 2\times10^5\,\mathrm{cm}^{-2}$, and using the coefficient of interference absorption[6] $N = 4\times10^5\,\mathrm{cm}^{-2}$. These data show good agreement with the dislocation density determined using etch pits, $N = 5\times10^5\,\mathrm{cm}^{-2}$. Thus, the dislocation density in a real crystal is substantially lower than the critical density. Note that the dislocation density determined from the coefficient of interference absorption is higher than

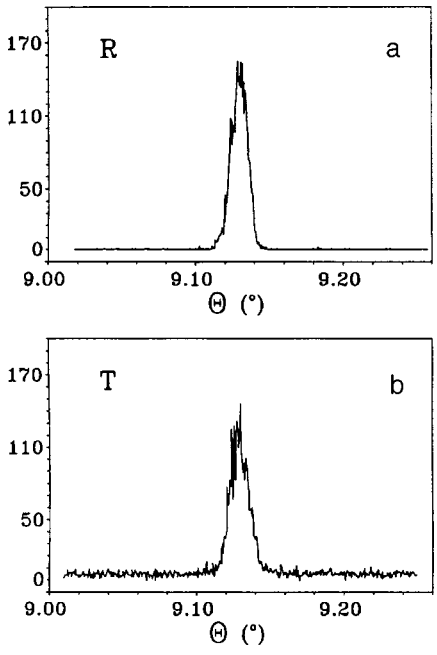


FIG. 2. Diffraction patterns of tungsten single crystal, (110) reflection, Θ scanning, Mo$K\alpha$1 radiation: a — $R$ direction, b — $T$ direction.

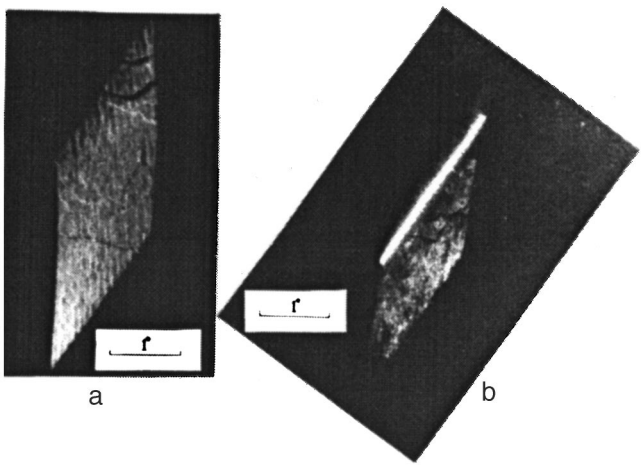


FIG. 3. Topogram of tungsten single crystal, (110) reflection, $\Theta-2\Theta$ scanning, Cu$K\alpha$ radiation: a — reflection geometry, b — transmission geometry, $R$ direction.

that obtained from the rocking curve width. This is evidently attributable to the presence of defects in the crystal (such as point defects) which increase the absorption but make no contribution to the rocking curve width.[7]

The observation of the Borrmann effect allows us to obtain an angular-scanned transmission topogram for our crystal (Fig. 3a), which reveals blocks larger than 1–2 mm. A comparison with the reflection topogram (Fig. 3b) suggests that the block structure exhibits similar reflection but the transmission topogram has a higher image contrast as a result of the dynamic narrowing of the diffracted beam for a thick crystal (the smaller width of the rocking curve in Laue geometry).

The authors are grateful to V. B. Molodkin and E. V. Shulakov for useful discussions and V. V. Lomeĭko for growing the single crystal.

This work was supported by Projects of the International Science and Technology Center, No. 437 and the Ministry of Sciences No. 2.8.99 (under the Program ''Surface Atomic Structures'').

[1] V. V. Kvardakov, V. A. Somenkov, V. Paulus, G. Heger, and S. Piñol, JETP Lett. **60**, 731 (1994).
[2] M. V. Koval'chuk, A. Ya. Kreĭnes, Yu. A. Osip'yan, V. V. Kvardakov, and V. A. Solomenkov, JETP Lett. **65**, 734 (1997).
[3] V. G. Glebovsky, V. N. Semenov, and V. V. Lomeyko, J. Cryst. Growth **87**, 142 (1988).
[4] Z. G. Pinsker, *X-Ray Crystal Optics* (Nauka, Moscow, 1982).
[5] É. G. Sheĭkhet, O. N. Efimov, and N. V. Veselovskaya, Fiz. Tverd. Tela (Leningrad) **18**, 272 (1972) [Sov. Phys. Solid State **18** (1972)].
[6] V. I. Kisin and I. V. Stratan, Fiz. Tverd. Tela (Leningrad) **12**, 1274 (1970) [Sov. Phys. Solid State **12** (1970)].
[7] M. A. Krivoglaz, *Diffraction of X-Rays and Neutrons in Nonideal Crystals* (Naukova Dumka, Kiev, 1983).

Translated by R. M. Durham

# Characteristics of cleavage fracture during interaction of nonlinear waves with the free surface of a copper single crystal

K. P. Zol'nikov, T. Yu. Uvarov, A. G. Lipnitskiĭ, D. Yu. Saraev, and S. G. Psakh'e

*Institute of Strength Physics and Materials Sciences, Siberian Branch of the Russian Academy of Sciences, Tomsk*

(Submitted July 9, 1999)
Pis'ma Zh. Tekh. Fiz. **25**, 22–27 (December 12, 1999)

A molecular dynamics method was used to study the interaction of isolated compression pulses with the (100) and (110) free surface in a copper monocrystallite. It is shown that this may be accompanied by cleavage fracture. Parameters of compression pulses which lead to cleavage processes are determined. © *1999 American Institute of Physics.* [S1063-7850(99)00412-7]

Studies of material behavior under high-energy pulsed action are an important problem in condensed-state physics.[1–3] High-speed mechanical loading, ion beam bombardment, and exposure to high-energy electron beams may have the result that the energy pumped into the material will propagate in this material in the form of nonlinear isolated waves.[4,5] Interaction of soliton-like waves with the free surface is accompanied by tensile stresses which may lead to so-called cleavage fracture. The values of the cleavage stresses are always higher than the corresponding values under static loading.[3,6] It should be noted that the nature of the fracture under dynamic loading differs substantially from that in static tests.

Despite numerous experiments and methods of measuring cleavage processes, the data obtained still exhibits an appreciable spread and even, in some cases, contradictory.[6] The difficulties encountered in the experimental investigations primarily arise from the transient nature of the phenomenon. In this context, a molecular dynamic modeling of the material behavior may prove extremely useful. With this aim the task for the present study was to investigate the anisotropy of cleavage phenomena in a copper single crystal when isolated nonlinear waves interact with the surface.

The calculations were made by a molecular-dynamics method[4,5,7] using the interatomic interaction potentials calculated by the embedded atom method.[8,9] The potential used in this study can describe with a high degree of accuracy many properties of free surfaces for various crystallographic planes, including the properties of vicinal surfaces (atomic structure,[9] formation and migration energies of point defects,[10] and phonon spectra[11]).

We modeled a copper crystallite having an ideal fcc structure and containing more than 12 000 atoms. The crystallite was constructed as a parallelepiped elongated in the direction of loading.

The boundary conditions were selected as follows. A stringent boundary condition was set on the loading side and a free surface on the other side. Periodic boundary conditions were used in directions perpendicular to the direction of application of the load.

We investigated the interaction between a propagating perturbation and the (100) and (110) free surfaces. These were chosen because of the different degrees of compression of the surface atomic planes [for the (100) direction for the last two planes the compression is 1.2% whereas for the (110) direction it is 4.5%]. In order to simulate the external loading, sample atoms from the impact region of the selected face were assigned a constant velocity in the direction being studied for $9.7\times10^{-16}$ s, which was $\sim 2-3\%$ of the total calculation time. The loading rate was varied between 1600 and 4300 m/s for the [100] direction and between 1400 and 2200 m/s for the [110] direction.

As a result of the loading, one or several isolated compression pulses form in the material (Fig. 1a) having a flat leading edge and propagating in the material without any change in shape or amplitude. The width of the pulses can vary between three and eight interplanar spacings and depends on its amplitude and crystallographic direction. For example, as the amplitude increases, the width decreases. The present authors have shown[12] that the energy of such a pulse is transferred in the direction of loading in a ballistic regime (without scattering).

In order to eliminate background perturbations, we defined the distribution of initial displacements and atomic velocities for which a single compression pulse forms.

As a result of the anisotropy in different directions, pulses of different amplitude form under the same loads in the [100] and [110] directions. For instance, at a loading rate of 1600 m/s a pulse having an amplitude of 1500 m/s forms in the [100] direction and a 2200 m/s pulse forms in the [110] direction. We also note that the propagation velocities of the pulses differ in the different directions (see Table I).

The calculations showed that cleavage processes begin at the free surfaces if the amplitude of an isolated compression pulse exceeds a threshold of 1500 m/s for the [100] direction and 1700 m/s for the [110] direction. As a result of the planar leading edge of the compression pulse, at above-threshold amplitudes one or several atomic surface planes begin to detach from the sample. For the [110] direction in the range of loads being studied, the last two atomic planes separated from the free surface as a single entity. For the [100] direction at relatively low load only the last plane becomes detached, but as the amplitude is increased, another plane is cleaved (Fig. 1b).

 © 1999 American Institute of Physics

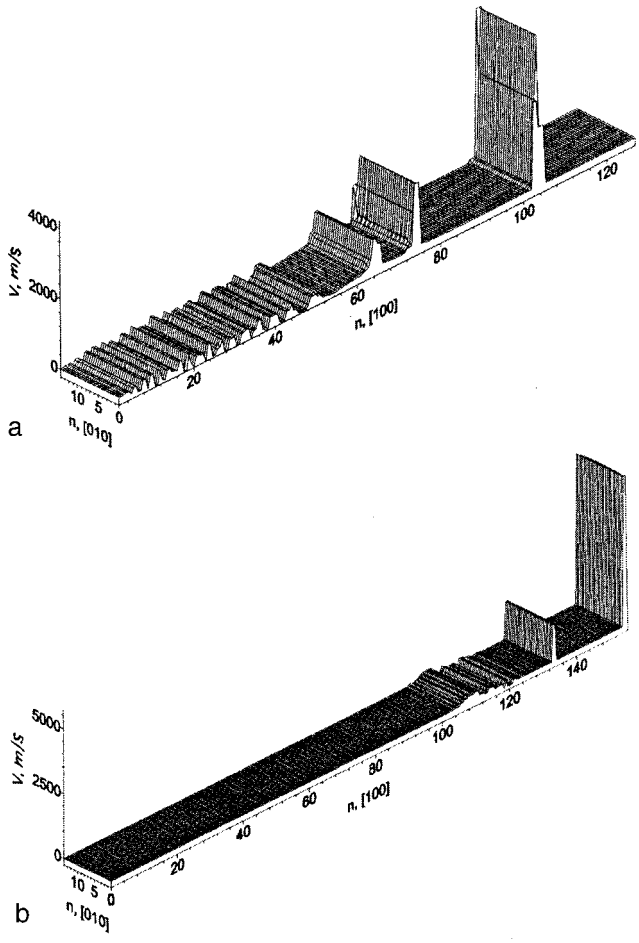


FIG. 1. Positions of compression pulses initiated by high-speed loading in copper: a — inside crystallite, b — after cleavage; *n* is the number of the atomic plane and *V* is the atomic velocity.

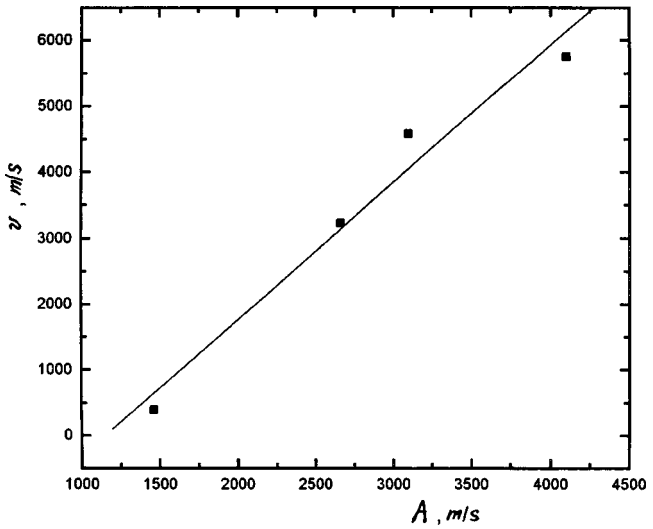


FIG. 2. Velocity *V* of cleaved section of crystallite as a function of the compression pulse amplitude *A* for the [100] direction.

As the amplitude of the cleaving pulse increases, the rate of detachment increases appreciably for both directions and approaches the propagation velocity of the pulse in the material (Fig. 2). This leads to an increase in the fraction of energy removed by the cleaved planes.

To sum up, we have shown that cleavage processes in copper monocrystallites are essentially anisotropic. This anisotropy is observed primarily in the difference between the threshold values of the cleaving stresses, the number of cleaved atomic planes, and the rates of detachment of the cleaved sections. Since we have shown[12,13] that high-energy bombardment of a material surface leads to the formation of isolated compression pulses, we may predict that the effect observed here will lead to nanoscopic cleavage from the rear surface of the sample. Thus, this nanoscopic cleavage may occur under ion implantation, under bombardment by high-energy pulsed high-current beams, and also under irradiation.

TABLE I. Pulse propagation velocity in sample as a function of amplitude and crystallographic direction.

| Direction | Amplitude *A*, m/s | Velocity in sample *V*, m/s |
|---|---|---|
| | 650 | 4750 |
| | 890 | 4800 |
| | 1350 | 5010 |
| 100 | 1790 | 5450 |
| | 2660 | 6100 |
| | 3100 | 6850 |
| | 4100 | 7760 |
| | 720 | 6000 |
| | 830 | 6180 |
| | 1110 | 6540 |
| 110 | 1610 | 7360 |
| | 1850 | 7630 |
| | 2180 | 7990 |

[1] Ya. B. Zel'dovich and Yu. P. Raizer, *Physics of Shock Waves and High-Temperature Hydrodynamic Phenomena*, Vols. 1, 2, (Academic Press, New York, 1966,1967; Nauka, Moscow, 1966).
[2] V. S. Nikiforovskiĭ and E. I. Shemyakin, *Dynamic Fracture of Solids* (Nauka, Novosibirsk, 1979).
[3] A. V. Bushman, G. I. Kanel', A. L. Ni, and V. E. Fortov, *Heat Physics and Dynamics of Intense Pulsed Action* [in Russian], Chernogolovka (1988).
[4] S. G. Psakh'e, K. P. Zol'nikov, and S. Yu. Korostelev, Pis'ma Zh. Tekh. Fiz. **21**(13), 1 (1995) [Tech. Phys. Lett. **21**, 489 (1995)].
[5] S. G. Psakh'e, K. P. Zol'nikov, and D. Yu. Saraev, Fiz. Goreniya Vzryva **33**(2), 43 (1997).
[6] G. I. Kanel', S. V. Razorenov, A. V. Utkin, and V. E. Fortov, *Shock-Wave Phenomena in Condensed Media* (Yanus–K, Moscow, 1966).
[7] S. G. Psakh'e, K. P. Zol'nikov, and D. Yu. Saraev, Pis'ma Zh. Tekh. Fiz. **24**(3), 42 (1998) [ Tech. Phys. Lett. **24**, 99 (1998)].
[8] S. M. Foiles, M. I. Baskes, and M. S. Daw, Phys. Rev. B **33**, 7983 (1986).
[9] A. V. Berch, A. G. Lipnitskiĭ, and E. V. Chulkov, Poverkhnost' No. 6, 23 (1994).
[10] S. V. Eremeev, A. G. Lipnitskii, A. I. Potekaev, and E. V. Chulkov, Phys. Low-Dimens. Semicond. Struct. No. 3/4, 127 (1997).
[11] G. G. Rusina, A. V. Berch, I. Yu. Sklyadneva, S. V. Eremeev, A. G. Lipnitskiĭ, and E. V. Chulkov, Fiz. Tverd. Tela (St. Petersburg) **38**, 1120 (1996) [Phys. Solid State **38**, 619 (1996)].
[12] K. P. Zol'nikov, R. I. Kadyrov, I. I. Naumov, S. G. Psakh'e, G. E. Rudenskiĭ, and V. M. Kuznetsov, Pis'ma Zh. Tekh. Fiz. **25**(6), 55 (1999) [Tech. Phys. Lett. **25**, 230 (1999)].
[13] S. G. Psakh'e, K. P. Zol'nikov, R. I. Kadyrov, G. E. Rudenskiĭ, Yu. P. Sharkeev, and V. M. Kuznetsov, Pis'ma Zh. Tekh. Fiz. **25**(6), 7 (1999) [Tech. Phys. Lett. **25**, 209 (1999)].

Translated by R. M. Durham

# Possibility of demonstrating a self-sustained fusion reaction in an ambipolar trap

G. I. Dimov

*G. I. Budker Institute of Nuclear Physics, Siberian Branch of the Russian Academy of Sciences, Novosibirsk*
(Submitted July 28, 1999)
Pis'ma Zh. Tekh. Fiz. **25**, 28–33 (December 12, 1999)

A brief description is given of an axisymmetric mirror trap to demonstrate ignition of a D–T plasma confined by ambipolar barriers. Key problems for this demonstration are ion pumping and suppression of instabilities in the thermal barriers. It is suggested that the fusion-fuel ions can be pumped away from the thermal barriers by exciting trapped-ion bounce oscillations at parametric resonances. © *1999 American Institute of Physics.*
[S1063-7850(99)00512-1]

In principle, an ambipolar trap can be used as the basis for several types of ambipolar fusion reactor. A completely axisymmetric ambipolar tandem-mirror reactor[1] is the most promising variant. In order to achieve complete axial symmetry, a high-pressure plasma ($\beta \sim 1$) must be confined in the trap whose magnetohydrodynamic (MHD) stability can be sustained by the conducting walls of the vacuum vessel and the finite ion Larmor radius effect.[2,3]

In order to demonstrate the feasibility of an ambipolar D–T reactor, it is possible to construct a mirror fusion system in the form of a reactor with a shortened central solenoid. Figure 1 shows the superconducting magnetic system and the plasma geometry in the mirror fusion system. The vacuum magnetic field is 2 T in the solenoid, 1.67 T in the thermal barriers ''*b*,'' 4.3 T in the ambipolar barriers ''*b*,'' 14 T in mirrors ''*m*'' and ''*h*,'' and 14.8 T in the exit mirror ''*m**.'' The total weight of the superconducting coils with the supporting structures is around 300 t, which is less than the corresponding weight of the coils in the LHD stellarator operating at the NIFS Institute (Japan).

The parameters of the D–T plasma in the solenoid are: density $n_s = 1.5 \times 10^{14}\,\mathrm{cm}^{-3}$, temperature $T_s = 25\,\mathrm{keV}$, $\beta = 0.85$, plasma radius 1 m (radius of vacuum wall 1.3 m), neutron load on wall $1.8\,\mathrm{MW/m^2}$, thermonuclear power, together with that released in blanket 24 MV/m. The depth of the thermal barriers is 112 kV while the depth of the ambipolar barriers is 105 kV. The plasma energy confinement parameter is $n\tau_\varepsilon = 1.8 \times 10^{14}\,\mathrm{cm}^{-3} \cdot \mathrm{s}$ for $n\tau_{\varepsilon\perp} \approx n\tau_{\varepsilon\parallel}$.

In the thermal barriers ''*b*'' the plasma density is $10^{13}\,\mathrm{cm}^{-3}$ and the hot electron temperature is 360 keV. In the ambipolar barriers ''*p*'' the plasma density is $5 \times 10^{13}\,\mathrm{cm}^{-3}$, the hot ion temperature 400 keV, and the electron temperature 77 keV. The values of $\beta_\perp$ are 0.7 and 0.65 in the ''*b*'' and ''*p*'' planes, respectively. The pressure ratio $p_\perp / p_\parallel$ is 1.9 and 2.4 in the ''*b*'' and ''*p*'' planes, respectively. An increase in $\beta_\perp$ and $p_\perp / p_\parallel$ improves the stabilization of the plasma by the conducting walls.

Several lowest MHD modes are stabilized by the walls of the vacuum vessel in the solenoid, the thermal barriers, and the ambipolar barriers. Higher MHD modes may be stabilized by the finite ion Larmor radius effect in the solenoid and the ambipolar barriers. The overall slow transverse drift of the plasma may be suppressed by various methods.[4]

The electron cyclotron resonance (ECR) heating power is $2 \times 70$ MW (38 MHz) in the thermal barriers and $2 \times 16.7$ MW (77 MHz) in the ambipolar barriers. The atomic injection power in the ambipolar barriers is $2 \times 3.8$ MW. The total power absorbed in the plasma of the tandem mirror traps is 176 MW. The ratio of the power generated in the solenoid to the power input to the end mirror traps is $Q \approx 4$. Prolonged testing of the mirror fusion system may be carried out without requiring any external electrical energy by using the generated thermonuclear energy. For a given specific neutron load on the wall, the capital cost of the shielding and blanket together with the heat extraction system per unit thermonuclear power will be no greater than that in any other magnetic-confinement fusion facility. The main power sources for particle heating in mirror traps are microwave generators in the frequency range 40–80 GHz. These generators should not be very expensive.

The system can be triggered by ECR heating in the thermal barriers ''*b*.'' In experiments using various mirror systems (ELMO, SM-1, STM) macroscopic stability of the electron populations, including disk-shaped, has been observed when these accumulate as a result of ECR heating to high $\beta \sim 1$. Thus, we can reasonably expect that populations of hot electrons will accumulate in the thermal barriers with above-critical $\beta$ after MHD stabilization by the walls, without any additional methods of stabilization. Then, hot ions from the atomic injection build up in the ambipolar barriers ''*p*'' and the electrons undergo ECR heating. At the same time, ions start to be pumped from the thermal barriers. As a result, we obtain an MHD-stable plasma with the initial confining barriers in the tandem mirror traps.

Then, D–T plasma accumulates and is heated in the solenoid. This plasma can be heated by supplying a power of $\sim 2$ MW for $\sim 100$ s by any suitable method. At the beginning of the buildup macroscopic stability of the plasma in the solenoid is sustained by the MHD-stabilizing end mirror systems. After being heated to fusion temperature and reaching $\beta \approx 0.8$, the D–T plasma in the solenoid becomes MHD stable and steady-state confining barriers are established in the end mirror systems. As the D–T plasma ignites in the solenoid, its initiating heating is terminated.

 © 1999 American Institute of Physics

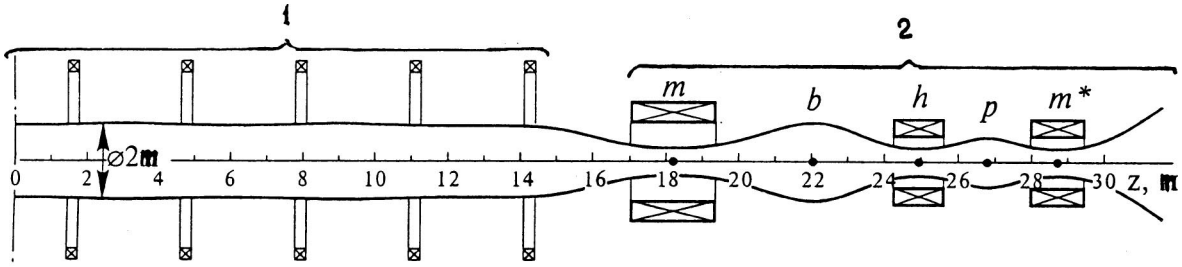


FIG. 1. Schematic of mirror fusion system (right half): *1* — solenoid and *2* — tandem mirror trap.

As the next stage it is proposed to construct a prototype with a high-temperature plasma—the PPU device. In order to reduce the cost of this device, the plasma diameter in the solenoid can be reduced to 1 m and its temperature lowered. The total length of PPU will be around 30 m with a central solenoid 12 m long. The total weight of the superconducting coils with the supporting structures will be around 50 t. The power absorbed in the end mirror systems will be reduced to $\sim 30$ MW.

The main physical problems should be solved experimentally using PPU, i.e., ion pumpout from the thermal barriers and suppression of drift ion instabilities in the end mirror systems. The main ions ($D^+$ and $T^+$ in a reactor) trapped in the thermal barriers should be returned to the solenoid along the magnetic field.[4] One possible method of achieving longitudinal return pumping of trapped ions is to excite longitudinal oscillations using parametric resonators. This may be accomplished by using coaxial coils with a relatively small ac current, positioned near the midplane ''*b*.'' The impurity ions can be removed from the thermal barriers by resonant low-frequency transverse magnetic fields over the radius into a halo at the plasma surface. The plasma density in the thermal barriers ''*b*'' and in the ambipolar barriers ''*p*'' should be reduced to the required value. The technology for fabricating compact superconducting mirror coils generating magnetic fields up to 14 T also needs to be developed. Experiments using PPU will be of decisive importance.

The first stage in the PPU project should involve carrying out relatively inexpensive experiments, such as: MHD plasma stabilization with high $\beta \sim 1$ in axisymmetric geometry, studies of drift ion stability in a deep mirror trap with longitudinal pumping of trapped ions, and ECR heating of the plasma electrons in the mirror trap to high $\beta$.

Successful experiments in the mirror fusion system will open up the way toward achieving a weakly radioactive D–$^3$He ambipolar fusion reactor. In order to develop a D–T reactor ($Q \sim 20$) the length of the central solenoid must be increased to 100–150 m (Ref. 5).

In the assumed tandem mirror systems, most of the power is dissipated in ECR heating of the electrons in the thermal barriers. Thermal barriers can be created spontaneously by drift ions without ECR heating of the electrons in the thermal barrier mirror traps. In this case, in the ''*b*'' midplane we have

$$\frac{n_{beth}}{n_s}\sqrt{\ln\frac{n_s}{n_{beth}}} \approx \frac{1}{\sqrt{\pi}}\left(1+\frac{n_{bitr}}{n_{bipas}}\right)\left(1+\frac{b_{bepas}}{n_{beth}}\right)^{-1}\frac{1}{R_{mb}},$$

where $n_{e\,th}$ and $n_{e\,pas}$ are the densities of the thermal and passing electrons, $n_{i\,tr}$ and $n_{i\,pas}$ are the densities of the trapped and passing ions, $R_{mb}$ is the ratio of the magnetic field in the entry mirror ''*b*'' ($B_m$) to the field in the thermal barrier ''*b*.'' For $B_m \sim 20$ T it is possible to achieve $R_{mb} \sim 30$. As a result, a very low density $n_{beth}$ is established and therefore a relatively large thermal barrier depth $\varphi = T_s \ln(n_s/n_{beth})$. Estimates indicate that in this case the absorption of energy in the tandem mirror systems is halved compared with that absorbed in the end mirror traps of the mirror fusion system described above. Superconducting input coils exciting the magnetic fields up to 20 T may be fabricated, but they are fairly expensive.

[1] D. E. Baldwin and B. G. Logan, Phys. Rev. Lett. **43**, 1318 (1979).
[2] H. L. Berk, H. V. Wong, and K. T. Tsang, Phys. Fluids **30**, 2681 (1987).
[3] Xing-Zhong Li, J. Kesner, and L. L. LoDestro, Nucl. Technol. **27**, 1259 (1987).
[4] G. I. Dimov, Fiz. Plazmy. **23**, 883 (1997) [Plasma Phys. Rep. **23**, 813 (1997)].
[5] G. I. Dimov, Trans. Fusion Technol. **35**(1T), 10 (1999).

Translated by R. M. Durham

# Measurement of linear velocity using a resonant ring interferometer with a low-coherence light source

V. V. Ivanov, M. A. Novikov, and V. M. Gelikonov

*Institute of Microstructure Physics, Russian Academy of Sciences, Nizhniĭ Novgorod*
*Institute of Applied Physics, Russian Academy of Sciences, Nizhniĭ Novgorod*
(Submitted July 19, 1999)
Pis'ma Zh. Tekh. Fiz. **25**, 34–42 (December 12, 1999)

It is demonstrated theoretically and experimentally that linear velocities of reflecting objects may be measured using a resonant ring interferometer with a low-frequency light source. The limiting sensitivity of this interferometer is estimated. It is shown that a resonant ring interferometer can be used to measure extremely low linear velocities corresponding to subhertz Doppler frequency shifts of light, which cannot be measured by conventional Doppler techniques based on direct measurements of the frequency difference between the initial and reflected waves. © *1999 American Institute of Physics.* [S1063-7850(99)00612-6]

Optical ring interferometers, which have conventionally been used to measure angular velocity, have recently found interesting new applications in science and engineering. For instance, the possibilities of using ring interferometers to measure linear velocities and displacements, in particular to detect gravitational waves, to measure liquid flow velocities,[1] and linear velocities of solids[2] are currently being actively pursued. Compared with the interferometers conventionally used to measure linear displacements, ring interferometers possess better noise stability and a lower level of technical noise. This is because in ring interferometers, changes in the optical length of the ring as a result of reciprocal optical effects, such as thermal expansion or mechanical noise, do not lead to any substantial change in the phase difference of the interfering waves.

In the present paper it is shown theoretically and experimentally that the linear velocities of objects may be measured using a resonant ring interferometer with a low-coherence light source,[3] which was earlier proposed and demonstrated as an optical gyroscope.[4] Compared with a Sagnac interferometer, which was used to measure linear velocities in Refs. 1 and 2, this interferometer possesses higher sensitivity for the same ring dimensions as a result of the multipass interference in the ring resonator.

From the many possible systems of resonant ring interferometers with low-coherence light sources for the experiments, we selected the simplest system shown in Fig. 1. The fundamental elements of the system are a low-coherence light source $S$, a 3 dB coupler $C_1$, a ring resonator $R$, a weak coupling closed coupler $C_2$, and a photodetector $PD$. The object being measured $M$ is a return mirror positioned at the exit from the coupler $C_2$. The polarizer $P$ and the polarization controllers $PC_1$ and $PC_2$ can isolate the photodetector from the light reflected from the ring resonator. This can be accomplished as follows. If the polarization of the light is rotated through $\pm 90°$ as a result of single round trip in the ring resonator (the sign depends on the direction of the round trip), the Jones matrix of this resonator in the system (Fig. 1) is:

$$\hat{\mathbf{T}}^{\pm}=\left(R^{1/2}-(1-R)(1-R^{1/2}\exp(i\varphi^{\pm}))\,\frac{R\exp(i\varphi^{\pm})}{1+R\exp(i2\varphi^{\pm})}\right)\times\begin{vmatrix}1 & 0\\ 0 & 1\end{vmatrix}+\frac{R^{1/2}(1-R)\exp(i\varphi^{\pm})}{1+R\exp(i2\varphi^{\pm})}\begin{vmatrix}1 & \mp 1\\ \pm 1 & 1\end{vmatrix}, \qquad (1)$$

where ''+'' and ''−'' correspond to a resonator round trip in the clockwise and counterclockwise direction, $R$ is the reflection coefficient (the fraction of noncoupled power) of the coupler $C_2$ (in a high-Q resonator $1-R\ll 1$), and $\varphi$ is the phase shift of the light wave per round trip. The coefficient of the isotropic matrix contains the term $R^{1/2}$, which carries no information on the phase shifts in the resonator. In order to eliminate background illumination associated with this term, the second of the two terms (1) should be isolated. This may be achieved by making the section between the polarizer $P$ and the coupler $C_2$ isotropic and the section between the coupler $C_2$ and the return mirror $M$ equivalent to a quarter-wave plate turned through 45° relative to the polarizer $P$. In this case, the polarizer only passes the wave corresponding to the second term (1) to the photodetector $PD$. Thus, in this polarization scheme the resonator only transmits light at its resonant frequencies, as if it were operating in the transmission mode (Fig. 2). The required anisotropy in the resonator and between the polarizer and the object is created by the polarization couplers $PC_1$ and $PC_2$.

The linear velocity of the object $M$ may be measured as follows. The light source $S$ emits a broad spectrum whose width includes many resonances of the ring resonator. On the path from the source to the object, the resonator cuts bands from this spectrum, corresponding to its resonance lines. As a result, the spectrum of the radiation incident on the object is a set of lines whose central frequencies are equal to the natural frequencies of the ring resonator. If the object $M$ moves relative to the resonator, the lines in the spectrum of the light reflected from the object are shifted relative to the lines of the incident light, i.e., relative to the resonant frequencies of the resonator. In order to reach the photodetector

 © 1999 American Institute of Physics

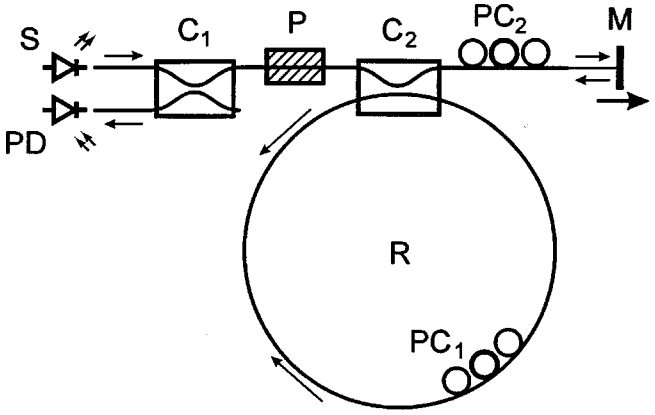


FIG. 1. Schematic of resonant ring interferometer with low-coherence light source: $S$ — light source, $C_1$ — 3 dB fiber coupler, $P$ — polarizer, $C_2$ — fiber coupler with weak coupling, $R$ — ring resonator, $PC_1$ and $PC_2$ polarization controllers, $M$ — object being measured (moving mirror), and $PD$ — photodetector.

$PD$, the reflected light must again pass through the resonator, although the shifted lines of the reflected light are transmitted less efficiently by the resonator the larger their frequency shift. Consequently, the optical power reaching the photodetector depends on the Doppler frequency shift of the light reflected from the object, i.e., on the velocity of the object relative to the interferometer.

The phase nonreciprocity in the ring resonator, which is responsible for different resonant frequencies for the clockwise and counterclockwise directions, influences the interferometer output power in exactly the same way as the Doppler effect.[3,4] Thus, the phase nonreciprocity in the ring resonator rather than the frequency of the reflected light can be modulated to make modulation measurements of the linear velocity. This can be accomplished by using phase nonreciprocity modulators comprising asymmetrically positioned reciprocal phase modulators used in Sagnac fiber-optic gyroscopes.[6] Modulators based on the Faraday and Kerr magneto-optic effects and other nonreciprocal optical effects can also be used.

The expression for the optical power at the photodetector is given by:[3,4]

$$P_{\text{out}}(\nu,\phi)=\frac{\pi}{16F}\,\frac{\alpha P_0}{1+(2F/\pi)^2\sin^2\left(4\pi\dfrac{Ln}{c}\dfrac{\nu}{\lambda}-\phi\right)}, \quad (2)$$

where

$$F=\frac{\pi\sqrt{R}}{1-R} \quad (3)$$

is the definition of the ring resonator, $\alpha$ is the reflection coefficient of the object, $P_0$ is the light source power, $L$ is the length of the ring resonator, $n$ is its refractive index, $v$ is the velocity of the object, $\nu_s$ is the central frequency of the source, and $\phi$ is the phase nonreciprocity in the resonator.

For measurements using the modulation method the limiting sensitivity of the interferometer in the 1 Hz band at the modulation frequency $f_m=c/(2nL)$ (assuming that $F\gg 1$) is:

$$v_{\min}\approx\frac{3c^2}{2\pi Ln\nu_s}\left(\sqrt{\frac{h\nu_s}{\alpha P_0 F}}+\frac{(2/\pi)^{1/4}}{F^{5/2}\sqrt{\Delta\nu_s}}\right), \quad (5)$$

where $\Delta\nu_s$ is the spectral width of the light source. The first term in Eq. (5) corresponds to the shot noise while the second corresponds to the beat noise of the spectral components of the radiation at the photodetector.[5] For the easily attainable interferometer parameters $L=100$ m, $n=1.5$, $F=50$, $\alpha=1$, $P_0=500$ mW, $\nu_s=2\times10^{14}$ Hz (1.5 $\mu$m wavelength), and $\Delta\nu_s=10^{13}$ Hz (coherence length 30 $\mu$m) the lowest detectable velocity of the object is $5\times10^{-7}$ mm/s, which corresponds to a Doppler frequency shift of $7\times10^{-4}$ Hz. This is approximately $\sqrt{F}$ times better than a Sagnac interferometer with the same light source and the same length of sensitive ring system.[2] This improvement in sensitivity was achieved by using multipass interference in the ring resonator. These estimates show that for very moderate parameters of the light source and the resonator, the interferometer can measure velocities corresponding to Doppler frequency shifts of the order of thousandths of a hertz. Measurements of such slow displacements by methods based on detecting the difference frequency would present considerable difficulties.

The experimental apparatus to measure the linear velocity is shown schematically in Fig. 3. For the experiment we used an all-fiber resonant interferometer consisting of an isotropic single-mode fiber with a low-Q ring resonator and a low-coherence superluminescence light source. The wavelength of the source $SLD$ was 0.83 $\mu$m, the power was around 100 $\mu$W, and the coherence length 50 $\mu$m. The length of the ring resonator was 500 m. The resonator was closed by a polished fiber coupler $C_2$ having a division coefficient of 1:10. With this division coefficient, the resonator

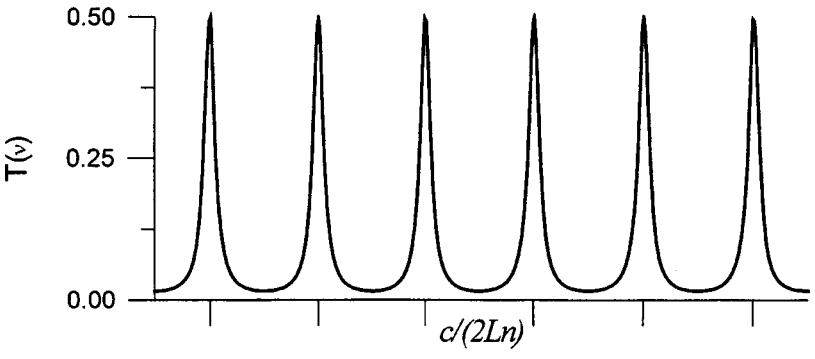


FIG. 2. Transmission spectrum of ring resonator in resonant ring interferometer in a polarizing system where light reflected from the ring resonator is eliminated.

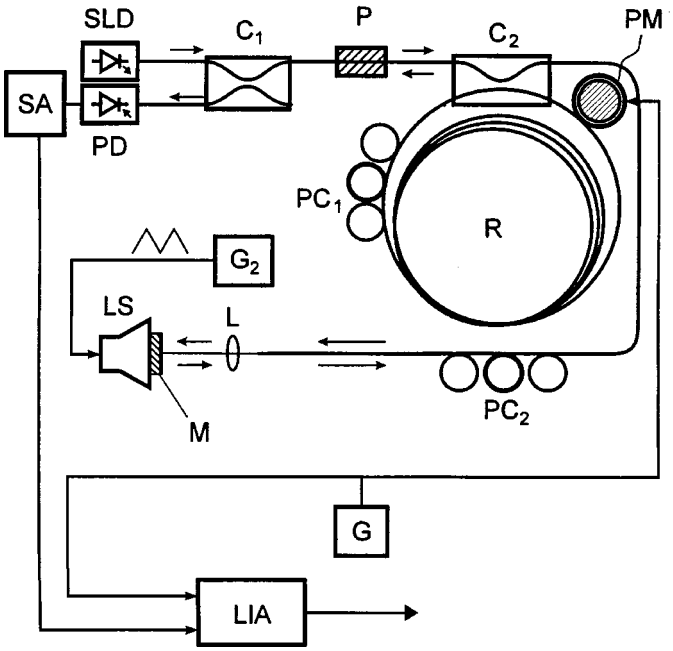


FIG. 3. Schematic of apparatus to measure linear velocity: *SLD* — superluminescence diode, $C_1$ — 3 dB fiber coupler, *P* — polarizer, $C_2$ — fiber coupler with weak coupling, *R* — ring resonator, *PM* — phase nonreciprocity modulator, *G* — modulating voltage generator (200 kHz), $PC_1$ and $PC_2$ — polarization controllers, *M* — return mirror, *LS* — loud speaker, $G_2$ — sawtooth voltage generator, *PD* — photodiode, *SA* — selective amplifier at 200 kHz, and *LIA* — lock-in amplifier.

definition was determined by the intrinsic losses in the fiber (2.2 dB/km) and did not exceed 1.8 so that the resonator operated in an almost single-pass regime. The ring resonator was equipped with a phase nonreciprocity modulator which consisted of a piezo-optic fiber phase modulator *PM* asymmetrically positioned relative to the closing coupler $C_2$. The modulation frequency was close to the optimum $c/(2Ln) = 200$ kHz. The object being measured was a return mirror *M* attached to a loudspeaker *LS*. The photodetector was a silicon photodiode *PD* whose load voltage was amplified by a selective amplifier *SA* tuned to the modulation frequency 200 kHz. Note that the interferometer parameters were far from optimal, since the aim of the experiment was merely to demonstrate the possibility of this new method of measurement.

The linear velocity of the return mirror was measured from the amplitude of the first harmonic of the modulation frequency 200 kHz isolated by a lock-in amplifier *LIA*. The time constant of this lock-in amplifier was around 0.05 s. A periodic sawtooth voltage from the generator $G_2$ was fed to the loudspeaker. The frequency and amplitude of this voltage were taken to be sufficiently low to ensure strict proportionality between the voltage at the loudspeaker and the mirror coordinate. Figure 4 shows a trace of the interferometer output signal (upper trace) for sawtooth modulation of the position of the return mirror (lower trace). When the oscillation amplitude was 0.4 mm and the period 1.25 s, the mirror velocity was $\pm 1.3$ mm/s, which corresponds to a Doppler frequency shift of 3.25 kHz. It can be seen that the interferometer output signal is proportional to the mirror velocity. The interferometer sensitivity was determined by the photodetector noise and was approximately $0.1\ \text{mm}/(\text{s}\cdot\text{Hz}^{1/2})$.

This theoretical and experimental investigation of a resonant ring interferometer with a low-coherence light source has shown that this interferometer may be used to measure the linear velocities of objects. The main advantage of the proposed interferometer over conventional optical velocity meters based on mixing the initial and reflected waves and measuring the difference frequency is that it is possible to measure very low velocities, corresponding to subhertz Doppler frequency shifts. Another attractive feature of low-coherence resonant interferometers is that they can be constructed using the well-developed technology and basic elements of Sagnac fiber-optic gyroscopes. Resonant ring interferometers with low-coherence sources can be used to measure microdisplacements with characteristic times of the order of or less than the period of the difference frequency, growth processes, and also processes involving no mechanical motion but which cause a frequency shift when light is reflected, for example, changes in refractive index.

The authors are grateful to I. A. Andronova for interest in this work and to R. V. Kuranov for assistance with the experiment.

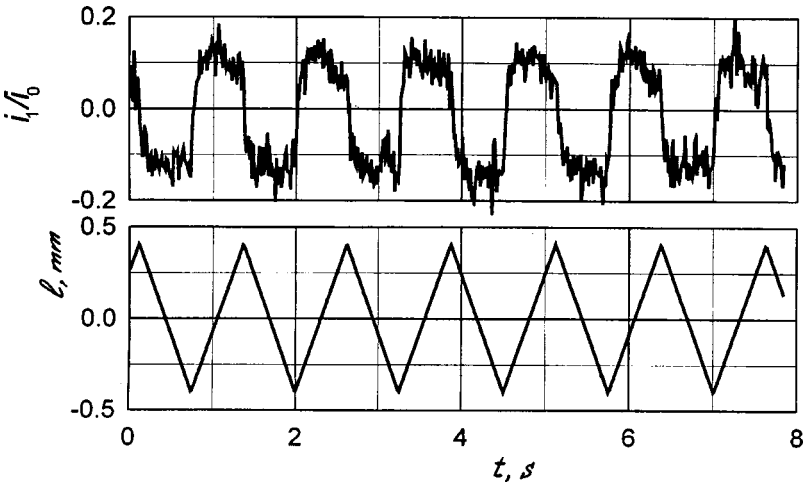


FIG. 4. Interferometer output signal with sawtooth modulation of the position of the return mirror. Upper trace — output signal from lock-in amplifier, $i_1$ — amplitude of the first harmonic of the photocurrent, $i_0$ — constant component of photocurrent. Lower trace — position of return mirror ($l$, mm). Time constant of lock-in amplifier — 0.05 s.

[1] A. Tselikov and J. Blake, Appl. Opt. **37**, 6690 (1998).
[2] T. A. Carolan, R. L. Reuben *et al.*, Appl. Opt. **36**, 380 (1997).
[3] M. A. Novikov and V. V. Ivanov, Pis'ma Zh. Tekh. Fiz. **24**(17), 24 (1998) [ Tech. Phys. Lett. **24**, 674 (1998)].
[4] V. V. Ivanov, M. A. Novikov, and V. M. Gelikonov, Kvantovaya Élektron. (Moscow), in press.
[5] S. M. Rytov, *Introduction to Statistical Radio Physics*, Part. I [in Russian], Nauka, Moscow (1976), pp. 393–395.
[6] R. A. Bergh, H. C. Lefevre, and H. J. Shaw, J. Lightwave Technol. **LT-2**, 91 (1984).

Translated by R. M. Durham

# Field evaporation of lanthanum hexaboride and estimate of the stability of forming clusters

I. Bustani, R. Byunker, G. Khirsh,*) V. N. Gurin, M. A. Korsukova, M. V. Loginov, and V. N. Shrednik

*Bergische Universität-Gesamthochschule, Wuppertal, Germany*
*A. F. Ioffe Physicotechnical Institute, Russian Academy of Sciences, St. Petersburg*
(Submitted July 28, 1999)
Pis'ma Zh. Tekh. Fiz. **25**, 43–49 (December 12, 1999)

In addition to boron and lanthanum ions, mass spectra of the field evaporation of lanthanum hexaboride ($LaB_6$) reveal various ionized clusters of the type $LaB_n^{+m}$, where $n=1,2\ldots6$, $m=1,2,3,4$. The probability of observing specific clusters in an ion flux is compared with the energy stability of the free clusters calculated theoretically. Clusters possessing low stability in the free state or completely unstable clusters tending to dissociate leave the surface more readily. © *1999 American Institute of Physics.* [S1063-7850(99)00712-0]

## 1. INTRODUCTION

An atomic probe[1,2] was used to investigate field evaporation[1] of lanthanum hexaboride ($LaB_6$) single crystals. Thin acicular $(LaB)_6$ crystals were grown by a flux method.[3] Detailed evaporation mass spectra were obtained at room temperature ($T$) at various electric field strengths ($F$) and after various sample pretreatments. Numerous peaks in these spectra (Fig. 1) corresponded to lanthanum ($La^{+++}$, $La^{++}$) and boron ions ($B^{++}$, $B_2^{+++}$, and so on), and also more complex cluster ions (fragments) having the composition $LaB_n$ ($n=1,2,3,4,5,6$). The ion charge was mostly $+2$ or $+3$ with ions having charges of $+1$ or $+4$ appearing less frequently.

The experimental spectra could be used to estimate the relative content of a particular $LaB_n^{+m}$ fragment in the ion flux.

This content is determined theoretically by the values of the parameters $F$ and $T$, and also by the energy required to detach this fragment from the solid and ionize it to a specific charge.[1] This should also be influenced by the energy determining the chemical stability of a particular free fragment cluster. The first two types of energy (the heat of evaporation and the ionization energy) are only known for simple, usually atomic (nonmolecular) ions. For multicomponent materials these values are generally unknown. The stability of free clusters, including charged ones (which is related to the energy expended to form them from isolated atoms) can be estimated theoretically. It was interesting to compare the experimental probability of particular clusters appearing in field evaporation products with the stability of these clusters calculated theoretically. Such a comparison for $LaB_n^{+m}$ clusters is made for the first time in the present study.

## 2. CALCULATIONS OF CLUSTER STABILITY

The total energy of $La_n^{+m}$ ($n=1\ldots6$, $m=0\ldots4$) clusters was calculated using exact *ab initio* quantum-chemical methods in the molecular orbital approximation taking into account the Hartree–Fock bounded self-consistent field and configurational interaction. We used a standard $(9s3p/4s2p)$ Dunning basis,[4] supplemented with allowance for all the boron electrons using polarization $d$-functions with the exponential function $0.34a_0^{-2}$. In addition to the three valence electrons from the $5d^16s^2$ shells of lanthanum, the calculations also took account of electrons from the $5s^2$ and $5p^6$ shells which are usually included in the atomic core, which allowed us to make reliable calculations of the binding energy.

For the internal electron shells of the lanthanum atom we used relativistic, compact effective potentials. The corresponding basis for the eleven active electrons of lanthanum together with the relativistic compact effective potentials of the core electrons are given in Ref. 5.

Configurational interaction was analyzed in terms of the geometric forms obtained when searching for the local minima on the potential energy surface using the Hartree–Fock ground-state energy.

All the calculations were made using the GAMESS-UK program package[6] on the SGI-Challenge computer at the Computing Center, Wuppertal University.

The stability of the clusters can be expressed in terms of the binding energy, which is the difference between the cluster energy and the energies of its constituent individual atoms (or ions). For neutral clusters the binding energy $E_b$ is determined using the formula:

$$E_b(LaB_n)=nE(B)+E(La)-E(LaB_n), \tag{1}$$

and for charged clusters, allowing for the most convenient dissociation channel, it is determined by

$$E_b(LaB_n^{+m})=(n-m+1)E(B)+(m-1)E(B)^+ +E(La)^+-E(LaB_n^{+m}). \tag{2}$$

In order to find the most stable systems, we analyzed various configurations of the $LaB_n^{+m}$ isomer.

 © 1999 American Institute of Physics

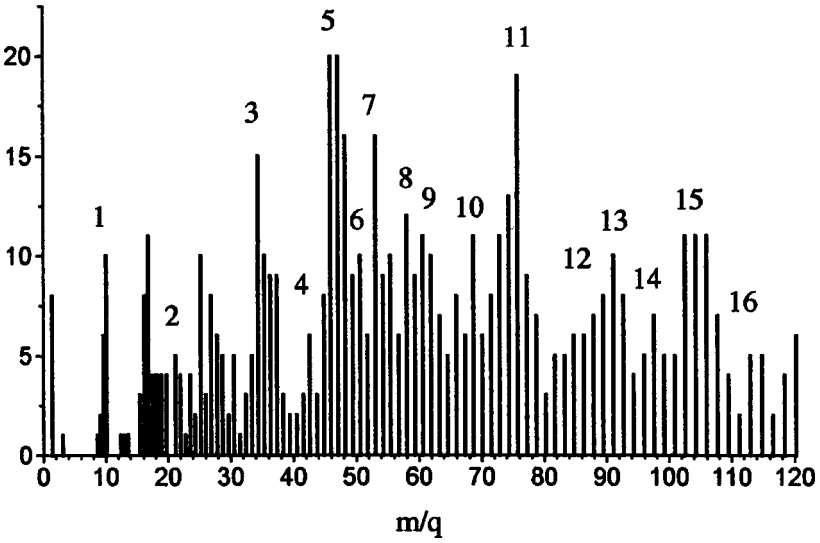


FIG. 1. Field evaporation spectrum (mass spectrum) of $LaB_6$ at room temperature. The number of recorded ions is plotted on the abscissa. The base voltage is $V_b = 8$ kV and the pulsed voltage $V_p = 4$ kV. The number of resultative pulses is $n = 300$, the total number of supplied pulses is $N = 534$, and $m/q$ is the ratio of the ion mass to its charge: *1* — $B^+$, $B_2^{++}$; *2* — $B_2^+$, $B_4^{++}$; *3* — $La^{4+}$; *4* — $LaB_3^{4+}$; *5* — $La^{+++}$; *6* — $LaB_6^{4+}$; *7* — $LaB_2^{+++}$; *8* — $LaB_3^{+++}$; *9* — $LaB_4^{+++}$; *10* — $La^{++}$; *11* — $LaB^{++}$; *12* — $LaB_3^{++}$; *13* — $LaB_4^{++}$; *14* — $LaB_5^{++}$; *15* — $LaB_6^{++}$; and *16* — $La_2B_5^{+++}$.

The binding energies (in electronvolts) of stable lanthanum boride clusters obtained using self-consistent field theory are given in Table I. A dash in the table corresponds to a decaying cluster.

### 3. ANALYSIS OF EXPERIMENTAL DATA AND COMPARISON WITH THEORY

We obtained eight mass spectra of the field evaporation of $LaB_6$ and analyzed data from the five most comprehensive and reliable ones. These spectra were obtained using the following base $V_b$ and pulsed $V_p$ voltages $(V_b + V_p)$: $(4+3)$ kV (two spectra), $(5+4)$, $(8+4)$, and $(10+4.8)$ kV. The number of resultative pulses (those which generated the recorded ions) $n$ relative to the total number of pulses $N$ was: 300/339, 300/375, 300/358, 300/534, and 507/515, respectively. It can be seen from the ratios $n/N$ that the evaporation regime was intensive. This means that several (two or three rather than one) ions were very frequently recorded in one resultative pulse, i.e., the total number of ions exceeded, for example in the first four spectra, $n = 300$.

At the initial stages (in the chronologically first spectra) the highest-intensity peak was some boron peak ($B^{++}$, $B_2^{++}$ or $B_2^{+++}$). The next peak in terms of height and the predominant peak in the last two spectra was $La^{+++}$, which could be conveniently used to calibrate the spectrum. The nonstoichiometry in the total composition of the ion flux (the difference from its composition $LaB_6$) can be attributed to the predominant field evaporation of lanthanum which readily migrates over the surface of $LaB_6$ at room temperature. In addition to B and La ions and $LaB_n$ clusters, we also recorded ions of residual gases. One of the spectra used for the analysis is shown in Fig. 1.

The most frequently encountered, highest-intensity, and most reliably identified peaks of the $LaB_n$ clusters are given in Table II together with their rating, i.e., the sum of their amplitudes normalized to the largest $LaB_n^{+m}$ peak. We encountered $LaB_4^{+++}$ ions in four out of the five spectra studied while the other ions appeared in three out of five, giving peaks ranked first among the highest-intensity peaks.

A comparison between the experimental and theoretical data (Table I) reveals that the first four peaks of the $LaB_n^{+m}$ clusters correspond to the least stable $LaB_4^{+++}$ and $LaB^{++}$ ions having energies (see Table I) of 0.77 and 1.43 eV, respectively, or even to decaying unstable ($LaB_2^{+++}$, $LaB_3^{+++}$) formations. The only relatively stable cluster $LaB_4^{++}$, having the lowest rating, has a formation energy of 9.03 eV, which is by no means the highest of the set given in the table. Thus, the experimental field evaporation spectrum contains unstable or the least stable clusters. This observation can be explained in terms of the model of nonequilibrium field evaporation of a multicomponent material discussed, for example, when analyzing the field evaporation of high-temperature superconducting materials.[7–9]

The complex unit cell of $LaB_6$ rarely evaporates as a unit by the field mechanism. In reality, some part such as a lanthanum atom or one or several boron atoms may leave the cell in the form of an ion (ions). The rest of the cell evaporates in subsequent pulses either completely or in parts. If the fragment is internally unstable at the stage of separation from the surface and ionization, the chances of it detaching from the surface, being ionized, and escaping being trapped by the field, are higher for this type of cluster than for a stable one.

TABLE I.

| $m$ | 0 | 1 | 2 | 3 | 4 |
|---|---|---|---|---|---|
| $LaB^{+m}$ | 1.9 | 2.27 | 1.43 | – | – |
| $LaB_2^{+m}$ | 4.11 | 4.26 | 1.71 | – | – |
| $LaB_3^{+m}$ | 8.12 | 8.05 | 4.38 | – | – |
| $LaB_4^{+m}$ | 10.22 | 10.12 | 9.03 | 0.77 | – |
| $LaB_5^{+m}$ | 14.98 | 15.36 | 7.33 | 3.81 | – |
| $LaB_6^{+m}$ | 18.53 | 19.63 | 17.89 | 11.70 | – |

TABLE II. Most frequently occurring ions in order of decreasing ''rating''.

| Ion | $LaB_4^{+++}$ | $LaB_2^{+++}$ | $LaB_3^{+++}$ | $LaB^{++}$ | $LaB_4^{++}$ |
|---|---|---|---|---|---|
| Rating | 2.49 | 2.32 | 1.98 | 1.9 | 1.81 |

Quite clearly, as long as the fragment is tightly bound to the solid, its energy characteristic differ from those of a free cluster. However, at some intermediate time when there is an equal probability of the fragment becoming detached from the surface or remaining bound, a stable cluster most probably will not evaporate, whereas an unstable one, having an inherent tendency to break up, will separate from the surface and evaporate.

In order to ensure that the entire unstable fragment is recorded by the detector of the atomic probe as a unit, the fragment only needs to stay together during the short acceleration time $\tau_a$. As a result of the abrupt nonuniformity of the field near the tip, this time is less than $10^{-10}$ s, whereas the drift time $\tau_f$ is a few microseconds. Over the time $\tau_f$ the fragment can dissociate in principle, although its fragments will reach the detector simultaneously if the cluster lifetime was not less than $\tau_a$. If this lifetime is less than $\tau_a$, but comparable to it, ''strange'' masses may be recorded (since the ion mass may vary as it is accelerated) but this was not observed experimentally. A small mass shift could be detected for some ions by using a high-resolution mass spectrometer. Such experiments to estimate the lifetime of unstable clusters could form the subject of a separate study.

To sum up, experiments have shown that the most stable clusters have a lower probability of evaporating. Less stable and unstable clusters remain in the flux of evaporated ions because of the irreversibility of the processes taking place as they move away from the surface, and a buildup of charge as a result of so-called post-ionization. Note that neutral clusters and ions having charges of $+1$ and $+2$ (Table I) are stable and some of them are only converted to decaying forms as a result of subsequent ionization. Ions in clusters having a low formation energy (such as $LaB_4^{+++}$) have fewer possibilities for binding to the surface compared with more stable ones and are more likely to leave the surface as a result of field evaporation.

This work was supported by NATO Grant HTECH.L.G.972010.

*)Deceased.

[1] E. W. Müller and T. T. Tsong, *Field Ion Microscopy, Field Ionization, and Field Evaporation* (Pergamon Press, Oxford, 1973; Nauka, Moscow, 1980, 220 pp.).
[2] M. V. Loginov, O. G. Savel'ev, and V. N. Shrednik, Zh. Tekh. Fiz. **64**, 123 (1994) [Tech. Phys. **39**, 811 (1994)].
[3] M. M. Korsukova and V. N. Gurin, Usp. Khim. **61**, 3 (1987).
[4] T. H. Dunning Jr., J. Chem. Phys. **53**, 2823 (1970).
[5] W. J. Stevens, M. Krauss, H. Bassh, and P. G. Jasien, Can. J. Chem. Eng. **70**, 612 (1992).
[6] M. F. Guest and J. Kendrick, Daresbury Laboratory Report No.CCP1 / 86.
[7] V. N. Shrednik, in *Proceedings of the Sixth International Symposium on Discharges and Electrical Insulation in Vacuum, St. Petersburg, 1994*, p. 497.
[8] Yu. A. Vlasov, O. L. Golubev, E. L. Kontorovich, and V. N. Shrednik, Zh. Tekh. Fiz. **65**(1), 70 (1995) [Tech. Phys. **40**, 37 (1995)].
[9] O. L. Golubev, E. L. Kontorovich, O. G. Saveljev, V. N. Shrednik, and Yu. A. Vlasov, in *Abstracts of the 41st International Field Emission Symposium, Rouen, France, 1994*, p. GB-2.

Translated by R. M. Durham

# Surface waves at a moving plasma layer

I. L. Sheĭnman, A. D. Kanareĭkin, and E. A. Sizova

*St. Petersburg State Electrotechnical University*
(Submitted January 29, 1999)
Pis'ma Zh. Tekh. Fiz. **25**, 50–55 (December 12, 1999)

An analysis is made of stable and unstable surface electromagnetic waves at the boundary of a planar moving plasma layer. It is shown that unlike an isolated tangential velocity discontinuity, both slow and fast waves may exist inside the layer. The maximum spatial growth rate of the oscillations is achieved for directions of wave propagation other than the direction of motion of the layer. Symmetric and antisymmetric waves relative to the symmetry plane of the layer have different critical angles from which their growth evolves and the range of angles where the flux is stable is determined by the smaller of these. © *1999 American Institute of Physics.* [S1063-7850(99)00812-5]

The formation of a surface electromagnetic wave near the planar interface between two media is related to the existence of an imaginary part of the surface impedance[1] which corresponds to the case where one of the media has a complex refractive index.[2] In the absence of losses, this situation may arise if the permittivity is $\varepsilon<0$, i.e., for a plasma. When both fixed boundary media have positive permittivities, it is impossible for surface waves to be excited near the interface. The relativistic motion of one of these media leads to the possible excitation of an electromagnetic surface wave even at a tangential velocity discontinuity in a homogeneous medium with $\varepsilon>0$. In this case, a necessary condition for the existence of surface waves is the formation of anisotropy as a result of the appearance of a selected direction of motion of the medium.[4] Then, the waves can only propagate in directions forming angles greater than some critical angle with this direction of motion.

In addition to stable waves, growing surface electromagnetic waves also exist at a tangential velocity discontinuity, which leads to hydrodynamic instability of the relativistic plasma fluxes.[5] For a planar layer, relativistic motion relative to a stationary external medium promotes instability as a result of waves moving away from the interface being excited in the external dielectric medium (Čerenkov instability)[6] or surface waves if the stationary medium is a plasma.[7] However, the analysis reported in Refs. 6 and 7 only referred to the case of a collinear velocity and wave vector.

We shall consider a moving planar plasma layer of thickness $2h$ having the permittivity $\varepsilon_2$ and velocity $\mathbf{V}=\beta c$ in a stationary medium having the permittivity $\varepsilon_1$. In rectangular coordinates the velocity has the form $\boldsymbol{\beta}=(0,\beta_y,\beta_z)$, and the wave vector $\mathbf{k}_\perp$ is directed along the $z$ axis. From Maxwell's equations for a moving medium and boundary conditions we obtain:

$$(\varepsilon_2\kappa_1 S+\varepsilon_1\kappa_2)(\kappa_1 S^{-1}+\kappa_2) = (\varepsilon_2-1)(\varepsilon_1-1)\eta^2\gamma^2\beta_y^2, \tag{1}$$

where $\kappa_1^2=\eta^2-\varepsilon_1$, $\kappa_2^2=\eta^2-1-(\varepsilon_2-1)\gamma^2(1-\eta\beta_z)^2$, $\eta=k_z/k$, $k=\omega/c$, $k_z=|\mathbf{k}_\perp|$, and $\gamma=(1-\beta^2)^{-1/2}$.

Equation (1) is the dispersion equation for surface waves in a planar waveguide filled with a moving plasma, and describes waves having symmetric $[S=\coth(kh\kappa_2)$ [and antisymmetric $[S=\tanh(kh\kappa_2)]$ components of the field $E_z$ relative to the $yz$ plane. For a tangential velocity discontinuity in a homogeneous medium i.e., $\varepsilon_1=\varepsilon_2$, the equations (1) for the symmetric and antisymmetric waves are the same. For

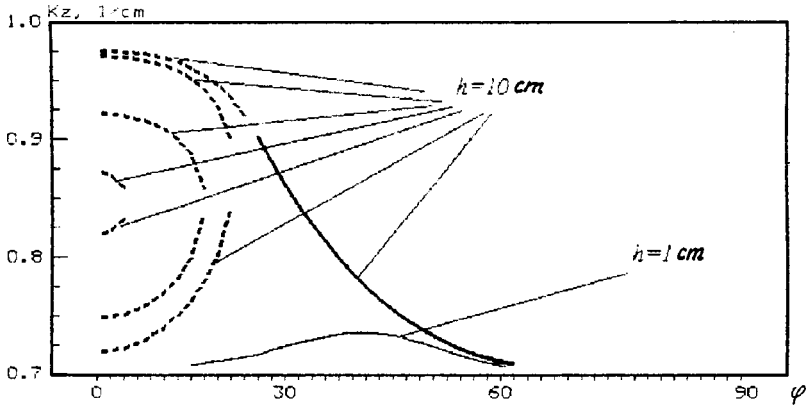


FIG. 1. Propagation constant $k_z$ as a function of the angle $\varphi$ between $\mathbf{k}_\perp$ and $\mathbf{V}$ for a planar moving layer for $\varepsilon_1=\varepsilon_2=0.5$, $k=\omega/c=1\ \mathrm{cm}^{-1}$, $\gamma=3$, $\beta=0.941$: ▬ $=\kappa_2^2>0$ (slow waves), ▪▪▪ $=\kappa_2^2<0$ (fast waves), $h=10$ cm; —— $=\kappa_2^2>0$ (slow waves), $h=1$ cm.

 © 1999 American Institute of Physics

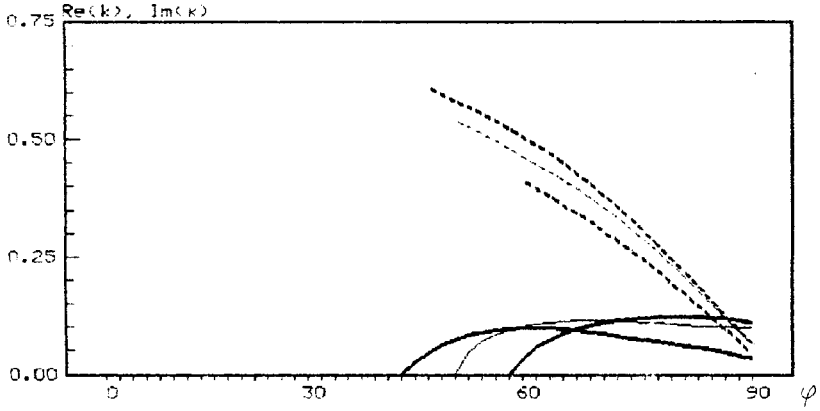


FIG. 2. Dependences of the real and imaginary parts of $k=\omega/c$ on the angle $\varphi$ between $\mathbf{k}_\perp$ and $\mathbf{V}$ for waves at a tangential velocity discontinuity and at a moving plasma layer for $\beta=0.999$ ($\gamma=22.4$), $k_z=1$ cm, $n_1=n_2=1.4\times10^{11}$ cm, $h=1$ cm: ▬ = Im($k$), ■■■ = Re($k$), planar moving layer; —— = Im($k$), - - - = Re($k$), tangential velocity discontinuity.

$h\to+\infty$ the relative influence of the boundaries becomes negligible and Eq. (1) yields the dispersion equation for surface waves at the planar interface between two media moving relative to each other:[3]

$$(\varepsilon_2\kappa_1+\varepsilon_1\kappa_2)(\kappa_1+\kappa_2)=(\varepsilon_2-1)(\varepsilon_1-1)\,\eta^2\gamma^2\beta_y^2. \quad (2)$$

Figure 1 gives the propagation constant $k_z$ as a function of the angle $\varphi$ between $\mathbf{k}_\perp$ and $\mathbf{V}$ for surface waves at the moving layer ($k=1$ cm, $\beta=0.941$, $\gamma=2.96$, $\varepsilon_1=\varepsilon_2=0.5$). Surface waves whose amplitude decays exponentially with increasing distance from the boundaries outside the layer may have two types inside the layer: slow surface waves for $\kappa_2^2>0$ and fast volume waves for $\kappa_2^2<0$. Unlike an isolated tangential velocity discontinuity where the surface waves could not propagate at angles smaller than some critical angle $\varphi_k$ between $\mathbf{k}_\perp$ and $\mathbf{V}$ (Ref. 3), for surface waves at a layer the critical angle $\varphi_k$ corresponds to the transition from fast to slow waves. The largest critical angle is achieved for $S\approx\sqrt{\varepsilon_1\varepsilon_2}$, which for $\varepsilon_1=\varepsilon_2$ gives $h\to+\infty$. A decrease in the layer thickness leads to a reduction in the critical angle and for small $h$ no fast volume waves appear.

In addition to stable solutions, the equations (1) may also have solutions which increase in time or space and lead to the appearance of absolute and convective instabilities of the plasma layer. Analytic expressions for a plasma external medium may be obtained in limiting cases of high and low frequencies by substituting expressions for the permittivity of a stationary and moving plasma into Eq. (2). For real $k$ we then have

$$\eta=\beta_z^{-1}[1\pm ik_{p2}k^{-1}\gamma^{-1}((k^2+k_{p1}^2\beta_y^2)/(k_{p1}^2-2k^2))^{1/2}], \quad (3)$$

where $k\ll k_{p1}$, $k\ll k_{p2}$ and for $k\gg k_{p1}$, $k\gg k_{p2}$.

When $k_z\ll k_{p1}$, $k_z\ll k_{p2}$ and $k\ll k_{p1}$, $k\ll k_{p2}$, the solution may be expressed in the form

$$\eta=[\beta_z(1+\nu)\pm i(\nu\beta^2(1+\nu)(1-\beta_z^2+\nu(1-\beta^2)))^{1/2}]\times(\beta_z^2+\nu\beta^2)^{-1}, \quad (4)$$

where $\nu=k_{p2}/k_{p1}$, $k_{p1}^2=4\pi e^2n_1/mc^2$, $k_{p2}^2=4\pi e^2n_2/m\gamma c^2$, $n_1$ and $n_2$ are the electron concentrations outside and inside the layer, $e$ is the charge, and $m$ is the electron mass.

Note that in these cases, the maximum spatial growth rate of the oscillations is reached for $\beta_z\to0$, $\beta_y=\beta$. In this case, we obtain from Eq. (4) $\mathrm{Im}(\eta)=(1+\nu\gamma^{-2})\times(1+\nu)\gamma/\beta^2$.

By finding complex solutions of Eq. (1) in the form of frequency perturbations of the wave whose phase velocity is equal to the velocity of the layer in its direction of propagation $k=k_0+k_*$, $|k_*|\ll k_0$, $k_0=\beta_zk_z$; $\beta_{\mathrm{ph}}=(k/k_z)\approx(k_0/k_z)=\beta_z$, we obtain

$$k_*=\frac{k_{p2}}{\gamma}\left(\frac{\kappa_1^2+\kappa_1\kappa_2S-(\varepsilon_1-1)\gamma^2\beta_y^2/\beta_z^2}{(\kappa_1S+\varepsilon_1\kappa_2)(\kappa_1S^{-1}+\kappa_2)}\right)^{1/2}, \quad (5)$$

where $\kappa_1^2=(1-\varepsilon_1\beta_z^2)/\beta_z^2$, $\kappa_2^2=(1-\beta_z^2)/\beta_z^2+k_{p2}^2/k_0^2$. Thus, for resonant wave instability the constraints $\varepsilon_1<0$ or $\varepsilon_1>1$ must be satisfied, i.e., the external medium must be dielectric.

Figure 2 gives the real and imaginary parts of $k$ obtained by means of a numerical solution of Eqs. (1) and (2) for a fixed real propagation constant $k_z$ as a function of the angle $\varphi$ between $\mathbf{k}_\perp$ and $\mathbf{V}$ for surface waves at the tangential velocity discontinuity between two media and a moving plasma layer for $k_z=1\ \mathrm{cm}^{-1}$, $n_1=n_2=1.4\times10^{11}\ \mathrm{cm}^{-1}$, $\beta=0.999$, $\gamma=22.4$, and $h=1$ cm. In the ultrarelativistic case the tangential velocity discontinuity is stable with respect to surface waves whose wave vector is parallel to the velocity of the medium but unstable with respect to waves propagating at angles greater than some critical angle $\varphi$. For the plasma layer the symmetric and antisymmetric waves relative to the $yz$ plane have different critical angles from which they begin to grow. The range of angles where the flux is stable is determined by the smaller of these.

This type of surface waves may be used in relativistic plasma microwave electronics devices to generate electromagnetic waves in directions other than the direction of motion of the plasma layer.

[1] G. T. Markov and A. F. Chaplin, *Excitation of Electromagnetic Waves* [in Russian], Énergiya, Moscow (1967), 376 pp.
[2] S. Solimeno, B. Crosignani, and P. DiPorto, *Guiding, Diffraction, and Confinement of Optical Radiation* (Academic Press, Orlando, 1986; Mir, Moscow, 1989, 664 pp.).

[3] K. A. Barsukov and A. D. Kanareĭkin, Zh. Tekh. Fiz. **55**, 1847 (1985) [Sov. Phys. Tech. Phys. **30**, 1082 (1985)].
[4] A. D. Kanareĭkin and I. L. Sheĭnman, Pis'ma Zh. Tekh. Fiz. **22**(2), 61 (1996) [Tech. Phys. Lett. **22**, 74 (1996)].
[5] A. D. Kanareĭkin and I. L. Sheĭnman, Pis'ma Zh. Tekh. Fiz. **23**(5), 76 (1997) [Tech. Phys. Lett. **23**, 201 (1997)].
[6] A. N. Kondratenko and V. M. Kuklin, *Principles of Plasma Electronics* [in Russian], Énergoatomizdat, Moscow (1988), 320 pp.
[7] V. G. Gavrilenko, G. A. Lupanov, and E. S. Stepanov, Izv. Vyssh. Uchebn. Zaved., Radiofiz. **13**, 700 (1970).

Translated by R. M. Durham

# Exact solution of the problem of an equilibrium configuration of a two-dimensional charged liquid-metal droplet

N. M. Zubarev

*Institute of Electrophysics, Urals Branch of the Russian Academy of Sciences, Ekaterinburg*
(Submitted July 13, 1999)
Pis'ma Zh. Tekh. Fiz. **25**, 55–60 (December 12, 1999)

A conformal mapping method was used to obtain exact solutions of the problem of the equilibrium shape of a charged two-dimensional liquid-metal droplet. It was found that when the perturbation amplitudes reach certain critical values, the regions occupied by the liquid ceased to be singly connected, which corresponds to the breakup of the droplet into parts. © *1999 American Institute of Physics.* [S1063-7850(99)00912-X]

The problem of the equilibrium configuration of a charged liquid-metal droplet plays an important role in understanding the conditions for the strict excitation of instability leading to its breakup.[1,2] In view of the nonlinearity of the corresponding equations, these have been investigated analytically either using the approximation of small surface perturbations or nonself-consistently (see, for example, Refs. 3 and 4 and the literature cited). In the present paper it is shown that for the special case of a two-dimensional droplet when all the quantities only depend on the pair of independent variables $x$ and $y$, conformal mapping can be used to find a wide range of exact solutions to this problem (from the mathematical point of view a very similar approach was used to solve the problem of the capillary wave profile at the surface of an ideal liquid[5]).

Thus, we shall assume that a charged conducting liquid having a free surface $S$ occupies a bounded, singly connected region in the plane $\{x,y\}$ (in 3D space the conductor occupies a volume bounded by a right cylindrical surface). The distribution of the electric field potential $\varphi$ (the field strength is given by $\mathbf{E}=-\nabla\varphi$) in the absence of space charge is described by the Laplace equation:

$$\varphi_{xx}+\varphi_{yy}=0,$$

This must be analyzed in conjunction with the condition for an equipotential conductor surface $\varphi|_S=0$, and also the condition that at infinity the field of the charged conductor will be the same as the field generated by a point charge:

$$\varphi\to-2q\ln x, \quad E=|\mathbf{E}|\to 2q/x, \quad r\to\infty, \tag{1}$$

where $r=\sqrt{x^2+y^2}$ and $q$ is the electric charge of the conductor.

The equilibrium relief of the liquid metal boundary is determined by the balance condition for the forces acting on the surface:[2]

$$p+\frac{E^2}{8\pi}\bigg|_S+\frac{\alpha}{R}=0, \tag{2}$$

where $\alpha$ is the surface tension, $p$ is the difference between the liquid pressure and the external pressure, and $R$ is the radius of curvature of the surface. Note that the curvature of an equipotential surface $S$ may be expressed in terms of $E$ and $\varphi$ as follows: $R^{-1}=-(\partial E/\partial\varphi)|_S$.

For convenience we now convert to the dimensionless quantities:

$$\mathbf{E}\to 4\pi\alpha q^{-1}\mathbf{E}, \quad \mathbf{r}\to q^2(2\pi\alpha)^{-1}\mathbf{r},$$

$$\varphi\to 2q\varphi, \quad p\to 2\pi\alpha^2 q^{-2}p.$$

We then introduce the auxiliary function $\psi$ for which $\mathbf{E}=\{\partial\psi/\partial y,-\partial\psi/\partial x\}$. The complex expression $w=\varphi-i\psi$ (the so-called complex potential) is an analytic function of the complex variable $z=x+iy$. Then

$$f-i\theta\equiv\ln(-dw/dz)=\ln E-i\arctan(\varphi_y/\varphi_x) \tag{3}$$

will also be an analytic function, this being the analog of the Zhukovskii function in the theory of the plane potential flow of an incompressible liquid.

For the following analysis it is convenient to use a system of coordinates where $\varphi$ and $\psi$ will play the role of independent variables. As a result of the analytic nature of Eq. (3), the function $f$ will satisfy the Laplace equation in the new variables

$$f_{\varphi\varphi}+f_{\psi\psi}=0 \tag{4}$$

with the condition at the conductor boundary obtained from condition (2):

$$\partial f/\partial\varphi=pe^{-f}+e^f, \quad \varphi=0, \tag{5}$$

and also the condition at infinity:

$$f\to\varphi, \quad \varphi\to-\infty, \tag{6}$$

obtained from Eq. (1) by eliminating the spatial variable $r$. Bearing in mind that in the limit $|z|\to\infty$ for the complex potential[2] we have $w\to-\ln z$ and hence the closed surface corresponds to a change in $\psi$ by $2\pi$, we add the condition for periodicity of $f$ in terms of the variable $\psi$:

$$f(\varphi,\psi)=f(\varphi,\psi+2\pi). \tag{7}$$

Thus, the problem of finding the steady-state profile of a charged 2D liquid-metal droplet reduces to an analysis of the boundary-value problem (4)–(7) on the half-plane $\varphi\leqslant 0$.

 © 1999 American Institute of Physics

We shall seek a solution of the problem (4)–(7) in the form

$$f(\varphi,\psi)=C+\varphi+\ln\left(\frac{Z_\varphi-Z+Y}{Z_\varphi+Z-Y}\right), \tag{8}$$

where $C$ is a constant, $Y$ is an unknown function of the variable $\psi$, and $Z$ is an unknown function of the variable $\varphi$. Substituting expression (8) into the equations being studied, we observe that the following relationships should be satisfied:

$$Z(\varphi)=\sinh(k\varphi+\ln d),$$

$$Y(\psi)=\sqrt{k^2-1}\cos(k\psi),$$

$$C=\ln(l/2-1/2),$$

where $k=2,3,4\ldots$ is an integer parameter which defines the number of branches of the corresponding curve in terms of the coordinates $x$ and $y$, $l=(1-4p)^{1/2}$ (the inequality $1<l<k$ is satisfied), and finally $d=(k-l)^{1/2}(k+l)^{-1/2}$.

Substituting our expressions for $Z$ and $Y$ into Eq. (8) and bearing in mind that $E=\exp f$, we obtain for the absolute value of the electric field intensity at the surface of the conductor:

$$E|_{\varphi=0}=\frac{1+a^2d^2+2ad\cos(k\psi)}{a^2+d^2-2ad\cos(k\psi)}\exp C, \tag{9}$$

where we have introduced the notation $a=(k-1)^{1/2}\times(k+1)^{-1/2}$.

We also need the dependence of the function $\theta$, which defines the slope of the electric field intensity to the direction of the $x$ axis, on the variable $\psi$ at the liquid metal interface. Using the Cauchy–Riemann condition $\partial\theta/\partial\psi=\partial f/\partial\varphi$, we obtain from Eq. (5):

$$\theta\Big|_{\varphi=0}=\frac{\pi}{2}+\int_0^\psi (E+p/E)\Big|_{\varphi=0}\,d\psi. \tag{10}$$

We can now construct equilibrium profiles of the free surface of a liquid metal in terms of the coordinates $x$ and $y$. Considering formula (3) to be an ordinary differential equation for the unknown function $z$, we obtain by integrating: $z=-\int\exp(-f+i\theta)dw$. Bearing in mind that at the interface $w=-i\psi$, we find that the unknown surfaces are defined parametrically as follows:

$$y=y_0+\int_0^\psi \frac{\cos(\theta|_{\varphi=0})}{E|_{\varphi=0}}d\psi,$$

$$x=x_0-\int_0^\psi \frac{\sin(\theta|_{\varphi=0})}{E|_{\varphi=0}}d\psi, \tag{11}$$

where the parameter $\psi$ covers the range $0\leqslant\psi<2\pi$, and formulas (9) and (10) should be used in the expressions in the integrand. The constants $x_0$ and $y_0$ can be conveniently selected so that the geometric center of the curve coincides with the origin.

Figures 1 and 2 show characteristic steady-state configurations of a liquid metal for $k=2$ and $k=3$, respectively, determined by formulas (9)–(11). It can be seen that as the parameter $l$ decreases, the amplitudes of the surface perturbations increase (cylindrical surfaces corresponding to the limits $l\to k$ are considered to be unperturbed surfaces) and for certain $k$-dependent critical values of the parameter $l$, the region occupied by the liquid ceases to be singly connected and isolated liquid metal droplets form.

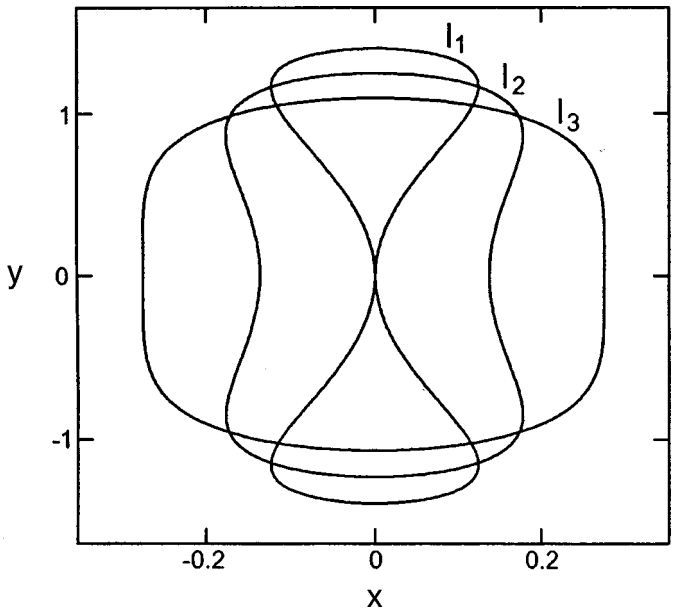


FIG. 1. Equilibrium configurations of charged 2D liquid-metal droplet for $k=2$ for three values of the parameter $l$ ($l_1=1.86$, $l_2=1.90$, and $l_3=1.94$).

The author is grateful to E. A. Kuznetsov for stimulating discussions and also to A. M. Iskol'dskiĭ and N. B. Volkov for their interest in this work.

This work was supported financially by the RFBR, Project No. 97-02-16177.

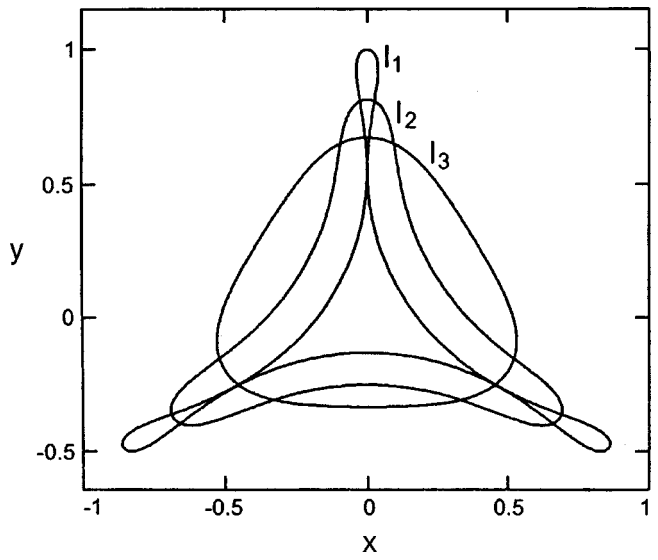


FIG. 2. Equilibrium configurations of charged 2D liquid-metal droplet for $k=3$ ($l_1=2.53$, $l_2=2.75$, and $l_3=2.97$).

[1] J. W. Strutt (Lord Rayleigh), Philos. Mag. **14**, 184 (1882).
[2] L. D. Landau and E. M. Lifshitz, *Electrodynamics of Continuous Media*, (Pergamon Press, Oxford, 1984; Nauka, Moscow, 1982).
[3] S. I. Shchukin and A. I. Grigor'ev, Zh. Tekh. Fiz. **68**(11), 48 (1998) [Tech. Phys. **43**, 1314 (1998)].
[4] S. O. Shiryaeva, A. I. Grigor'ev, and I. D. Grigor'eva, Zh. Tekh. Fiz. **65**(9), 39 (1995) [Tech. Phys. **40**, 885 (1995)].
[5] G. D. Crapper, J. Fluid Mech. **2**, 532 (1957).

Translated by R. M. Durham

# Trajectories of return surface magnetostatic waves in a ferrite–dielectric–metal structure magnetized by a nonuniform ''ridge'' field

V. I. Zubkov and V. I. Shcheglov

*Institute of Radio Engineering and Electronics, Russian Academy of Sciences, Fryazino*
(Submitted April 2, 1998)
Pis'ma Zh. Tekh. Fiz. **25**, 61–66 (December 12, 1999)

Calculations are made of the trajectories of return surface magnetostatic waves (SMSWs) in a ferrite–dielectric–metal structure magnetized by a nonuniform ''ridge'' field. It is shown that there are four different types of trajectories. Conditions are determined for which the return SMSWs propagate in the direction opposite to the forward SMSWs and in the same direction as the forward SMSWs. © *1999 American Institute of Physics.*
[S1063-7850(99)01012-5]

Surface magnetostatic waves (SMSWs) propagating in ferrite films and structures based on them [ferrite–dielectric–metal (semiconductor, superconductor, and so on)] are used in microwave analog information processing devices.[1,2] The nonuniform magnetic field in these devices allows their dimensions to be minimized and new principles of information processing to be implemented.[3] This makes it topical to study the propagation of return SMSWs in a ferrite–dielectric–metal (FDM) structure magnetized by a nonuniform ''ridge'' field $H_g$ and results are presented below.

The FDM structure consists of a ferrite film of thickness $d$ separated from the metal layer by a layer of dielectric of thickness $p$. The $yz$ plane of the coordinate system is parallel to the plane of the ferrite film, the origin is located at the center of the film thickness, and the $x$ axis is perpendicular to the plane of the film.

The field $H_g$ is directed in the plane of the ferrite film parallel to the $z$ axis and has a ''ridge'' configuration.[3,4] Its strength depends quadratically on the $z$ coordinate:

$$H_g = H_0 - H_M z^2 a^{-1}.$$

The top of the ridge is elongated in the direction of the $y$ axis.

The dispersion equation for SMSWs in an FDM structure was studied in detail in Refs. 4 and 5. As a result of the gyrotropic properties of the ferrite film, the direction of the phase velocity vector **k** of the SMSWs differs from the direction of the group velocity vector **s**. The angle between the vector **k** and the $y$ axis will be denoted by $\varphi$ and the angle between the vector **s** and the $y$ axis will be denoted by $\psi$. By definition,[1,2,5] forward waves are those for which the projection of the group velocity vector on the direction of the phase velocity vector is positive and the return waves are those for which this projection is negative. As the SMSW propagates at a constant frequency $f$, it covers sections of the film located in different fields $H_g$.

An analysis shows that all possible types of return SMSW trajectories can be explained taking the example of an SMSW of frequency $f=3650$ MHz in an FDM structure with an yttrium iron garnet film having a saturation magnetization of 1750 Gs, $d=15\,\mu$m and $p=25\,\mu$m, magnetized by the field $H_g$ for $H_0=437.5$ Oe, $H_M=4H_0$, and $a=128\ \text{cm}^{-2}$.

Figure 1 shows dispersion curves of SMSWs with $\varphi=0$ for various fields $H_g$. Curve *1* corresponds to the top of the ridge ($H_g=H_0$). The return SMSWs correspond to the descending sections of the dispersion curves. We shall analyze the excitation of SMSWs at the top of the ridge. It can be seen from Fig. 1 that return SMSWs only exist in the range of fields between $H_0=437.5$ Oe and $H_{\min}=431.9$ Oe (curves *1–4*). This range defines the boundaries of the SMSW propagation channel on the plane of the ferrite film, parallel to the $y$ axis and positioned symmetrically on either side of this axis.

The SMSW trajectories can be conveniently analyzed using frequency contours plotted on the $k_y 0 k_z$ plane.[2,3,5] Figure 2 shows a family of SMSW frequency contours for various fields $H_g$ in the range between $H_0$ and $H_{\min}$. Curve *1* (heavy line) describes the excitation of SMSWs at the top of the ridge. We shall analyze the characteristic points on this curve. The letter *M* denotes the point through which the tangent to the frequency contour $k_z(k_y)$ drawn from the origin passes. The letter *N* denotes the point through which the tangent to the frequency contour parallel to the $k_y$ axis passes. The wave vector **k** corresponds to a ray drawn from the origin to the point of intersection with the contour $k_z(k_y)$. The group velocity vector **s** is perpendicular to the tangent to the frequency contour $k_z(k_y)$ constructed at this point of intersection. The character of the excited SMSWs is determined by the position of the end point of the wave vector **k** on the contour $k_z(k_y)$. If the end of the wave vector **k** lies to the left of point *M*, the waves are forward and if it lies to the right, they are return waves. If the end of the wave vector **k** lies between points *M* and *N*, the return waves propagate in the positive direction of the $y$ axis (like the forward SMSWs[3–5]). If the end of the wave vector **k** lies to the right of point *N*, the return waves propagate in the negative direction of the $y$ axis.

By way of example, Fig. 2 shows two wave vectors: $\mathbf{k}_1$, for which $\varphi=7.4°$, and $\mathbf{k}_2$ for which $\varphi=7.9°$. The corre-

 © 1999 American Institute of Physics

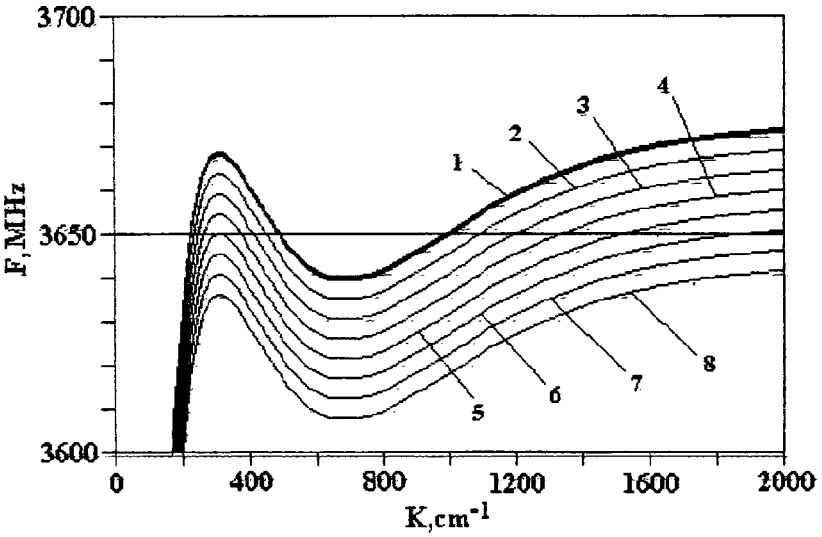


FIG. 1. Dispersion curves of SMSWs for various fields $H_g$, Oe: *1* — 437.5, *2* — 436, *3* — 434.5, *4* — 433, *5* — 431.5, *6* — 430, *7* — 428.5, and *8* — 427.

sponding group velocity vectors are denoted by $\mathbf{s}_1$ and $\mathbf{s}_2$. It can be seen from Fig. 2 that the vector $\mathbf{k}_1$ corresponds to the return waves propagating in the negative direction of the $y$ axis and the vector $\mathbf{k}_2$ corresponds to those propagating in the positive direction. As the SMSWs propagate, the projection of the initial wave vector $\mathbf{k}$ on the $y$ axis is always conserved.[4,5] For $\mathbf{k}_1$ and $\mathbf{k}_2$ this corresponds to the vertical dashed lines parallel to the $k_z$ axis. As the SMSW propagates, it passes successively from the axis of the ridge toward its edge, which corresponds to the end of the wave vector moving along the indicated dashed line toward the $k_y$ axis after which the SMSW again turns toward the ridge axis, which corresponds to the end of the wave vector moving away from the $k_y$ axis. After reaching the ridge axis, the SMSW crosses it and the process repeats, so that the SMSW trajectory is described by a periodic function of constant amplitude.

Figure 3 shows trajectories of return SMSWs constructed for various values of the angle $\varphi$. It can be seen that four different types of trajectory are possible.

1. A pseudosinusoidal trajectory (curve *1*) where the SMSW propagates monotonically in the negative direction of the $y$ axis.

2. A pseudomeander nonself-intersecting $\Omega$-shaped trajectory (curve *2*) — the half-periods of the meander are similar to the Greek letter $\Omega$ with no sections parallel to the abscissa (positive on the normal $\Omega$ and negative on the inverted $\Omega$). The tangents to the trajectory at neighboring points with $z=0$ intersect outside the trajectory. The SMSW as a whole propagates in the negative direction of the $y$ axis but there are sections on which it propagates in the positive direction. The trajectory turns smoothly.

3. A pseudomeander self-intersecting $\Omega$-shaped trajectory (curve *3*). The tangents to the trajectory at neighboring

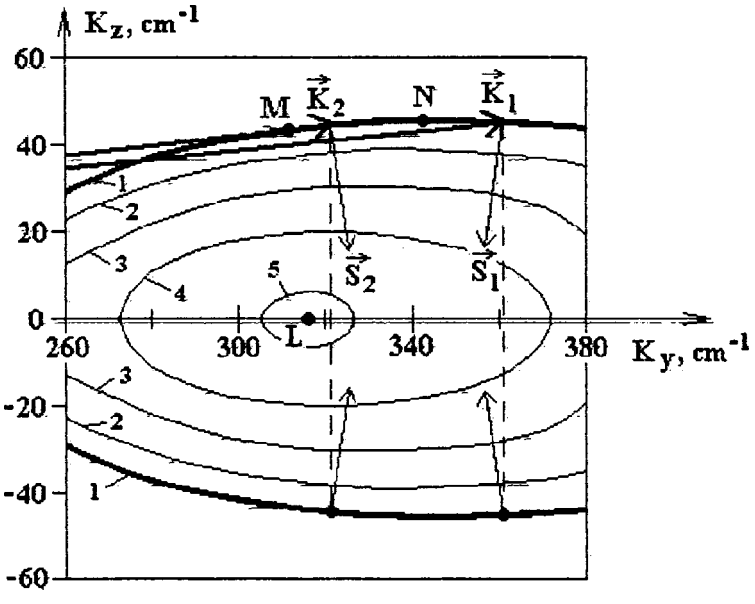


FIG. 2. Frequency contours of SMSW with $f=3650$ MHz for various fields $H_g$, Oe: *1* — 437.5, *2* — 436, *3* — 434.5, *4* — 433, and *5* — 431.9.

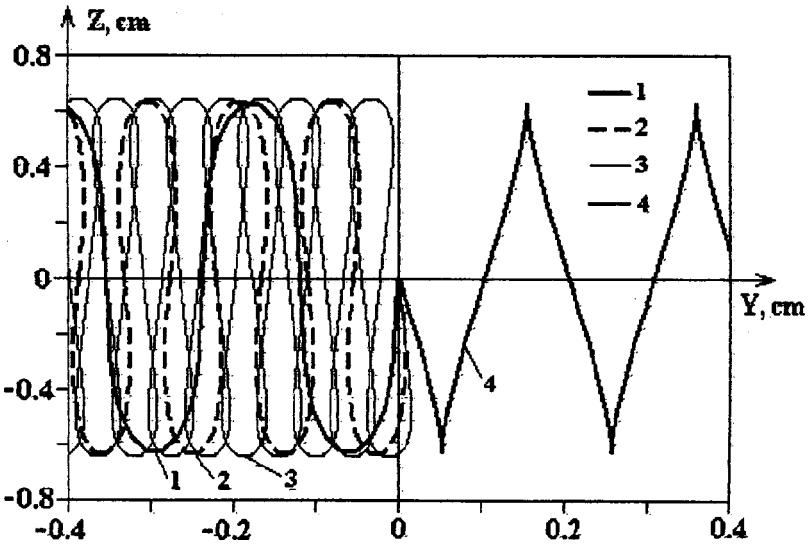


FIG. 3. Trajectories of return SMSWs with $f=3650$ MHz for various initial angles $\varphi$: *1* — 7.4, *2* — 7.6, *3* — 7.7, and *4* — 7.9°.

points with $z=0$ intersect inside the trajectory. The SMSW as a whole propagates in the negative direction of the $y$ axis although the sections on which it propagates in the positive direction of the $y$ axis are so large that the trajectory self-intersects.

4. Pseudosawtooth trajectory (curve *4*). The SMSW as a whole propagates in the positive direction of the $y$ axis although there are sections where it propagates in the negative direction of the $y$ axis. These sections are extremely small and the trajectory turns sharply.

[1] W. S. Ishak, Proc. IEEE **76**, 171 (1988).
[2] A. V. Vashkovskiĭ, V. S. Stal'makhov, and Yu. P. Sharaevskiĭ, *Magnetostatic Waves in Microwave Electronics* [in Russian], Saratov State University Press, Saratov (1993), 312 pp.
[3] A. V. Vashkovksy, V. I. Zubkov, E. H. Lock, and V. I. Shcheglov, Proc. IEEE **26**, 1480 (1990).
[4] A. V. Vashkovskiĭ, V. I. Zubkov, and V. I. Shcheglov, Radiotekh. Elektron. (Moscow) **41**, 1413 (1996).
[5] V. I. Zubkov and V. I. Shcheglov, Radiotekh. Elektron. (Moscow) **42**, 1114 (1997).

Translated by R. M. Durham

# Investigation of the propagation of microwave beams in an inhomogeneous plasma in a magnetic field

D. L. Grekov

*Institute of Plasma Physics, National Scientific Center ''Kharkov Physicotechnical Institute,'' Ukraine*
(Submitted May 18, 1998; resubmitted March 25, 1999)
Pis'ma Zh. Tekh. Fiz. **25**, 67–71 (December 12, 1999)

An analysis is made of the propagation of microwave beams in an inhomogeneous magnetized plasma. It is shown that the presence of a plasma increases the astigmatism of the beams, increases the amplitude of the beam compared with vacuum conditions, and reduces the curvature of their phase fronts compared with vacuum. © *1999 American Institute of Physics.* [S1063-7850(99)01112-X]

The propagation of microwave beams in vacuum has already been studied intensively in connection with problems of transmission lines, resonators, and laser beams.[1]

At present microwave beams are widely used for diagnostics (reflectometry and interferometry) and for rf (microwave) plasma heating. The propagation of microwave fields in a plasma is usually analyzed using a ray trajectory method.

The present paper is devoted to an analysis of the propagation characteristics of microwave beams (10–200 GHz) in an inhomogeneous magnetized plasma. The influence of the separatrix layer of low-density plasma on the distribution of the fields emitted by the antenna is determined for ITER-scale facilities and correct initial conditions are constructed for calculations using the ray trajectory method.

We introduce the Cartesian coordinates $(X,Y,Z)$: $OZ \| \Delta n_e$, $OX \| \mathbf{B}$ (where $n_e$ is the electron concentration and $\mathbf{B}$ is the external magnetic field). The beam propagates mainly in the direction of the $Z$ axis and the emitter is located in the $XY$ plane. For the ordinary wave we have $E_x \geqslant E_y$, $E_z$, and for the extraordinary wave $E_y \geqslant E_z \geqslant E_x$. Since $(\partial E_i/\partial z) \geqslant (\partial E_i/\partial x)$, $(\partial E_i/\partial y)$, we obtain from the Maxwell equations for the *o*-wave $(E_x \equiv E_o)$

$$\frac{\partial^2 E_o}{\partial z^2}+\frac{\omega^2}{c^2}\varepsilon_3 E_o+\frac{\partial^2 E_o}{\partial y^2}+\varepsilon_3\frac{\partial^2 E_o}{\partial x^2}=0 \tag{1}$$

and for the *e*-wave $(E_y \equiv E_e)$

$$\frac{\partial^2 E_e}{\partial z^2}+\frac{\omega^2}{c^2}\frac{\varepsilon_1^2-\varepsilon_2^2}{\varepsilon_1}E_e+\frac{\partial^2 E_e}{\partial y^2}+\left(1+\frac{\varepsilon_2^2}{\varepsilon_1^2}\right)\frac{\partial^2 E_e}{\partial x^2}=0, \tag{2}$$

where

$$\varepsilon_1=1-\frac{\omega_p^2}{\omega^2-\omega_e^2}, \quad \varepsilon_2=\frac{\omega_c}{\omega}\frac{\omega_p^2}{\omega^2-\omega_c^2}, \quad \varepsilon_3=1-\frac{\omega_p^2}{\omega^2}.$$

We obtain solutions of Eqs. (1) and (2) using the parabolic approximation method.[2] These have the form $(\alpha=o,e)$

$$E_\alpha(x,y,z)=-\frac{iA_\alpha}{2\pi}\sqrt{\frac{c}{\omega k_\alpha(z)}}\,[\Psi_{1\alpha}(z)\Psi_{2\alpha}(z)]^{-1/2} \times\exp\left[i\int_0^z k_\alpha(z)dz\right]\int_{-\infty}^{\infty}\int E\alpha(\xi,\eta) \times\exp\left\{\frac{i}{2}\left[\frac{(y-\xi)^2}{\Psi_{2\alpha}(z)}+\frac{(x-\eta)^2}{\Psi_{1a}(z)}\right]\right\}d\xi d\eta. \tag{3}$$

Here we have

$$k_o(z)=\frac{\omega}{c}\varepsilon_3^{1/2}(z), \quad k_e(z)=\frac{\omega}{c}\left[\frac{\varepsilon_1^2(z)-\varepsilon_2^2(z)}{\varepsilon_1(z)}\right]^{-1/2},$$

$$\Psi_{1o}(z)=\frac{c^2}{\omega^2}\int_0^z k_o(z')dz', \quad \Psi_{2o}(z)=\int_0^z dz'/k_o(z'),$$

$$\Psi_{le}(z)=\int_0^z\frac{\varepsilon_1^2(z')+\varepsilon_2^2(z)}{\varepsilon_1^2(z')}\frac{dz'}{k_e(z')},$$

$$\Psi_{2e}(z)=\int_0^z\frac{dz'}{k_e(z')}.$$

For $n_e=0$ the integrals (3) are expressed in terms of Fresnel functions. For vacuum we have $\Psi_{1\alpha}(z)=\Psi_{2\alpha}(z)=zc/\omega$, i.e., $z=\omega\Psi_{1,2\alpha}/c$. The influence of the plasma may be characterized by the effective change in $z$. For the $X$ axis, $z$ becomes $z_\parallel=\omega\Psi_{1\alpha}(z)/c$, and for the $Y$ axis $z_\perp=\omega\Psi_{2\alpha}(z)/c$. Calculations show that the presence of a low-density plasma does not influence the field distribution of the *e*-wave in the boundary layer. However, for the *o*-wave, particularly in the long-wavelength part of this range, the influence may be considerable. In this case, the amplitude distribution of the *o*-wave is not symmetric relative to the toroidal direction which is caused by the influence of the low-density plasma.

In order to make a detailed analysis of the propagation of the *o*-wave we shall seek a solution of Eq. (1) in the form

$$E_o=\sqrt{\frac{c}{\omega k_o(z)}}\exp\left[-i\int_0^z k_o(z')dz'\right]A(x,y,z).$$

For $A(x,y,z)$ we then obtain

 © 1999 American Institute of Physics

$$\frac{c^2k_o^2(z)}{\omega^2}\frac{\partial^2 A}{\partial x^2}+\frac{\partial^2 A}{\partial y^2}-i2k_o(z)\frac{\partial A}{\partial z}=0. \quad (4)$$

It is well-known that the solutions of the diffusion equation (4) may be expressed in the form

$$A(x,y,z)=A_0H_m\left(\frac{\sqrt{2}x}{w_\parallel(z)}\right)H_n\left(\frac{\sqrt{2}y}{w_\perp(z)}\right)\times\exp\left\{-i\left[P(z)+k_o(z)\left(\frac{x^2}{2q_\parallel}+\frac{y^2}{2q_\perp}\right)\right]\right\}, \quad (5)$$

where $H_n(x)$ are Hermite polynomials. We shall analyze the propagation of the dominant mode $m=n=0$. Expressing $q_\alpha$ in the form

$$\frac{1}{q_\alpha}=\frac{1}{R_\alpha(z)}-\frac{2i}{k_o(z)w_\alpha^2(z)},$$

where $R_\alpha$ are the radii of curvature of the wavefront in the $X$ or $Y$ direction, and $w_\alpha$ are the beam dimensions in these directions, we obtain

$$w_\perp(z)=w_{\perp0}\left\{1+\left[\frac{2}{w_{\perp0}^2}\int_0^z\frac{dz'}{k_o(z')}\right]^2\right\}^{1/2}, \quad (6)$$

$$w_\parallel(z)=w_{\parallel0}\left\{1+\left[\frac{2c^2}{\omega^2w_{\parallel0}^2}\int_0^z k_o(z')dz'\right]^2\right\}^{1/2}, \quad (7)$$

$$R_\perp(z)=k_o(z)\int_0^z\frac{dz'}{k_o(z')}\left\{1+\left[\frac{2}{w_{\perp0}^2}\int_0^z\frac{dz'}{k_o(z')}\right]^{-2}\right\}, \quad (8)$$

$$R_\parallel(z)=\frac{c^2k_o(z)}{\omega^2}\int_0^z k_o(z')dz'\times\left\{1+\left[\frac{2c^2}{\omega^2w_{\parallel0}^2}\int_0^z k_o(z')dz'\right]^{-2}\right\}, \quad (9)$$

$$iP(z)=\frac{1}{2}\int_0^z\frac{1}{i\frac{w_{\perp0}^2}{2}+\int_0^{z'}\frac{dz''}{k_o(z'')}}\frac{dz'}{k_o(z')}+\frac{1}{2}\int_0^z\frac{k_o(z')dz'}{\frac{i\omega^2w_{\parallel0}^2}{c^2}+\int_0^{z'}k_o(z'')dz''}. \quad (10)$$

Separating the real and imaginary parts in the expression for $iP(z)$, we can find the differences in the phase and amplitude of a bounded wave beam and a plane wave:

$$A(z,x=0,y=0)=A_0\left\{1+\frac{4}{w_{\perp0}^4}\left[\int_0^z\frac{dz'}{k_o(z')}\right]^2\right\}^{-1/4}\times\left\{1+\frac{4c^4}{\omega^4w_{\parallel0}^4}\left[\int_0^z k_o(z')dz'\right]^2\right\}^{-1/4}\times\exp\frac{i}{2}\left\{\arctan\left[\frac{2}{w_{\perp0}^2}\int_0^z\frac{dz'}{k_o(z')}\right]+\arctan\left[\frac{2c^2}{\omega^2w_{\parallel0}^2}\int_0^z k_o(z')dz'\right]\right\}. \quad (11)$$

We shall analyze the differences in the propagation of wave beams in vacuum and in a plasma using expressions (6)–(9) in the low-density plasma approximation ($\omega_p^2(z)\ll\omega^2$).

1. Compared with a vacuum, the presence of a plasma causes narrowing of the beam parallel to the magnetic field and broadening perpendicular to the magnetic field

$$w_\parallel=w_{\parallel0}[1+D^2(1-\omega_p^2(\overline{z})/\omega^2)]^{1/2},$$

$$w_\perp=w_{\perp0}[1+D^2(1+\omega_p^2(\overline{z})/\omega^2)]^{1/2}.$$

Here we have

$$\frac{\omega_p^2(\overline{z})}{\omega^2}=\frac{1}{z}\int_0^z\frac{\omega_p^2(z')}{\omega^2}dz',\quad D=\frac{2\lambda z}{w_{\alpha0}^2}.$$

2. When wave beams propagate in a plasma, the curvature of their phase fronts decreases compared with vacuum. For the direction parallel to the magnetic field the defocusing in the ''far-field'' zone ($D\gg1$) is greater than that in the near-field zone ($D\ll1$) and for the perpendicular direction the reverse is true:

$$R_\parallel=R_{\rm vac}\left[1-\frac{\omega_p^2(z)+\omega_p^2(\overline{z})}{2\omega^2}\right],\quad D\gg1,$$

$$R_\parallel=R_{\rm vac}\left[1-\frac{\omega_p^2(z)-\omega_p^2(\overline{z})}{2\omega^2}\right],\quad D\ll1,$$

$$R_\perp=R_{\rm vac}\left[1-\frac{\omega_p^2(z)-\omega_p^2(\overline{z})}{2\omega^2}\right],\quad D\gg1,$$

$$R_\perp=R_{\rm vac}\left[1-\frac{\omega_p^2(z)+\omega_p^2(\overline{z})}{2\omega^2}\right],\quad D\ll1;$$

3. The presence of a plasma increases the beam amplitude compared with vacuum and this effect does not depend on the plasma density profile.

It is interesting to note that the presence of a plasma leads to astigmatism of the ordinary and extraordinary wave beams. Moreover the astigmatism of the ordinary wave does not depend on the plasma gyrotropy.

[1] H. Kogelnik and T. Li, Appl. Opt. **5**, 1550 (1966).
[2] V. A. Fock, *Electromagnetic Diffraction and Propagation Problems* (Pergamon Press, New York, 1965), 320 pp.

Translated by R. M. Durham

# Deep diffusion doping of macroporous silicon

E. V. Astrova, V. B. Voronkov, I. V. Grekhov, A. V. Nashchekin, and A. G. Tkachencko

*A. F. Ioffe Physicotechnical Institute, Russian Academy of Sciences, St. Petersburg*
(Submitted July 16, 1999)
Pis'ma Zh. Tekh. Fiz. **25**, 72–79 (December 12, 1999)

An investigation is made of the diffusion of boron and phosphorus impurities in macroporous silicon with a regular structure of deep cylindrical pores, for which through doping of the walls was achieved. The $\sim 150\,\mu$m layers obtained were quasiuniformly doped and had a planar diffusion front, and their electric parameters were very similar to those of the doped single crystal. It is demonstrated that deep diffusion of phosphorus may be used to fabricate $n$–$n^+$ structures. © *1999 American Institute of Physics.* [S1063-7850(99)01212-4]

## INTRODUCTION

The development of the technology to produce deep cylindrical pores 0.6–20 $\mu$m in diameter and up to 500 $\mu$m deep[1–4] in *n*-type silicon opens up extensive prospects for using this material in various fields.[5–9] Macroporous anisotropic silicon ($ma$–Si) is also a promising material for electronics. Unlike microporous silicon, macroporous silicon has a low porosity ($<10\%$) and in many respects retains the properties of the single crystal. Thus, macroporous silicon may be considered as some new material having effective values of macroscopic parameters, such as resistivity, permittivity, and so on. The aim of the present paper is to study various possibilities for using macroporous silicon to fabricate semiconductor structures.

## FABRICATION TECHNOLOGY FOR MACROPOROUS SILICON

The starting material was ⟨100⟩-oriented non-crucible zone-refined *n*-type silicon having resistivity $\rho = 200\,\Omega\cdot$cm. After thermal oxidation, the 400 $\mu$m thick polished wafers underwent photolithographic treatment which opened up a square network of circular holes in the oxide 10 $\mu$m in diameter and $a = 30\,\mu$m apart. Standard alkali etching formed pits in the oxide, in the form of inverted pyramids with a square surface. Deep pores were etched electrochemically using a 2.5% aqueous solution of HF for 4 h with the back of the wafer illuminated by its self-emitted light ($\lambda \leqslant 800$ nm) at 4 V and current density $j = 1.66$ mA/cm$^2$, which corresponds to a current $I_{pp} = 15$ nA per pore. The shape and size of the pores was monitored using a transverse cleaved section of the sample using a scanning electron microscope (see Figs. 1a and 1b). These pores had a depth $l = 120\,\mu$m and diameter $d = 10\,\mu$m, and their density was $1.1\times 10^5$ pore/cm. These technological parameters correspond to a stable etching regime when the current density at the bottom of the pore is equal to the critical current density for transition to electropolishing $j_{ps} = 20$ mA/cm$^2$ (Ref. 2) and the diameter is satisfactorily described by[3]

$$d = a(j/j_{ps})^{1/2} = 8.6\,\mu\text{m}.$$

The porosity is easy to estimate using the formula

$$p = \frac{\pi}{4}\left(\frac{d}{a}\right)^2,$$

which in our case gives $p = 8.7\%$.

## DOPING OF MACROPOROUS SILICON

Previous attempts have been made to use a porous structure to introduce slowly diffusing impurities into silicon. However, the method has not been widely used because of the radical difference between the properties of ''ordinary'' microporous silicon and single-crystal Si. Using macroporous silicon can avoid this major disadvantage. There have already been reports of this being used to form deep vertical *p*-walls preventing the breakdown of high-voltage $p$–$n$ junctions along their edges.[11] The regular pore structure used by us can produce well-controlled porous layers having the same wall thickness, which ensures uniform doping of the porous layer when a diffusion source is introduced into the inner surface of the pores (Fig. 1c). In order to achieve through doping of the walls with boron acceptor impurities, the diffusion zones must overlap in the horizontal plane and the diffusion front must be equalized near the lower part of the pores. If the depth of the $p$–$n$ junction in the single-crystal silicon is $x$, the following condition must be satisfied for the boundaries of the $p$–$n$ junctions to close around the pores

$$x_{j_{\min}} = \frac{1}{2}(\sqrt{2}a - d),$$

i.e., for our samples $x_{j_{\min}} = 16.2\,\mu$m. Attention should be drawn to the fact that if the scale of the entire structure is changed, for example, by reducing $a$ and $d$ with the ratio $d/a$ kept constant, the depth $x_j$ may be reduced but the properties of the material are conserved, since the porosity remains the same. For example, for $a = 3\,\mu$m and $d = 1\,\mu$m we obtain $x_{j_{\min}} = 1.62\,\mu$m and to obtain a $p$–$n$ junction of this depth the temperature and duration of diffusion may be reduced appreciably.

 © 1999 American Institute of Physics

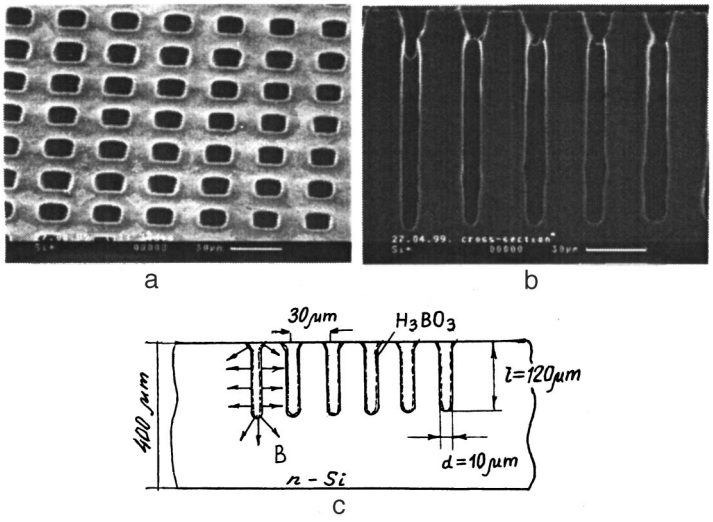


FIG. 1. Macropores in Si: a and b — SEM images, c — diagram showing introduction of dopant.

## DIFFUSION OF BORON

In our experiments macroporous silicon was doped with boron from a 1% alcohol solution of $H_3BO_3$ at $T=1250°C$ for 3 h to the depth $x_j=30\ \mu$m in the single-crystal region, which is almost twice $x_{j_{\min}}$. This allowed us to obtain a $p-n$ junction 150 $\mu$m deep in the macroporous silicon (see Fig. 2). Staining a polished section showed that the boundary of the $p-n$ junction is horizontal in the region where the pores enter the plane of the cross section and between rows (see Fig. 3).

The resistivity was measured using a four-probe method in the porous and single-crystal regions immediately after diffusion (Figs. 2a and 2b) and after grinding the $p$-layer in the single-crystal region (Fig. 2c). These values are given in

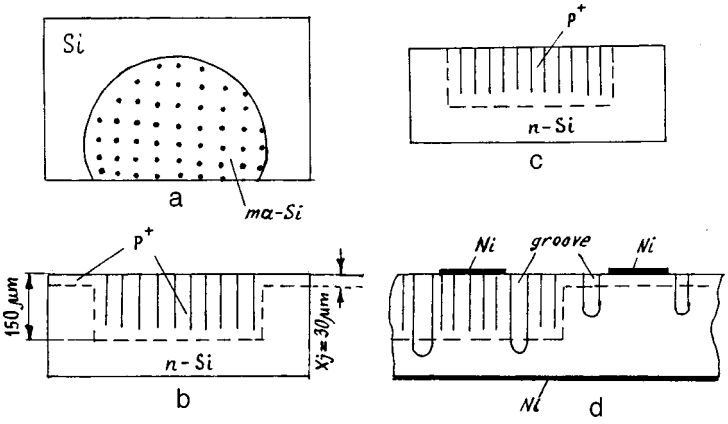


FIG. 2. Schematic of sample structure: a) top view; deep pores etched in central region; b) cross section; c) cross section after grinding a 35 $\mu$m thick layer from above; d) structure to measure the parameters of a $p-n$ junction on single-crystal and macroporous Si.

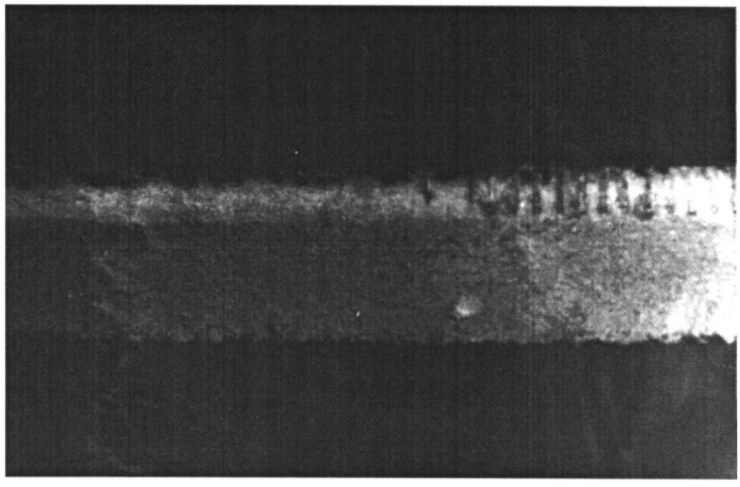

FIG. 3. Optical-microscope image of cross section through boron-doped macroporous silicon sample after exposing $p-n$ junction (the $p$ region is a light color). On the left-hand side of the photograph the pores do not reach the plane of the polished section although the formation of a deep $p-n$ junction can be seen.

TABLE I. Parameters of layers obtained by boron diffusion.

| | | $R_s$, Ω/□ | $\rho$, Ω·cm | $N_B$, cm$^{-3}$ | $\tau_p$, μs |
|---|---|---|---|---|---|
| After diffusion | Single-crystal Si | 0.261 | $7.5\times10^{-4}$ | $1.8\times10^{20}$ | 8 |
| After diffusion | Macroporous Si | 0.168 | $2\times10^{-3}$ | $6\times10^{19}$ | 4 |
| After removing 35 μm | Macroporous Si | 0.470 | $4\times10^{-3}$ | $3\times10^{19}$ | |

Table I where the average resistivity of the layer $\overline{\rho}=R_S\cdot x_j$, and the corresponding average boron concentration $\overline{N_B}$ are taken from published data for uniformly doped single-crystal silicon.[12] In regions with and without pores we fabricated $p$–$n$ junctions with vertical walls, obtained by mechanical polishing an annular groove, and Ni contacts (Fig. 2d). These structures were used to measure the hole lifetimes $\tau_p$ by the Lax method. Table I gives values of $\tau_p$ measured by switching from the forward current $I_j=100$ mA to the reverse $I_r=50$ mA in the single-crystal and macroporous Si regions, respectively. It can be seen that $\overline{\rho}$ for doped macroporous silicon is slightly higher than that for single-crystal silicon although this has a sufficiently low value for many applications and $\tau_p$ is slightly lower.

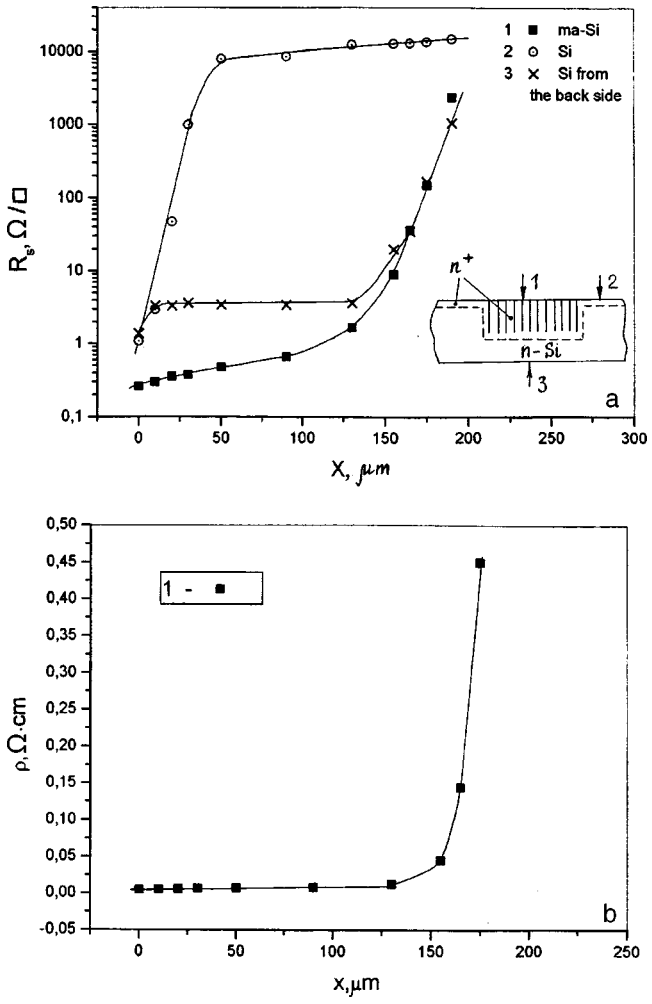


FIG. 4. Resistivity distribution in various regions of the sample after phosphorus diffusion: a — surface resistivity, b — volume resistivity in region containing pores.

## DIFFUSION OF PHOSPHORUS

Diffusion of phosphorus into macroporous silicon with a pore depth $l=165$ μm was carried out using a 10% alcohol solution of $H_3PO_4$ at 1240°C for 5 h ($x_j=25$ μm). Figure 4a shows the depth distribution of the surface resistance $R_s$ obtained as a result of layer-by-layer grinding of the sample on the pore side. The measurements were made in regions *1*, *2*, and *3* shown on the inset. Note that the shunting influence of the lower *n*-Si layer can be neglected when analyzing the results of the measurements in regions *1* and *2* since its resistance is several orders of magnitude higher than the resistance of the diffusion layer. It can be seen that in the single-crystal region *2*, the $n^+$ layer ceases to have an influence at $x\approx50$ μm whereas for the macroporous silicon region *1* this is ~200 μm. The resistivity of phosphorus-doped macroporous silicon estimated using the formula $\overline{\rho}=R_s\times(l+x_j-x)=R_s(190-x)\times10^{-4}$ Ω·cm is plotted in Fig. 4b. It can be seen that $\overline{\rho}$ remains low as far as values of $x$ corresponding to the pore depth.

The standard substrate for the formation of bipolar devices is a highly doped thick $n^+$ layer. Its role is to reduce the thickness of the base and thus the resistance connected in series with the $p$–$n$ junction. This $n$–$n^+$ structure is usually fabricated by epitaxial growth of thin *n*-Si on a highly doped substrate or a thick $n^+$ layer on single-crystal Si whose thickness is then reduced (''inverted'' epitaxial structures). By using deep doping of macroporous silicon with donor impurities, it is possible to replace the existing epitaxial technology for fabricating $n$–$n^+$ structures with diffusion technology. Measurements of $R_s$ in region *3* (Fig. 4a) demonstrate an effective reduction in the resistance achieved using this type of layer. Because of the low porosity of macroporous silicon this substrate should possess good mechanical strength and the problem of compatibility between this technology and other operations involved in fabricating devices may be resolved by masking the inner surface of the pores with thermal oxide. There is reason to assume that replacing the complex and ecologically harmful epitaxy processes with relatively simple etching and diffusion processes is economically viable.

## CONCLUSIONS

We have therefore confirmed that replacing single-crystal silicon with macroporous silicon can appreciably increase the thickness of the diffusion layers while negligibly changing the properties of the material and can be used to fabricate device structures, in particular $n$–$n^+$ structures to produce a thick $n^+$ layer.

This work was financed by the RFBR Program of Support for Scientific Schools and the Ministry of Science Program ''Physics of Solid-State Nanostructures.''

[1] V. Lehmann and H. Föll, J. Electrochem. Soc. **137**, 653 (1990).
[2] V. Lehmann, J. Electrochem. Soc. **140**, 2836 (1993).
[3] V. Lehmann, Thin Solid Films **255**, 1 (1995).
[4] V. Lehmann and U. Gruning, Thin Solid Films **297**, 13 (1997).
[5] U. Gruning, V. Lehmann, S. Ottow, and K. Bush, Appl. Phys. Lett. **68**, 747 (1996).
[6] U. Gruning, V. Lehmann, S. Ottow, and K. Bush, Thin Solid Films **276**, 151 (1996).
[7] A. Birner, U. Gruning, S. Ottow, S. Schneider, F. Muller, V. Lehmann, H. Föll, and U. Gösele, Phys. Status Solidi A **165**(1), 111 (1998).
[8] V. V. Aristov, V. V. Starkov, X. Shabel'nikov, S. M. Kusnetsov, A. P. Ushakov, V. V. Grigoriev, and V. M. Tseitlin, Opt. Commun. **161**, 203 (1999).
[9] A. M. Rossi, G. Amato, L. Boarino, and C. Novero, in *Abstracts of the European Materials Research Society Spring Meeting, Strasbourg, France, 1999*, Abstract No. I–I11.
[10] V. Lehmann, W. Honlein, H. Reisinger, A. Spitzer, H. Wendt, and Y. Willer, Thin Solid Films **297**, 321 (1997).
[11] G. Amato, L. Boarino, N. Brunetto, and M. Turnaturi, Thin Solid Films **297**, 321 (1997).
[12] S. M. Sze, *Physics of Semiconductor Devices* (Wiley, New York, 1969; Énergiya, Moscow, 1973, 656 pp.).

Translated by R. M. Durham

# Evolution of the morphological structure of a two-dimensional cluster obtained with a linear microparticle trajectory in the diffusion-limited aggregation regime

D. B. Berg

*Urals State Technical University, Ekaterinburg*
*Institute of Industrial Ecology, Urals Branch of the Russian Academy of Sciences, Ekaterinburg*
(Submitted May 11, 1999)
Pis'ma Zh. Tekh. Fiz. **25**, 80–85 (December 12, 1999)

Two-dimensional diffusion-limited aggregation of spherical microparticles was achieved experimentally as a result of their rectilinear motion (''ballistic aggregation'') at a ''water–air'' interface. A percolation cluster was obtained and the evolution of its morphological parameters was studied under compression. A change in the orientation of the cluster pores and a nonlinear coalescence and breakup process were observed. A fabrication technology is proposed for monolayer films similar to the Langmuir method. © *1999 American Institute of Physics.* [S1063-7850(99)01312-9]

## 1. INTRODUCTION

Aqueous suspensions of microparticles (such as latex microspheres) of the same micrometer dimensions have been successfully used to study crystallization processes in ''ideal'' systems in which the colloidal particles are atoms.[1,2] Two-dimensional crystallization–melting processes can be observed in a planar sandwich cell, whose thickness does not exceed two or three particle diameters[3] or by positioning microspheres at a planar ''water–air' interface.[4] Depending on the type of microsphere and the so-called ''anti-ions'' added to the aqueous medium, it is possible to obtain a broad spectrum of structures, ranging from a dense crystal lattice (such as hexagonal) to branching dendritic and fractal forms.[5] Their formation is described in terms of universal growth mechanisms, i.e., diffusion- and reaction-limited aggregation[6,7] which have different probabilities of particle attachment to the cluster (the analog of surface tension). In general, these regimes are established for different particle trajectories, i.e., Brownian (random walk) and ballistic (rectilinear motion).[8] As a result of collisions between water molecules and microparticles during aggregation in a suspension, the particles undergo Brownian motion.[9] Ballistic aggregation has only been observed experimentally in a low-density gas atmosphere or vacuum during the condensation of evaporated material vapor when the particle mean free path exceeded the dimensions of the growing cluster.[8]

In the present study ballistic diffusion-limited aggregation of microparticles was achieved experimentally at a water–air interface.

## 2. EXPERIMENTAL METHOD OF BALLISTIC DIFFUSION-LIMITED AGGREGATION

Ballistic aggregation of microparticles takes place at the surface of a water droplet lying freely on a transparent glass

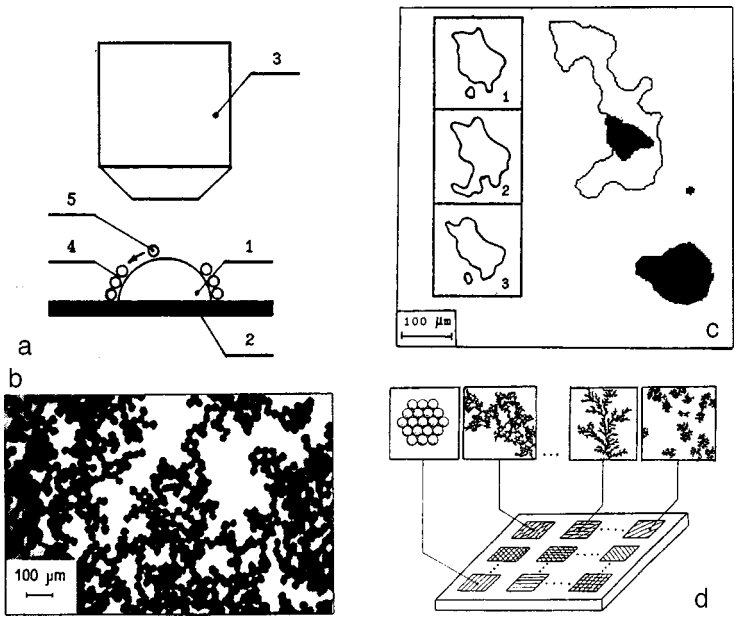


FIG. 1. Microparticle cluster at water–air interface: a — formation of cluster and its observation using an optical microscope, side view (schematic): 1 — droplet, 2 — transparent substrate, 3 — objective, 4 — growing microparticle cluster, 5 — separate particle, after reaching the droplet surface this moves in the radial direction indicated by the arrow; b — cluster in upper part of droplet, viewed from above; c — breakup of large cluster pore (initial position shown by the contour) into smaller ones (shown black) under compression; inset — merging of two pores over time; d — solid substrate on which various functional microparticle monolayers are deposited.

 © 1999 American Institute of Physics

TABLE I. Evolution of morphological parameters of percolation cluster pores under compression.

| Degree of compression of cluster,% | Top view of cluster, pores shown in black | Orientational dependence of average Fere diameter $D_f$ | Distribution of form factors $F_f$ |
|---|---|---|---|
| 0 | 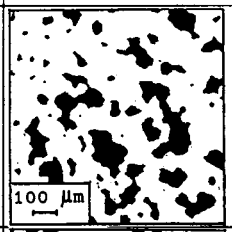  | 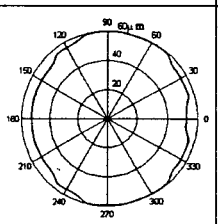 | 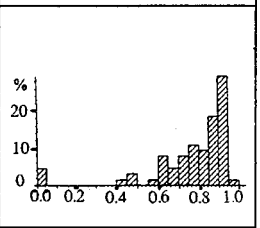 |
| 13.7 | | 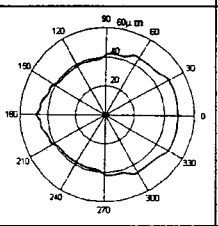 | 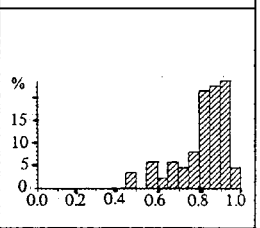 |
| 37.5 | | 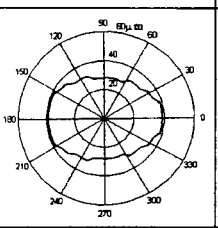 | 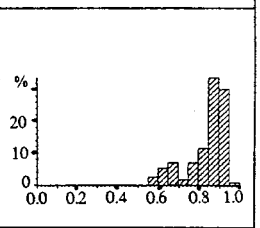 |
| 44.4 | | 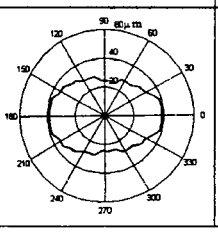 | 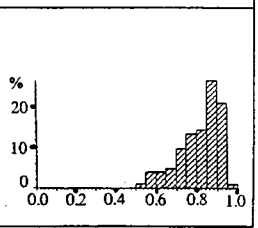 |

substrate, as shown in Fig. 1a. The volume of the droplet is 20–40 $\mu$l, the diameter of the contact spot with the substrate is 3–4 mm, and the initial height 2–3 mm. A microparticle deposited on the surface rolls downward in a radial direction under the action of gravity and attaches to a cluster which grows from the edge toward the center. The cluster grows in the form of branches elongated radially in the direction opposite to the moving particles. The pores are also oriented in this direction. The length of a branch generally does not exceed 6–8 particles since ''restructuring'' is observed at longer lengths,[8] i.e., the entire branch rotates about the contact with the cluster at the base of the branch until a second contact forms. The microparticles are added singly, and gradually fill the entire surface of the droplet, forming a two-dimensional percolation cluster, as shown in Fig. 1b, whose fractal dimension is $1.95 \pm 0.02$ (Ref. 8).

The cluster becomes compressed as the surface area of the droplet decreases as a result of drying and this compression is determined from the specific area of the pores on the image or from the shadow of the droplet. The rate of compression is regulated by the rate of drying. The evolution of the percolation cluster is determined from the morphological parameters of its pores: the perimeter, area, form factor $F_f$, and the orientation according to the angular dependence of the Fere diameter $D_f$ (Ref. 10), i.e., the length of the pore projection in a given direction.

A quantitative microanalysis was made using the Siams image analysis hardware and software (Ekaterinburg) for a cluster in the upper part of the droplet where there are no distortions. The microparticles were *Lycopodium clavatum* microspores, spheres of uniform 37 $\mu$m diameter, which allowed the aggregation process to be observed directly under a microscope.[11] These microparticles have a hydrophobic surface and on a planar water–air interface form typical fractal clusters consistent with the cluster–cluster diffusion-limited aggregation of wax microspheres[9] having fractal dimensions of $1.48 \pm 0.03$.

### 3. EVOLUTION OF CLUSTER MORPHOLOGICAL STRUCTURE

The following laws governing the changes in the morphological parameters of the cluster pores were identified (Table I):

– the shape of the pores becomes more rounded and the form factor distribution becomes narrower;

– the pores not only break up but also merge, as shown in Fig. 1c;

– the average areas and perimeters decrease monotonically;

– the direction of orientation of the pores changes.

## 4. ANALOGY WITH THE LANGMUIR METHOD

Microparticles at the surface of a droplet may be replaced by amphiphilic molecules which become oriented at the water–air interface. Compression of the monolayer as the droplet evaporates will then correspond to the motion of the barrier which compresses the monomolecular layer at the surface of the aqueous subphase in a Langmuir tank.[12] Thus, the proposed method can be used to compress microparticle monolayers to small areas (less than $0.3\,cm^2$) and may be used to deposit films for various purposes on a solid substrate (crystal, amorphous, Langmuir films, and so on). The microparticles may be macromolecules, permolecular aggregates of macromolecules and their complexes (such as enzyme–substratum, antigen–antibody), microspheres (polymer, ceramic, and so on), and other supramolecular objects which become oriented at a water–air interface.

This work was partially supported by a grant from the Ministry of General and Professional Education for Fundamental Problems in the Natural Sciences and by the International Research and Development Program of the Russian Universities ''New Organic Materials for Molecular Electronics'' (OMMEL).

[1] J. Prost and F. Rondelez, Nature (London) **350**, No. 6319, Suppl., 11 (1991).
[2] P. N. Pusey, J. Phys. (Paris) **48**, 709 (1987).
[3] C. A. Murray and D. H. Van Winkle, Phys. Rev. Lett. **58**, 1200 (1987).
[4] P. Pieranski, Phys. Rev. Lett. **45**, 569 (1980).
[5] A. T. Skjeltorp and G. Helgesen, in *Random Fluctuations and Pattern Growth: Experiments and Models*, edited by H. E. Stanley and N. Ostrowsky, NATO ASI Series, Series E, Applied Sciences, Vol. 157 (Kluwer, Dordrecht, 1989), pp. 56–61.
[6] M. Y. Lin, H. M. Lindsay, D. A. Weitz *et al.*, J. Phys.: Condens. Matter **2**, 3093 (1990).
[7] M. Y. Lin, H. M. Lindsay, D. A. Weitz *et al.*, Phys. Rev. A **41**, 2005 (1990).
[8] B. M. Smirnov, *Physics of Fractal Clusters* [in Russian], Nauka, Moscow (1991), 135 pp.
[9] R. Jullien and R. Botet, *Aggregation and Fractal Aggregates* (World Scientific, Singapore, 1987), 120 pp.
[10] Kieshi Gotoh, Powder Technol. No. 1, 5 (1984).
[11] R. I. Mintz and D. B. Berg, in *Abstracts of the Seventh International Conference on Organized Molecular Films*, Ancona, Italy, 1995, p. 36.
[12] A. W. Adamson, *The Physical Chemistry of Surfaces*, 4th ed. (Wiley, New York, 1982; Mir, Moscow, 1979, 540 pp.).

Translated by R. M. Durham

# Hyperfine structure of magnetic-resonance electrical conductivity of doped polydiacetylene

M. K. Kerimov and É. Z. Aliev

*Department of Radiation Research, Academy of Sciences of Azerbaijan, Baku*
(Submitted March 17, 1997; resubmitted April 10, 1999)
Pis'ma Zh. Tekh. Fiz. **25**, 86–90 (December 12, 1999)

Magnetic resonance with a hyperfine structure which can be detected from the electrical conductivity has been observed in iodine-doped polydiacetylene films. This resonance is attributable to transitions between Zeeman levels in the spin-dependent carrier transfer process in a system of localized paramagnetic centers. © *1999 American Institute of Physics.* [S1063-7850(99)01412-3]

The paramagnetism characteristic of most organic semiconductors together with the electrical conductivity which can be varied within twelve orders of magnitude by doping, create favorable conditions for identifying a correlation between the systems of paramagnetic centers and charge carriers.

This correlation is achieved in particular as a result of carrier hopping via localized states, including paramagnetic ones, and is observed as a drop in the electrical conductivity under the action of a static magnetic field.[1–3] Magnetic resonance was observed for the first time in Ref. 4, where it was recorded in polyacetylene from a change in the electrical conductivity, which was interpreted as a change in the carrier hopping probability in a polaron–soliton pair under the combined action of static and alternating magnetic fields.

In the present paper we report data on the first observations of a magnetic resonance hyperfine structure detected from the conductivity of iodine-doped polydiacetylene. It is shown that the effect is of a general nature, without using soliton–polariton concepts and can be used to determine some quantitative characteristics of charge carrier transport.

We investigated polydiphenyldiacetylene (PDA) films prepared by pouring from a chloroform solution onto quartz substrates with copper electrodes 10 mm high and 0.1 mm apart. After drying in vacuum, the films were doped with iodine at room temperature by diffusion from vapor to a concentration of $2.0\times10^{19}\,g^{-1}$. As a result of the doping, the conductivity of the samples increased from $1.4\times10^{-11}$ to $6.0\times10^{-4}\,\Omega^{-1}\,cm^{-1}$, and the spin concentration after doping was $1.5\times10^{19}\,g^{-1}$.

The conductivity of the samples was measured under ESR conditions by detecting the voltage drop at a modulation frequency of 100 kHz at a load resistor positioned outside the magnetic fields. The voltage applied to the sample was 1–100 V.

The relative change in the conductivity of the PDA film as a function of the magnetic field strength has the form of a saturating curve which was described in detail in Refs. 1–3. The only difference from the known curves is that as the magnetic field increases, the section corresponding to saturation reveals a slight increase before reaching the limiting value in the range $H_b \simeq 4$ kOe. In addition, in the range $H = 3.3$ kOe we observed a resonant increase in the conductivity of the sample in the form of a peak having full width at half-maximum $\Delta H_{1/2} = 12$ Oe.

Figure 1 shows spectra of the resonant change in the conductivity of PDA obtained for a microwave magnetic field of 0.3 Oe and for various values of the electric field at the sample. It can be seen that the resonant increase in the conductivity exhibits a clearly defined hyperfine structure in the form of a three-component spectrum, which may be represented as the superposition of a singlet with the *g*-factor $g_1 = 2.0027$ and a doublet with $g_2 = 2.0035$ and the hyperfine splitting constant $a = 12$ Oe.

In order to explain the influence of the magnetic fields on the electrical conductivity of doped PDA, we shall take the system for hopping of charge carriers in the spin system proposed in Refs. 1–4

$$^{1,3}[\dot{h}^+ + \dot{R}] \rightarrow {}'[h^0 + R^+], \tag{1}$$

where $\dot{R}$ and $R^+$ are a neutral paramagnetic and corresponding charged spinless structural defect, $\dot{h}^+$ is a hole formed by capture of an electron by an acceptor (iodine), and $h^0$ is the neutral diamagnetic unit of the polymer chain. The magnetic sensitivity of process (1) is caused by the difference between the spins states of the reacting particles on the right- and left-hand sides of the reaction, for which the charge hopping frequency will depend on the magnetic field mixing efficiency of the singlet $S$ and triplet $T_{0,\pm}$ states in the pairs $(\dot{h}^+ \ldots \dot{R})$.

The action of the microwave magnetic field induces resonant transitions between the mixed $S - T_0$ level and the $T_\pm$ levels, which leads to binding of all the levels in the spin system and ensures an effective yield in the singlet channel for the carrier hopping. Thus, under the action of the microwave field the $(\dot{h}^+ \ldots \dot{R})$ pair lifetime decreases and consequently the conductivity of the polymer increases resonantly.

The observed conductivity spectrum corresponds to allowed transitions between the magnetic spin levels of the paramagnetic partners in the pairs when a spin 1/2 magnetic nucleus is present in the structure of one of the partners.

 © 1999 American Institute of Physics

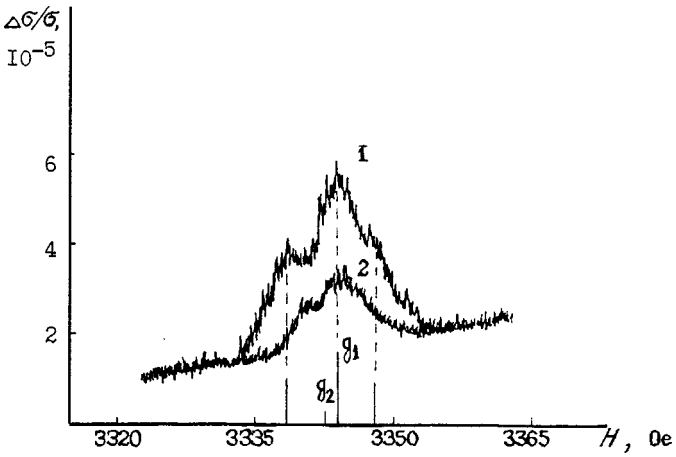


FIG. 1. Spectra of the resonant change in the electrical conductivity of doped PDA for various electric field intensities: *1* — $E=1\times10^2$ V/cm, *2* — $E=6\times10^3$ V/cm.

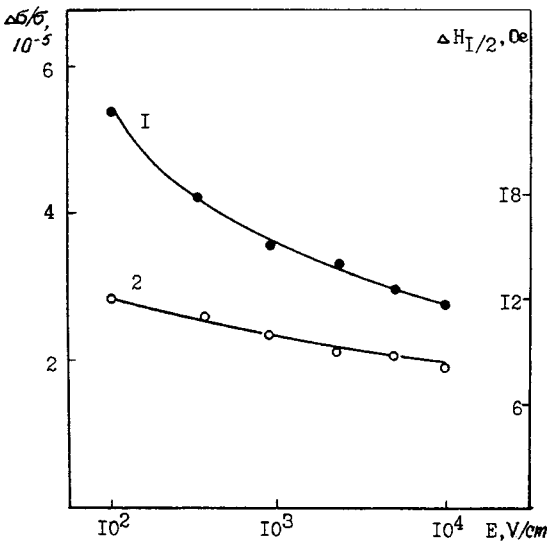


FIG. 2. Dependence of the amplitude (*1*) and width (*2*) of the spectrum of resonant change in the conductivity of PDA on the electric field intensity.

The nonresonant increase in the conductivity with increasing $H$ is evidently caused by the so-called $\Delta g$ mechanism when as a result of a difference between the Zeeman precession frequencies of the spins $\dot{h}^+$ and $\dot{R}$ the magnetic field mixes the $S$ and $T_0$ states with the frequency $\omega_{ST_0}=|g_2-g_1|\beta H/2\hbar$ and thereby increases the carrier hopping frequency $\tau^{-1}$ with increasing $H$. For effective $S-T_0$ mixing the condition $T_1^{-1}<\tau^{-1}<\omega_{ST_0}$ should be satisfied ($T_1^{-1}$ is the spin relaxation rate) which determines the magnetic field at which saturation is achieved $H_B\gtrsim 2\hbar/\Delta g\beta T$ (Ref. 5). Substituting the values for PDA $\Delta g=8\times10^{-4}$ and $T_1=0.8\times10^{-7}$ s we find $H_B\gtrsim 4.6\times10^3$ Oe which is close to the experimentally observed value of $H_B$. The maximum effect did not exceed $3\times10^{-4}$.

The individual spectral line width $\delta H$ can be used to estimate the fixed carrier lifetime $\tau_0\simeq\hbar/g\beta\delta H\simeq 2\times10^{-8}$ s. This value of $\tau_0$ can be used to estimate the carrier mobility $\mu\simeq e\overline{l}^2/6kT\tau_0$, where $\overline{l}^2$ is the mean-square hopping length. Taking the typical value for polymers $\overline{l}\simeq 30$ Å, we find $\mu\simeq 3\times10^{-5}$ cm$^2$/Vs, which is fairly close to the mobility obtained from independent experiments.

It is interesting that an increase in the electric field intensity at the sample caused narrowing of the resonant line and reduced its intensity, which indicates that the duration of contact between the carrier and the paramagnetic center is reduced (Fig. 2), which may be caused by an increase in the carrier hopping frequency as the electric field increases.

[1] E. L. Frankevich, I. A. Sokolik, D. I. Kaydrov *et al.*, JETP Lett. **36**, 486 (1982).
[2] E. L. Frankevich, Khim. Fiz. **2**, 1642 (1983).
[3] E. L. Frankevich *et al.*, Phys. Status Solidi **132**(1), 283 (1985).
[4] E. L. Frankevich, A. I. Pristupa, and V. M. Kobryanskiĭ, JETP Lett. **40**, 733 (1984).
[5] Ya. B. Zel'dovich, A. L. Buchachenko, and E. L. Frankevich, Usp. Fiz. Nauk. **155**, 3 (1988) [Sov. Phys. Usp. **31**, 385 (1988)].

Translated by R. M. Durham

# Diffusion of solvent across the surface of a resist film during centrifuging

V. I. Trigub and P. B. Boldyrevskiĭ

*Nizhniĭ Novgorod State Technical University*
(Submitted April 8, 1999)
Pis'ma Zh. Tekh. Fiz. **25**, 91–94 (December 12, 1999)

The influence of surface stresses induced by an external force on the diffusion of solvent across the surface of a resist film during centrifuging is investigated. The proposed model can be used to estimate the formation time of the resist film and the thickness of the protective coating. The theoretical estimates show fairly good agreement with the experimental results.
© *1999 American Institute of Physics.* [S1063-7850(99)01512-8]

When a resist is deposited on a substrate by centrifuging, solvent is removed from the film which causes the resist–air interface to be displaced. The resist drying process is analyzed by solving the problem of diffusion of the solvent component from the resist film into a vacuum-filled half-space. An expression for the normal component of the interface displacement velocity $V$ can be obtained by solving the hydrodynamic problem involving the rotation of a submerged disk at constant angular velocity $\Omega$ in a resist having the kinematic viscosity $\partial_R$, allowing for evaporation of the solvent during centrifuging[1]

$$V(\xi) = -\frac{2}{3}\sqrt{\Omega \partial_R}\,\xi^3, \tag{1}$$

where $\xi = \sqrt{\Omega/\partial_A}Z$ is a dimensionless variable, $\partial_A$ is the kinematic viscosity of air, and $Z$ is the coordinate axis perpendicular to the plane of the substrate. We shall consider the process taking place in the laminar regime. In addition, we also need to allow for compression of the film in one direction (along the $Z$ axis) with free expansion in the other two directions caused by the presence of the force density[2]: $Q = (dm/dt)u/S$, where $dm/dt = mCuS$ is the mass flow of the solvent, $m$ is the mass of the solvent molecules, $C$ is the molecular concentration, $u$ is the velocity of the solvent molecules, $S$ is the area of the film, and $t$ is the time.

We write the diffusion equation with initial and boundary conditions allowing for displacement of the resist–air interface

$$D\frac{d^2C}{dZ^2} - V(Z)\frac{dC}{dZ} = \frac{Q(Z)}{a} \tag{2}$$

subject to the conditions $C = C_0(Z=0)$ and $C = 0$ $(Z \to \infty)$, where $D$ is diffusion coefficient of the solvent vapor, $C_0$ is the saturated vapor concentration of the solvent, $Q(Z)$ is the external force acting on the resist film per unit area, $a = Wh$, $W = \sqrt{E/[3\rho_F(1-\mu^2)]}$, $\rho_F$ is the density of the resist surface film, $E$ and $\mu$ are Young's modulus and the Poisson ratio of the surface film material, and $h$ is the film thickness of the resist surface layer (not exceeding a few nanometers). For our estimates we assume that the solvent molecules can diffuse across the surface layer.[3]

The solution of Eq. (2) will be the function

$$C(Z) = C_0 - M^2\sqrt{\frac{\partial_A}{\Omega}}\int_0^Z \left[\exp\sqrt{\frac{\partial_A}{\Omega}}\int_0^\eta \frac{V(\Phi)}{D}d\Phi \int_0^\eta \frac{Q(\mu)\exp\sqrt{\partial_A/\Omega}\int_0^\mu (V(p)/D)dpd\mu}{Da}\right]d\eta, \tag{3}$$

$$M^2 = \frac{\sqrt{(\Omega/\partial_A)}C_0}{\displaystyle\int_0^\infty \left\{\exp\sqrt{\partial_A/\Omega}\int_0^\eta (V(\Phi)/D)d\Phi \int_0^\eta \left[Q(\mu)\exp\sqrt{\partial_A/\Omega}\int_0^\mu (V(p)/D)dpd\mu/Da\right]\right\}d\eta}.$$

The diffusion flux of solvent vapor per unit surface area is given by

$$j = \frac{D\rho_s\sqrt{\Omega^3/\partial_A}C_0 a}{\displaystyle\int_0^\infty \exp\sqrt{\partial_A/\Omega}\int_0^\xi (V(\Phi)/D)d\Phi \int_0^\xi Q(\mu)\exp\sqrt{\partial_A/\Omega}\int_0^\mu (V(p)/D)dpd\mu d\xi}. \tag{4}$$

 © 1999 American Institute of Physics

It is well known that the relationship between the stress and strain for a polymer under tension or compression is linear. In the present paper, we show that the cubic dependence for a resist is very well substantiated experimentally

$$Q(\xi)=\chi\,\xi^3, \tag{5}$$

where $\chi=(\rho_F RT)/M_F$, $R$ is the gas constant, $T$ is the absolute temperature, and $M_F$ is the average molecular mass of the polymer (resist).

We assume a statistical model of a polymer film in the definition of $\chi$.

On the basis of Eqs. (4) and (5), the rate of displacement of the air–photoresist interface caused by evaporation of the solvent may be written as

$$V=\frac{j}{\rho_S}\cong\frac{D\Omega^{3/2}C_0 a}{\chi\partial_A^{1/2}0.38}. \tag{6}$$

The thickness of the resist should be fixed by equating the viscous flow velocity (1) and the solvent evaporation rate (6). For a photoresist we need to introduce the correction factor $\rho_k/\rho_d$ which allows for the difference between the densities of the dry film and the photoresist solution, and also the content of dry residue in the photoresist $\beta_R$

$$l_0\cong\frac{\rho_R}{\rho_d}\beta_R\sqrt{\frac{4DC_0 a\partial_R}{\Omega^{1/2}\partial_A^{1/2}\chi}}. \tag{7}$$

We shall estimate the time $\tau_0$ for fixing the film thickness $l_0$. We shall assume that before $\tau_0$ the resist viscosity changes negligibly and then by integrating expression (1) between infinity and $l_0$ we obtain

$$\tau_0\cong 0.3\left(\frac{\partial_R^{1/2}\partial_A^{1/2}\chi}{\Omega^{5/2}DC_0 a}\right). \tag{8}$$

Using Eqs. (6), (7), and (8), we estimate the values of $\tau_0$, $V$, and $l_0$ for an FP-383 photoresist where dioxane is used as the solvent. In this case we have $C_0=0.17\,\mathrm{kg/m^3}$, $\chi=1\,\mathrm{J/m^3}$, $\partial_R=5.9\,\mathrm{cS}$, $\partial_A=0.13\,\mathrm{S}$, $a=1\times10^{-6}\,\mathrm{m^2/s}$, and $D=7\times10^{-6}\,\mathrm{m^2/s}$. For $\Omega=2.5\times10^3\,\mathrm{rpm}$, we obtain $V\cong0.3\,\mu\mathrm{m/min}$, $l_0\cong0.6\,\mu\mathrm{m}$, and $\tau\cong2\,\mathrm{min}$, which shows very good agreement with the experimental values $l_0\cong0.56\,\mu\mathrm{m}$ and $\tau\cong1.5\,\mathrm{min}$.

[1] V. G. Levich, *Physicochemical Hydrodynamics* [in Russian], Fizmatgiz, Moscow (1959), 450 pp.
[2] L. D. Landau and E. M. Lifshitz, *Mechanics*, 2nd ed. (Pergamon Press, Oxford, 1969; Nauka, Moscow, 1965, 203 pp.).
[3] V. I. Trigub and G. L. Gol'denberg, Izv. Vyssh. Uchebn. Zaved. Mater. Élektron. Tekh. No. 4, 41 (1998).

Translated by R. M. Durham

# Mechanisms for thermal stability of the electrophysical properties of overcompensated *n*-Si⟨*B*,*S*⟩

M. S. Yunusov, M. Karimov, and P. A. Khalikov

*Institute of Nuclear Physics, Uzbek Academy of Sciences, Tashkent*
(Submitted April 13, 1999)
Pis'ma Zh. Tekh. Fiz. **25**, 1–4 (December 26, 1999)

Thermal annealing was used to study silicon samples having different sulfur concentrations. It was established that the temperature at which the sulfur centers decay depends on the concentration of sulfur atoms $N_s$ in the overcompensated silicon. As the distance between the impurities ($N_s^{-1/3}$) decreases, the decay temperature increases. The effect can be attributed to characteristic features of the distribution of the compensating sulfur impurity atoms inside a region of fluctuation, formed in silicon during doping. © *1999 American Institute of Physics.* [S1063-7850(99)01612-2]

Numerous studies have been made of the thermal stability of impurity centers in doped silicon having deep energy levels.[1–8] However, the physical processes taking place in these materials have not yet been clarified. Lemke[1–3] used DLTS to study Au, Pt, Ir, and Rh impurity centers in *n*- and *p*-Si before and after repeated heat treatment, and showed that the observed concentrations of impurity centers in silicon decrease, or are converted into other centers at temperatures below 400 °C (in this case the concentrations of impurity centers are $N_{\text{im}} \simeq 10^{13}$–$10^{14}\,\text{cm}^{-3}$). In Refs. 4–8 the decay of impurity centers (Au, Pt, Ir, Rh, and S) having concentrations $N_{\text{im}} \simeq 10^{15}$–$10^{16}\,\text{cm}^{-3}$ was observed at temperatures above 600 °C.

The aim of the present study is to identify the influence of the concentration of sulfur centers on the thermal stability of the conductivity of overcompensated *n*-Si⟨*B*,*S*⟩.

Sulfur was chosen as the silicon impurity because first, sulfur impurities form donor centers in the upper half of the silicon band gap and second, sulfur has a high solubility ($\sim 3\times 10^{16}\,\text{cm}^{-3}$ at 1320 °C). These two factors allow us to obtain *n*-type silicon (overcompensated *n*-Si⟨*B*,*S*⟩) from *p*-type over a wide range of resistivity (between 1 and $10^5\,\Omega\cdot\text{cm}$). In this case, sulfur atoms are the principal dopant in *n*-Si⟨*B*,*S*⟩. By establishing the temperature $T_p$ at which the transition from *n*- to *p*-type conductivity takes place under heat treatment, we can determine the dependence of the concentration of sulfur centers on the stabilization temperature ($T_s = T_p$) for the material conductivity.

The starting material was Czochralski-grown *p*-type silicon with resistivity $\sim 45\,\Omega\cdot\text{cm}$ and dislocation density $\sim 2\times 10^4\,\text{cm}^{-2}$.

The silicon was doped with sulfur impurities by thermal diffusion in the range 1000–1300 °C for ~20 h in an open quartz ampoule followed by cooling at a rate of ~250 deg/min, when conversion from *p*- to *n*-type conductivity was observed.

We investigated isochronous annealing in *n*-Si ⟨*B*,*S*⟩ in the temperature range 300–900 °C for which the holding time at a particular annealing temperature was ~20 min. Ohmic contacts were prepared by diffusion of phosphorus prior to doping the silicon with sulfur. Standard methods of measuring the Hall coefficient were used to determine the concentration and type of silicon conductivity.[9]

Table I gives results of studying the variation of the concentration of sulfur centers in overcompensated silicon with the temperature $T_p$ for the transition from *n*- to *p*-type conductivity. It can be seen that as the sulfur atomic concentration increases, $T_p$ shifts toward higher temperatures. We take the view that this is caused by a nonuniform distribution of sulfur atoms in the bulk of the overcompensated silicon, i.e., these samples have different degrees of impurity fluctuation.

Repeated heat treatment (resulting in the formation of vacancies V and interstitial sulfur impurity atoms $S_i$)[1)] up to the total decay temperature $T_{\text{dec}}$ ($T_p \simeq T_{\text{dec}}$) leads to additional lattice strength: after a sulfur atom has migrated from a lattice site to an interstitial site, a previously elongated region (the radius of the sulfur atom is smaller than the radius of the silicon atom;[10] in this case the lattice situated in the region of fluctuation is elongated) becomes even more elongated. Then, the lattice strength is compensated by the interstitial atom $S_i$ and becomes concentrated inside the fluctuation region, i.e., the released V and $S_i$, migrating within the region have a fairly high probability of encountering each other. As a result, an $S_i$ enters a lattice site configuration or a new $[V+S_i]$ forms. Thus, in our view, as $N_s$ increases, $T_p$ shifts toward higher temperatures. The higher the impurity concentration in the region of fluctuation, the shorter the distance between the sulfur atoms ($N^{-1/3}$) and the larger the radius of action of the elastic forces, and as a result the thermal stability of the conductivity of the compensated silicon is enhanced [in this case $N^{-1/3} \simeq (0.94-2)\times 10^{-5}$ cm]. The proposed mechanism to explain the thermal stability of compensated silicon also confirms the results reported in Refs. 1–3. In these studies the distance between the impurity atoms is $N^{-1/3} < 4\times 10^{-4}$ cm.

The condition for efficiency of this mechanism is that the distance between impurities $N^{-1/3}$ should be smaller than

 © 1999 American Institute of Physics

TABLE I. Dependence of the conductivity stabilization temperature in $n$-Si$\langle B,S\rangle$ on the concentration of sulfur centers.

| Concentration of sulfur centers ($N_s$), $cm^{-3}$ | $6\times10^{14}$ | $1\times10^{15}$ | $6\times10^{15}$ | $2\times10^{16}$ |
|---|---|---|---|---|
| Conversion temperature ($T_p$), °C | 680 | 700 | 730 | 780 |

the distance of action of the elastic forces $R_{el}$, i.e., $N^{-1/3} < R_{el}$. As the temperature increases, all the sulfur atoms are simultaneously released from vacancies and the mechanism ceases to operate.

It should be noted that when analyzing the shift of the total decay temperature as a function of the impurity atom concentration, we allowed for dilatational charges, i.e., we assumed that in the bulk of the material the compressed and elongated regions (formed as a result of heat treatment to the total decay temperature) have opposite dilatational charges.

To sum up, as a result of this analysis we have proposed a mechanism to explain the dependence of the total decay temperature of sulfur centers on their concentration, which we attribute to the different degrees of fluctuation of the sulfur atoms: the larger the number of sulfur atoms in a region of fluctuation, the higher the probability of the decay product becoming fixed inside this region in the bulk of $n$-Si $\langle B,S\rangle$.

It is quite interesting to note that the temperature dependence of the annealing of the same center (in this case an A-center[11]) depends on the degree of order of the semiconductor (i.e., as the radiation dose accumulates). However, the radiation conditions in the experiment are such that alternative mechanisms may appear.[12]

[1)]Several types of impurity fluctuations occur in the bulk of the doped material. It was assumed that the sulfur centers begin to decay in a fluctuation where the distance between the sulfur atoms is greater than in other fluctuations.

[1] H. Lemka, Phys. Status Solidi A **92**, K139 (1985).
[2] H. Lemke, Phys. Status Solidi A **91**, 143 (1985).
[3] H. Lemke, Phys. Status Solidi A **101**, 193 (1987).
[4] A. Z. Badalov, Fiz. Tekh. Poluprovodn. **6**, 789 (1972) [Sov. Phys. Semicond. **6**, 685 (1972)].
[5] M. S. Yunusov and M. Karimov, Dokl. Akad. Nauk Uz. SSR. No. 8, 19 (1976).
[6] M. S. Yunusov, M. Karimov, A. A. Karimov, R. Kh. Kochkarov, and B. L. Oksengendle, Dokl. Akad. Nauk Uz. SSR. No. 3, 25 (1991).
[7] A. Lebedev, N. A. Sobolev, and B. M. Urunbaev, Fiz. Tekh. Poluprovodn. **15**, 1519 (1981) [Sov. Phys. Semicond. **15**, 880 (1981)].
[8] V. E. Kustov and N. A. Tripachko, *Decay of a Supersaturated Solid Solution of Platinum in Silicon in: Properties of Doped Semiconductor Materials* [in Russian], Nauka, Moscow (1990).
[9] T. M. Baleshta and J. D. Keys, Am. J. Phys. **36**, 23 (1968).
[10] S. S. Batsanov, *Electronegativity of Elements and Chemical Bonds* [in Russian], Siberian Branch of the Academy of Sciences of the USSR Press, Novosibirsk (1962), 196 pp.
[11] T. Tanaka and J. Inuishi, J. Phys. Soc. Jpn. **19**(2), 167 (1964).
[12] L. S. Smirnov, S. P. Solov'ev, V. F. Stas', and V. A. Kharchenko, *Doping of Semiconductors Using Nuclear Reactions* [in Russian], Nauka, Novosibirsk (1981), 181 pp.

Translated by R. M. Durham

# Probing of a random phase object by a focused spatially modulated laser beam. Integral scanning method

V. P. Ryabukho, A. A. Chausskiĭ, and A. E. Grinevich

*Institute of Problems in Precision Mechanics and Control, Russian Academy of Sciences, Saratov*
*Saratov State University*
(Submitted April 16, 1999)
Pis'ma Zh. Tekh. Fiz. **25**, 5–10 (December 26, 1999)

A telescope system incorporating an illuminating spatially modulated laser beam, a diffuser in the entry plane, and a random phase screen in the spatial frequency plane was used to analyze the formation of average-intensity interference fringes in the image plane of the diffuser. It is shown that the system can operate as a shift interferometer where the contrast of the fringes is independent of the diffuser characteristics. Analytic expressions are obtained for the contrast of the fringes as a function of the parameters of the screen and the illuminating beam and it is established that the statistical anisotropy of the screen influences the contrast of the fringes. © *1999 American Institute of Physics.* [S1063-7850(99)01712-7]

In Refs. 1–3 Ryabukho and Chausskiĭ established that the parameters of the phase inhomogeneities of an object satisfying the ''random phase screen'' model[4,5] can be determined using a spatially modulated laser probe beam focused onto the surface of the screen. In order to observe average-intensity interference fringes which carry information on the inhomogeneity parameters, these authors[1–3] suggested moving the object or the inhomogeneities relative to the probe beam. Equivalent averaging is performed by scanning the laser beam over the object. In the present paper we consider an alternative method of obtaining average-intensity fringes with both the object and the probe beam fixed. This method involves simultaneously probing the object with numerous identical focused spatially modulated laser beams (SMLBs) obtained using a primary auxiliary diffuser which functions as an irregular diffraction grating.

The optical system is shown schematically in Fig. 1. In the absence of the diffuser $S_1$ the object $S_2$ is illuminated by a focused SMLB and the object must be displaced in the transverse direction to observe the interference fringes.[1–3] The diffuser $S_1$ multiplies the SMLB, i.e., the diffraction field behind it is a set of SMLBs propagating in different directions and simultaneously probing the object $S_2$. As a result of uncorrelated addition in the image of the diffuser $S_1$, the diffraction patterns from these beams form average-intensity fringes.

The formation of the interference fringes in the image $S_1'$ can have another interpretation which is more convenient for a formal analysis. Since the diffuser $S_1$ is illuminated by two waves whose directions of propagation differ by the angle $\theta$, two identical speckle fields form behind it, propagating at the angle $\theta$ relative to each other.[6] In the rear focal plane of the lens $L_1$ the fields acquire the transverse shift $\rho_0 = \theta f = \lambda f/\Lambda$, where $\Lambda$ is the period of the fringes in the SMLB. As a result of this shift the speckle fields beyond the object $S_2$ also become partially decorrelated, and in the image plane where the shift of the fields again becomes zero, the contrast of the average-intensity fringes is reduced. Hence, the contrast of the fringes should be determined by the modulus of the normalized correlation function $B_{12}(\boldsymbol{\zeta}, \boldsymbol{\rho}_0)$ of the interfering fields $U_1(\boldsymbol{\zeta})$ and $U_2(\boldsymbol{\zeta})$ in the image plane:

$$V = V_0 \left| \frac{B_{12}(\boldsymbol{\zeta}, \boldsymbol{\rho}_0)}{B_{12}(\boldsymbol{\zeta}, \boldsymbol{\rho}_0 = 0)} \right|, \quad B_{12}(\boldsymbol{\zeta}, \boldsymbol{\rho}_0) = \langle U_1(\boldsymbol{\zeta}) U_2^*(\boldsymbol{\zeta}) \rangle, \tag{1}$$

where $V_0$ is the contrast of the fringes in the illuminating diffuser $S_1$ of the SMLB; the angular brackets denote a statistical averaging operation.

Let us assume that the diffuser $S_1$ and the object $S_2$ are random phase screens having the transmission functions $t_1(\mathbf{r})$ and $t_2(\boldsymbol{\rho})$. Then, using two successive Fourier transformations and assuming that the entire scattered field falls within the aperture of the lens, $U_1(\boldsymbol{\zeta})$ may be written as

$$U_1(\boldsymbol{\zeta}) = \int_{-\infty}^{\infty} \int_{-\infty}^{\infty} U_0(\mathbf{r}) \exp(i \mathbf{k}_1 \mathbf{r}) t_1(\boldsymbol{\rho}_1) \times \exp\left( i \frac{k}{f} \mathbf{r} \boldsymbol{\rho} \right) t_2(\boldsymbol{\rho}) \exp\left( i \frac{k}{f} \boldsymbol{\zeta} \boldsymbol{\rho} \right) d^2\mathbf{r} d^2\boldsymbol{\rho}, \tag{2}$$

where $U_0(\mathbf{r})$ is the complex amplitude of one of the waves in the SMLB and $\mathbf{k}_1$ is the wave vector of this wave. The expression for $U_2(\boldsymbol{\zeta})$ is similar, with the vector $\mathbf{k}_1$ replaced by $\mathbf{k}_2$, where $|\Delta \mathbf{k}_{12}| = |\mathbf{k}_1 - \mathbf{k}_2| = k 2 \sin(\theta/2)$.

Substituting Eq. (2) for $U_1(\boldsymbol{\zeta})$ and $U_2(\boldsymbol{\zeta})$ into Eq. (1), changing the order in which integration and averaging are carried out, and taking into account the independence of the random functions $t_1(\mathbf{r})$ and $t_2(\boldsymbol{\rho})$ yields the following expression for the correlation function of the complex amplitudes of the fields in the image plane:

 © 1999 American Institute of Physics

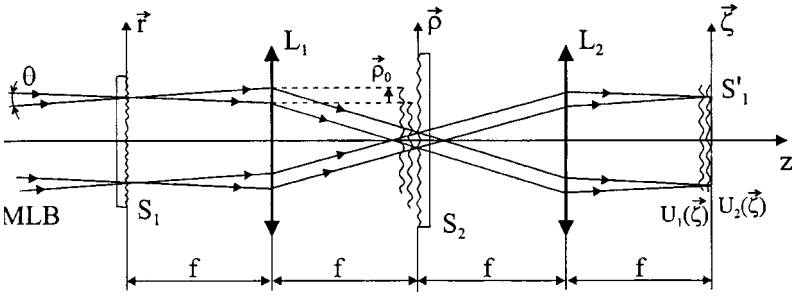


FIG. 1. Telescope measuring system with illuminating spatially modulated laser beam, diffuser in entry plane, and object being monitored in spatial frequency plane: SMLB — illuminating spatially modulated laser beam with parallel interference fringes, $L_1$ and $L_2$ — collimating lenses, $S_1$ — diffuser in front focal plane of the lens $L_1$, $S_2$ — object being monitored in rear focal plane of lens $L_1$, and $S_1'$ — image of diffuser $S_1$.

$$B_{12}(\boldsymbol{\zeta},\Delta\mathbf{k}_{12})=\int_{-\infty}^{\infty}\langle I_f(\boldsymbol{\rho})\rangle d^2\boldsymbol{\rho}\int_{-\infty}^{\infty}B_f \times\left(\Delta\rho+\frac{f}{k}\Delta\mathbf{k}_{12}\right)\mu_{t2}(\Delta\boldsymbol{\rho}) \times\exp\left(-i\frac{k}{f}\,\boldsymbol{\zeta}\,\Delta\boldsymbol{\rho}\right)d^2\Delta\boldsymbol{\rho}, \tag{3}$$

where $\langle I_f(\boldsymbol{\rho})\rangle=\int_{-\infty}^{\infty}\int_{-\infty}^{\infty}\mu_{t1}(\Delta\mathbf{r})\exp(i(k/f)\Delta\mathbf{r}\boldsymbol{\rho})d^2\Delta\mathbf{r}$ is the average intensity in the rear focal plane of the lens $L_1$ (the spatial spectrum of the diffuser $S_1$), the function $B_f(\Delta\boldsymbol{\rho})=\int_{-\infty}^{\infty}\int_{-\infty}^{\infty}I_0(\mathbf{r})\exp(i(k/f)\Delta\boldsymbol{\rho}\mathbf{r})d^2\mathbf{r}$ is the autocorrelation function of the field illuminating the object $S_2$, $I_0(\mathbf{r})=|U_0(\mathbf{r})|^2$ is the average intensity in the SMLB, and $\mu_{t1}(\Delta\mathbf{r})$ and $\mu_{t2}(\Delta\boldsymbol{\rho})$ are the normalized autocorrelation functions of the transmission coefficients $t_1(\mathbf{r})$ and $t_2(\boldsymbol{\rho})$ of the diffuser $S_1$ and the object $S_2$.

Substituting expression (3) into expression (1) shows that the contrast of the fringes does not depend on $\langle I_f(\boldsymbol{\rho})\rangle$ and $\mu_{t1}(\Delta\mathbf{r})$, i.e., it does not depend on the properties of the diffuser $S_1$.

For a fairly large-aperture illuminating SMLB for which the width of the function $B_f(\Delta\boldsymbol{\rho})$ is substantially less than the width of the function $\mu_{t_2}(\Delta\boldsymbol{\rho})$ so that $B_f(\Delta\boldsymbol{\rho})$ may be replaced by a $\delta$-function, the expression for the contrast of the fringes has the extremely simple form

$$V=V_0\mu_{t_2}\left(\boldsymbol{\rho_0}=\frac{f}{k}\Delta\mathbf{k}_{12}\right). \tag{4}$$

The contrast is determined by the normalized correlation function of the boundary field beyond the object as a function of the magnitude and direction of the relative shift $\rho_0$, i.e., the period $\Lambda$ and the orientation of the fringes in the SMLB. Thus, this system operates as a shift interferometer where the contrast of the fringes depends on the statistical anisotropy of the object.

For an arbitrary aperture $2W$ of the illuminating SMLB, an analytic expression for the fringe contrast can be obtained under the following assumptions: the intensity distribution $I_0(\mathbf{r})$ is Gaussian, $I_0(\mathbf{r})=I_0\exp(-2\mathbf{r}^2/W^2)$; the inhomogeneities of the object obey normal statistics, and their correlation coefficient $K_\phi(\Delta\boldsymbol{\rho})$ is Gaussian, $K_\phi(\Delta\boldsymbol{\rho})=\exp(-\Delta\boldsymbol{\rho}^2/l_\phi^2)$, where $l_\phi$ is the correlation length of the inhomogeneities. For $\mu_{t_2}(\Delta\boldsymbol{\rho})$ we can then use the approximation[2] $\mu_{t_2}(\Delta\boldsymbol{\rho})\approx(1-\exp(-\sigma_\phi^2))\exp(-\Delta\boldsymbol{\rho}^2/\rho_\perp^2)+\exp(-\sigma_\phi^2)$, where $\sigma_\phi^2$ is the dispersion of the phase fluctuations, and $\rho_\perp=l_\phi[-\ln\{\sigma_\phi^{-2}\ln[\exp(-1)(\exp(\sigma_\phi^2)-1)+1]\}]^{1/2}$ is the correlation length of the field beyond the object $S_2$ ($\rho_\perp\approx l_\phi$, for $\sigma_\phi\leqslant 1$, $\rho_\perp\approx l_\phi/\sigma_\phi$ for $\sigma_\phi>1$).

Using these approximations in expression (3) gives the following expression for the fringe contrast (1) in the paraxial region of the image $\boldsymbol{\zeta}=0$:

$$V=V_0\frac{\mu_0+(1-\mu_0)\rho_\perp^2(\rho_\perp^2+\rho_f^2)^{-1}\exp[-\boldsymbol{\rho}_0^2/(\rho_\perp^2+\rho_f^2)]}{\mu_0+(1-\mu_0)\rho_\perp^2(\rho_\perp^2+\rho_f^2)^{-1}}, \tag{5}$$

where $\mu_0=\exp(-\sigma_\phi^2)$ and $\rho_f=\sqrt{2}\lambda f/\pi W$ is the correlation length of the field illuminating the object $S_2$. Note that a similar expression for the fringe contrast is obtained using a single SMLB focused onto the surface of a moving object subject to the condition $\rho_f=\sqrt{2}w_0$, where $w_0$ is the radius of the constriction of the focused Gaussian beam. If the period

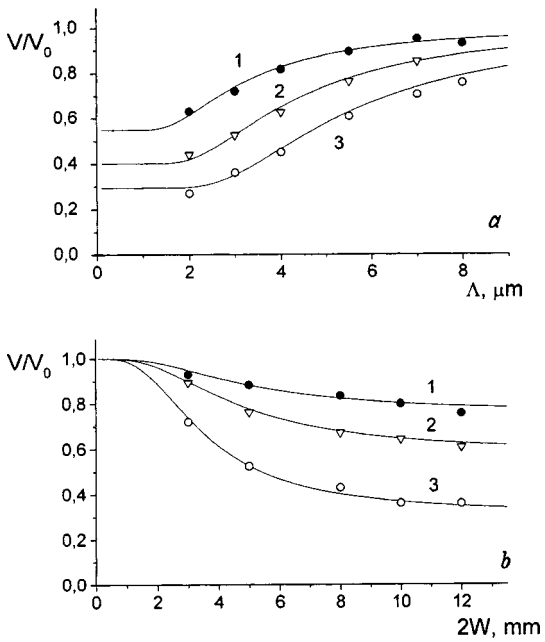


FIG. 2. Contrast of average-intensity interference fringes in image of diffuser: a — as a function of the fringe period $\Lambda$ in the illuminating beam for an object with $\sigma_\phi=1.15$ and $l_\phi=17\,\mu$m for various values of the beam aperture $2W$ and thus various correlation lengths of the object-probing field $\rho_f$ for $f=110$ mm. *1* — $2W=3$ mm, $\rho_f=20.8\,\mu$m; *2* — $2W=5$ mm, $\rho_f=12.5\,\mu$m; *3* — $2W=12$ mm, $\rho_f=5.2\,\mu$m; b — as a function of the beam aperture for various fringe periods: *1* — $\Lambda=8$ mm, *2* — $\Lambda=5.5$ mm, and *3* — $\Lambda=3$ mm.

$\Lambda$ of the fringes is fairly small, when $\rho_0^2 > \rho_\perp^2 + \rho_f^2$ the dependence of the fringe contrast on the statistical anisotropy of the object disappears.

The theoretical results agree fairly accurately with the experimental ones. Figure 2 gives the experimental points and theoretical curves obtained using expression (5) for the fringe contrast $V/V_0$ as a function of the fringe period $\Lambda$ and the aperture $2W$ of the illuminating SMLB.

The formation of an image of the interference fringes in the system shown in Fig. 1 can also be considered from the point of view of the classical analysis of linear optical systems.[5] However, the approach used here is clearer from the physical point of view and allows us to establish an analogy with the processes of formation of interference patterns in systems using a single probe SMLB.[1–3] It should also be noted that these results can be applied to optical imaging systems of a more general nature.

This work was supported by RFBR Grant No. 96-15-96389, under the Program ''Leading Scientific Schools in the Russian Federation.''

[1] V. P. Ryabukho and A. A. Chausskiĭ, Pis'ma Zh. Tekh. Fiz. **21**(16), 57 (1995) [Tech. Phys. Lett. **21**, 658 (1995)].
[2] V. P. Ryabukho and A. A. Chausskiĭ, Pis'ma Zh. Tekh. Fiz. **23**(19), 47 (1997) [Tech. Phys. Lett. **23**, 755 (1997)].
[3] V. P. Ryabukho and A. A. Chausskiĭ, Pis'ma Zh. Tekh. Fiz. **25**(1), 56 (1999) [Tech. Phys. Lett. **25**, 23 (1999)].
[4] S. M. Rytov, Yu. A. Kravtsov, and B. I. Tatarskiĭ, *Introduction to Statistical Radio Physics, Part 2, Random Fields* [in Russian], Nauka, Moscow (1978), 464 pp.
[5] J. W. Goodman, *Statistical Optics* (Wiley, New York, 1985; Mir, Moscow, 1988, 528 pp.).
[6] V. P. Ryabukho, Yu. A. Avetisyan, and A. B. Sumanova, Opt. Spektrosk. **79**, 299 (1995) [Opt. Spectrosc. **79**, 275 (1995)].

Translated by R. M. Durham

# Integrated-optics semiconductor detector using a prism coupling device

A. V. Khomchenko, E. V. Glazunov, I. U. Primak, V. P. Red'ko, and A. B. Sotskiĭ

*Institute of Applied Optics, Academy of Sciences of Belarus, Mogilev*
(Submitted January 12, 1999)
Pis'ma Zh. Tekh. Fiz. **25**, 11–17 (December 26, 1999)

A room-temperature integrated-optics semiconductor detector is proposed. The sensitive element of the detector is a thin film of antimony-activated tin dioxide deposited on a prism coupling element. The sensitivity of the structure to ammonia, alcohol vapor, and acetone impurities is investigated. The range of detectable ammonia concentrations is $10^{-4}$–$10^{-6}$%.
© *1999 American Institute of Physics.* [S1063-7850(99)01812-1]

Ceramic or thin-film sensors for gases and gas mixtures utilize the change in the electrical resistance of semiconductor materials caused by chemisorption and reverse catalysis or physical adsorption of the gas being detected.[1] In order to achieve efficiency together with the required sensitivity and selectivity, the operating temperatures of these devices vary between 100 and 500 °C (Refs. 2 and 3) and one of the main problems in the fabrication of these detectors is to obtain semiconducting layers whose properties exhibit good temperature stability.[3]

In the present paper we propose an integrated-optics semiconductor detector using antimony-activated tin dioxide and we investigate its properties. All the measurements were made at room temperature.

The sensitive element of the detector was a thin semiconducting film deposited on a prism coupling element. A schematic of this detector is shown as an inset to Fig. 1a. A prism coupling element comprising an isosceles glass prism serves as the substrate and is used to excite a waveguide mode in the semiconducting film. This film is separated from the prism by a buffer layer consisting of a silicon dioxide film. The buffer layer is used both to achieve the waveguide regime in the semiconducting film and to optimize the detector parameters. The sensitive element was fabricated by sputtering a ceramic target made from a mixture of tin oxide and between 2 and 15 wt.% antimony oxide. The films were deposited by rf sputtering in an argon and oxygen atmosphere. The thickness of the glass film varied in the range 0.2–1.0 $\mu$m and that of the sensitive element between 0.07 and 0.5 $\mu$m.

Light from a radiation source ($\lambda = 0.6328\,\mu$m) is coupled into the semiconducting film using the prism element and excites a waveguide mode whose complex propagation constant $h$ depends on the optical and geometric parameters of the buffer layer, the semiconducting film, and the properties of the ambient medium. When impurities of the gas being detected are present in the air, this changes the optical parameters of the semiconducting film (refractive index and absorption coefficient) which in turn changes the mode propagation constant. We used an optoelectronic recording unit consisting of an array of photodetectors and an analog-to-digital converter to record the spatial distribution of the reflected optical signal intensity and measure its change (Fig. 1a), from which we determined the real $h'$ and imaginary $h''$ parts of the mode propagation constant. The changes in the values of $h'$ and $h''$ were used as the measurable parameters of the detector sensitivity.

We investigated the properties of this structure as a function of the concentration of ammonia, alcohol vapor, and acetone in the ambient medium. The temperature (20 °C) and relative humidity (80%) in the volume being analyzed were kept constant in all cases. The results of investigating the sensitivity of the detector to impurities in a gas are plotted in Figs. 1a and 1b where $\Delta h''/h_0'' = (h'' - h_0'')/h_0''$, and $h''$ and $h_0''$ are the imaginary parts of the propagation constant of the waveguide mode in the presence of impurities and in air, respectively. Whereas the value of $h'$ changed negligibly over the entire range of concentrations, the values of $\Delta h''$ allow this to be used as a sensitivity parameter, so that this structure can be considered to be a gas impurity sensor.

The proposed structure exhibited the highest sensitivity to ammonia impurities, being able to record concentrations two or three orders of magnitude lower than other gases, i.e., this type of sensor has fairly high selectivity. The range of detectable concentrations was $10^{-4}$–$10^{-6}$ vol%. The sensitivity of the sensor and the range of detectable concentrations can be varied by varying the physical parameters of the thin-film structure. For instance, a reduction in the waveguide losses of the semiconductor film, i.e., in the value of $h_0''$, leads to an improvement in the sensor sensitivity (Fig. 2). Naturally, the range of detectable concentrations is then reduced. Similar results may be obtained by varying the parameters of the buffer layer.[4]

The time parameters of the sensor, i.e., the actuation and relaxation times, were investigated with a time resolution of 0.1 s. The actuation time was 6–9 s, and the initial parameters of the film were recovered completely over 15–20 s.

For comparison, we made similar electrical measurements where the measured parameter was the change in the specific conductivity of the films $\sigma$, measured by a four-probe method. Figure 2 (curve *4*) gives the dependence of $\Delta\sigma/\sigma_0 = (\sigma - \sigma_0)/\sigma_0$ on the ammonia concentration in air, where $\sigma$ is the conductivity of the film in the presence of impurities, and $\sigma_0$ is the conductivity in air. These measurements were again made at room temperature. In view of the lower sensitivity of the electrical parameters, the values of

 © 1999 American Institute of Physics

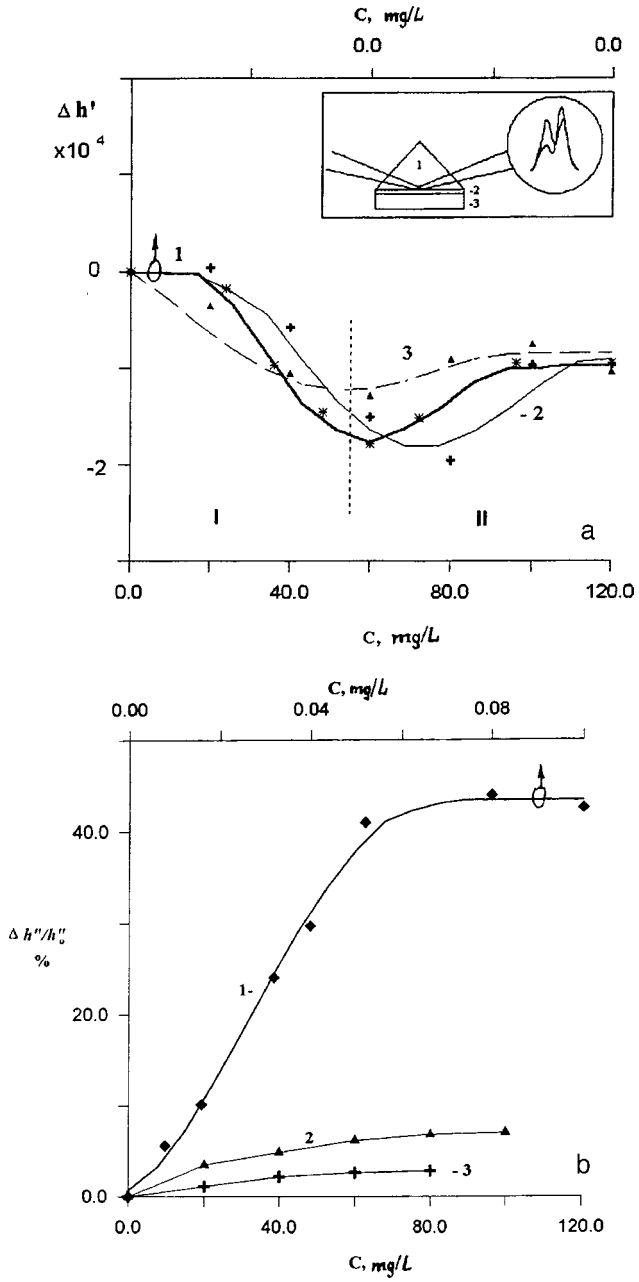


FIG. 1. Dependences of the real (a) and imaginary (b) parts of the propagation constant on the concentration of detected gas for ammonia (*1*), ethyl alcohol (*2*), and acetone (*3*); the inset shows the change in the detected signal and a schematic of the integrated-optics detector (*1* — prism, *2* — buffer layer, and *3* — semiconducting film.

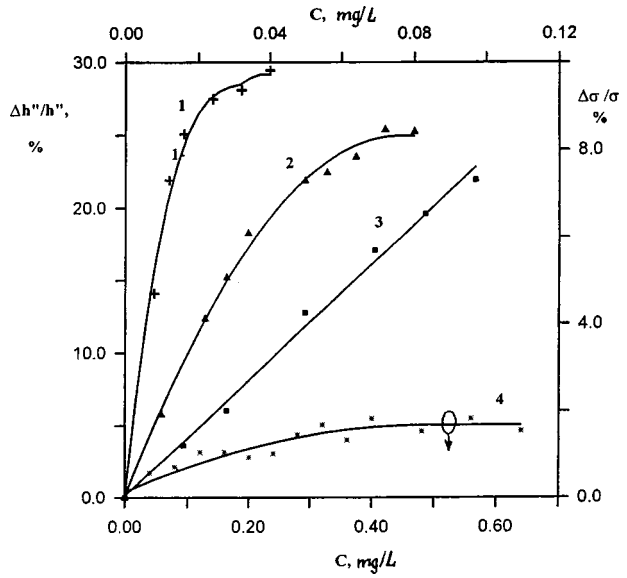


FIG. 2. Change in the detector sensitivity with decreasing waveguide losses in the semiconducting film: $h_0''=1.82\times10^{-4}$ (*1*), $h_0''=3.2\times10^{-4}$ (*2*), $h_0''=4.87\times10^{-4}$ (*3*); and conductivity (*4*) for this particular structure in ammonia.

the measured concentrations were slightly higher: between 0.02 and 6 mg/L. In this case, we also obtained a similar dependence of the sensitivity parameter on the gas impurity concentration.

This suggests an operating mechanism for the integrated-optics detector. In our opinion, this mechanism involves charge transfer from the energy levels of surface states created by adsorbed molecules to allowed energy bands. Under equilibrium conditions, because of the electrical neutrality of the entire structure, the electrical charge trapped by the surface states of the film is neutralized by the opposite charge in the surface region of the semiconducting film. When the semiconducting film is exposed to light, the concentration of free charge carriers increases and the unsaturated molecular bonds become unblocked. The appearance of excess carriers shifts the equilibrium between the charges in the surface states into the surface charge region, reducing the size of the latter. Under cw illumination, as in our case, a new quasiequilibrium carrier distribution is established in the space charge region. Charge exchange between surface states created by adsorbed gas molecules at unsaturated molecular bonds, and allowed energy levels is observed as a change in the absorption coefficient of the waveguiding semiconducting layer and causes a change in the imaginary part of the propagation constant of the waveguide mode $h''$, which was recorded experimentally.

In addition, the nonmonotonic dependence of the propagation constant on the impurity concentration indicates that there is another mechanism for the processes taking place in this structure. In our view, at low concentrations of gas impurities, adsorption taking place via a coordination mechanism plays a major role.[5] As a result of coordination-unsaturated centers being filled in the surface layer, $h''$ increases and $h'$ decreases. At high concentrations, a waveguide coupling mechanism predominates,[5] when the value of $h''$ reaches saturation (Fig. 1b) and $h'$ begins to increase

TABLE I. Results of estimating the thickness of the adsorbed layers and their influence on the parameters of the waveguide structure.

| | Ammonia | Alcohol | Acetone |
|---|---|---|---|
| $\varepsilon_{med}$ | 1.836033 | 1.84498 | 1.833386 |
| $d$, Å | 3.7 | 8.5 | 2.2 |
| $\Delta h'_{prop}$* | $1.0\times10^{-4}$ | $1.31\times10^{-4}$ | $3.9\times10^{-5}$ |

*The values of $\Delta h'_{prop}$ are given for interval II in Fig. 1a.

(Fig. 1a) which is most probably attributable to adsorption of a layer of gas molecules on the surface of the semiconducting film.

We can estimate the thickness of the adsorbed layers on the waveguide surface for the given dependence of $h'$ on the gas impurity concentration.[6] It should be borne in mind that the change in the mode propagation constant is influenced by the two mechanisms for variation in the permittivity of the waveguide structure indicated above. The influence of each mechanism can be separated by utilizing the fact that from a certain concentration of the gas impurities being analyzed, any further increase causes no appreciable changes in $h''$, and the change in the mode propagation constant is mainly influenced by the formation of the adsorbed layer.

In order to estimate the thickness of the adsorbed layers, we reconstructed the parameters of the waveguide structure used as the detector. The thickness and permittivity of the waveguide and buffer layers $d_f = 0.1\,\mu$m, $d_{\text{gap}} = 0.71\,\mu$m, $\varepsilon_f = 3.64086 - i \times 4.23 \times 10^{-3}$, and $\varepsilon_{\text{gap}} = 2.17976$ were determined from the measured values of the mode propagation constant when the detector was placed in various media such as air and water ($\varepsilon_a = 1.00$ and $\varepsilon_w = 1.69$, respectively). The permittivity of the prism is $\varepsilon_p = 3.74813$. Values of the permittivity of bulk materials were used as values for the adsorbed layers. The results of these estimates are presented in Table I and agree with the experimental data (Fig. 1a).

Thus, these results show that this structure may be used as a room-temperature gas impurity sensor.

This work was supported by the Belarus Republic Foundation for Basic Research.

[1] V. M. Arutyunyan, Mikroélektronika **20**, 337 (1991).
[2] G. Vigleb, *Detectors: Device and Applications* (Mir, Moscow, 1989, 190 pp.).
[3] V. A. Loginov, S. I. Rembeza, T. V. Svistova, and D. Yu. Shcherbakov, Pis'ma Zh. Tekh. Fiz. **24**(7), 57 (1998) [Tech. Phys. Lett. **24**, 270 (1998)].
[4] I. U. Primak, A. B. Sotskiĭ, and A. V. Khomchenko, Pis'ma Zh. Tekh. Fiz. **23**(3), 46 (1997) [Tech. Phys. Lett. **23**, 515 (1997)].
[5] V. F. Kiselev and O. V. Krylov, *Electronic Phenomena in Adsorption and Catalysis on Semiconductors and Dielectrics* [in Russian], Nauka, Moscow (1979), 232 pp.
[6] K. Tuefenthaler and W. Lukosz, J. Opt. Soc. Am. B **6**, 209 (1996).

Translated by R. M. Durham

# Beam model of waveguide regimes in a multilayer graded-index waveguide

D. G. Sannikov, D. I. Sementsov, A. M. Shutyĭ, and A. V. Kazakevich

*Ulyanovsk State University*
(Submitted September 24, 1998)
Pis'ma Zh. Tekh. Fiz. **25**, 18–23 (December 26, 1999)

Beam and wave approaches were used to obtain mode dispersion equations and to perform an analysis for a planar structure consisting of two waveguiding layers of which one is a graded-index layer. © *1999 American Institute of Physics.* [S1063-7850(99)01912-6]

Guided propagation of light in dielectric waveguides is frequently analyzed using a beam approach, which can be used to find a relationship between the propagation constant and the parameters of the waveguide structure and the radiation on the basis of clear concepts of geometric optics.[1] For waveguides having a stepped permittivity profile, the mode dispersion equations obtained by the beam and wave methods are the same for one[1] and several waveguide layers.[2,3] The beam approach is also applied to graded-index waveguides having one guiding layer, but the dispersion equations obtained do not agree analytically with those obtained by solving the boundary-value problem because of the approximate nature of the beam approach. In the present study we use both the beam and wave approaches to obtain dispersion equations, and make a comparative analysis for a waveguide structure having two guiding layers, of which one has a graded permittivity profile.

We shall consider a planar structure consisting of a semi-infinite covering medium of permittivity $\varepsilon_4$, a guiding cover layer of permittivity $\varepsilon_3$, and a guiding graded-index layer formed in the surface layer of the substrate and having the following permittivity profile:

$$\varepsilon_2(x)=\varepsilon_1+(\varepsilon_2-\varepsilon_1)\exp(-x/a). \tag{1}$$

Here $\varepsilon_2$ is the permittivity of the graded-index layer at the interface with the cover layer ($x=0$), $\varepsilon_1$ is the permittivity of the substrate ($x\gg a$), and $a$ is the characteristic thickness of the graded-index layer. All the values of $\varepsilon_1$ are taken to be real, which presupposes that no absorption takes place in these media. We postulate that $\varepsilon_4\leqslant\varepsilon_1<\varepsilon_2<\varepsilon_3$, which corresponds to real waveguide structures with a highly refracting coating.

Waveguide regimes in this structure are achieved as a result of total internal reflection of the wave at the boundary of the waveguiding layers. In the graded-index layer this reflection occurs at its interface with the cover layer, and at a caustic having the coordinate $x_c$ determined from the condition $\beta^2=k_0^2\varepsilon_2(x_c)$, where $\beta$ is the mode propagation constant, $k_0=2\pi/\lambda$, and $\lambda$ is the wavelength in vacuum. Two possible radiation channeling regimes in this structure are determined by the inequalities

$$\sqrt{\varepsilon_1}\,k_0\leqslant\beta\leqslant\sqrt{\varepsilon_2}\,k_0, \quad \sqrt{\varepsilon_2}\,k_0\leqslant\beta\leqslant\sqrt{\varepsilon_3}\,k_0. \tag{2}$$

The first regime corresponds to a zigzag mode propagating in the cover and graded-index layers and undergoing damping in the cover layer and the substrate at depth $x>x_c$. The second regime corresponds to a zigzag mode propagating only in the cover layer and undergoing damping in the covering medium and the graded-index layer.

In the beam approach, the mode dispersion equation is obtained from the transverse phase resonance condition[1] which for this particular structure may be given as follows:

$$2h_3L_3+\delta_{34}+\delta_{32}=2\nu\pi, \tag{3}$$

where $\nu$ is the number of the waveguide mode, $L_3$ is the thickness of the cover layer, $\delta_{34}$ is the phase shift of the wave undergoing total internal reflection at the cover layer–covering medium interface, and $\delta_{32}$ is the phase shift in the graded-index layer–covering medium system (first regime) or at the cover layer–graded-index layer interface (second regime). The value of $\delta_{34}$ is given by

$$\delta_{34}=-2\arctan(h_4/h_3\tau), \tag{4}$$

where $\tau=1$ and $\varepsilon_4/\varepsilon_3$ for the TE and TM modes, respectively. Here and subsequently, the transverse components of the wave vector in each layer are given by:

$$h_{1,4}^2=\beta^2-k_0^2\varepsilon_{1,4}, \quad h_{2,3}^2=k_0^2\varepsilon_{2,3}-\beta^2. \tag{5}$$

For the first channeling regime in accordance with Ref. 4, we have

$$\delta_{32}=-2\arctan[(1-r_{32})(1+r_{32})^{-1}\tan(\phi/2)], \tag{6}$$

where the phase shift of the wave as it propagates in the graded-index layer is

$$\phi=\delta_c+2\int_0^{x_c}(k_0^2\varepsilon_2(x)-\beta^2)^{1/2}dx, \tag{7}$$

and $\delta_c=\pi/2$ is the phase shift at the caustic in the graded-index layer,[1]

$$r_{32}=(\sigma h_3-h_2)(\sigma h_3+h_2)^{-1} \tag{8}$$

is the amplitude reflection coefficient at the interface between semi-infinite media having the parameters $\varepsilon_2$ and $\varepsilon_3$, and $\sigma=1$ and $\varepsilon_2/\varepsilon_3$ for the TE and TM modes, respectively. Using the expression for the caustic coordinate $x_c=2a\ln(\nu/w)$ and integrating in expression (7), we obtain:

$$\phi=4\nu(\sqrt{1-b}-\sqrt{b}\arccos\sqrt{1-b})+\pi/2, \tag{9}$$

 © 1999 American Institute of Physics

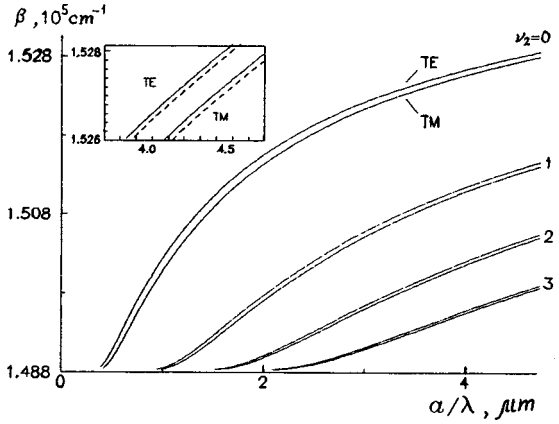


FIG. 1. Dispersion dependences for the first waveguide regime.

where we introduce the notation $v=ak_0(\varepsilon_2-\varepsilon_1)^{1/2}$, $w=ah_1$, and $b=(w/v)^2$. Substituting these expressions into Eq. (3), we write the dispersion equation for the first waveguide regime:

$$\tan(\phi/2)=(\sigma h_3/h_2)\tan[L_3h_3-\arctan(h_4/\tau h_3)]. \quad (10)$$

Under the conditions of the second waveguide regime, $h_2$ becomes imaginary and the wave is damped in the graded-index layer at depth $x\simeq\lambda/2\pi$ (Ref. 4). Total internal reflection takes place at the interface between the graded-index layer and the cover layer and this is responsible for the absence of a caustic so that $\delta_c=0$. As a result, the dispersion equation for this case has the form:

$$\tanh(\tilde{\phi}/2)=(\sigma h_3/\tilde{h}_2)\tan[-L_3h_3+\arctan(h_4/\tau h_3)], \quad (11)$$

where $\tilde{h}_2=(\beta^2-k_0^2\varepsilon_2)^{1/2}$ and $\tilde{\phi}=4v(\sqrt{b-1}-\sqrt{b}\times\arctan\sqrt{(b-1)/b})$.

We also obtained the dispersion equation for this waveguide structure using the wave approach, which gives:

$$J_{2w}(2v)ah_3(h_2\tau-h_3\tan h_3L_3)+J'_{2w}(2v)v\sigma\times(h_2\tau-\tan h_3L_3+h_3)=0, \quad (12)$$

where $J_{2w}$ and $J'_{2w}$ are the $2w$th order Bessel function and its derivative.[5] In order to obtain an explicit analytic difference between the dispersions equations (10) and (11) on the one hand and (12) on the other, we need to make a comparative analysis of their results.

For this purpose we take the parameters corresponding to a real waveguide structure consisting of an ion-exchanged $Ag^+$ waveguide with a semiconducting coating of chalcogenide glassy semiconductor:[5] $\varepsilon_1=2.04$, $\varepsilon_2=2.31$, $\varepsilon_3=6.15$, and $\varepsilon_4=1.00$ (at $\lambda=0.6328\,\mu$m). An analysis of these dispersion equations shows that their solutions are generally determined by a set of mode numbers $\nu=\nu_2+\nu_3$, where $\nu_2$ corresponds to an integer number of energy maxima of the mode field in the graded-index layer, and $\nu_3$ corresponds to that in the cover layer. Thus, the mode numbers $\nu_2$ and $\nu_3$ determine the distribution of the mode field with a given number $\nu$ which corresponds to the total number of energy minima in the waveguide structure. The phase shift of the mode in the cover layer in conveniently expressed in the form $L_3h_3=(\nu+\alpha)\pi$, where the parameter $\alpha$ has values between zero and one. We introduce the thickness $L_h=\pi/h_3$, which is generally a function of the propagation constant $\beta$. If $\varepsilon_2-\varepsilon_1\ll\varepsilon_1$, and $\varepsilon_3$ is considerably greater than $\varepsilon_1$ and $\varepsilon_2$ (highly refracting coating), the value of $L_h$ can be considered to be constant. In this case we have $L_3=(\nu+\alpha)L_h$, and $L_h$ is the characteristic period for the thickness of the cover layer.

Figure 1 gives dependences of the propagation constant $\beta$ on the normalized thickness of the graded-index layer $a/\lambda$ obtained for the first radiation channeling regime using Eqs. (10) and (12) for the first four $\nu_2=0,\ldots,3$; $\nu_3=1$) TE and TM modes and the parameters $L_3=L_h=0.158\,\mu$m and $\alpha=0$. To within graphical error, both dispersion equations give the same dependences $\beta(a/\lambda)$. The inset shows part of the dispersion curves for the $\nu_2=0$ mode on a larger scale, obtained using the beam and wave approaches (solid and dashed curves). The largest difference between the solutions of the dispersion equations (10) and (12) $\Delta\beta/\beta$, where $\Delta\beta=|\beta_{\text{wave}}-\beta_{\text{beam}}|$, for the selected parameters does not exceed $2\times10^{-4}$. The dispersion dependences for the second waveguide regime are higher than $\beta=2\pi\sqrt{\varepsilon_2}/\lambda=1.55\times10^5\,\text{cm}^{-1}$ and are not shown in the figure.

Figure 2 gives dependences of the propagation constant $\beta$ on the normalized thickness of the cover layer $L_3/L_h$ for three ($\nu=2,6,10$) TE and TM modes for the parameter $a=3.87\,\mu$m. The lower steps on each curve correspond to $\nu_3=0$. On transition from one step to the next step up, $\nu_3$ increases and $\nu_2$ decreases by one. These dependences $\beta(a/\lambda)$ are plotted for the beam and wave approaches and agree to within graphical error.

To conclude, we note that this method of obtaining the dispersion equation in the beam approximation is valid not only for an exponential profile but for any graded-index profile $\varepsilon_2(x)$ in this particular waveguide structure.

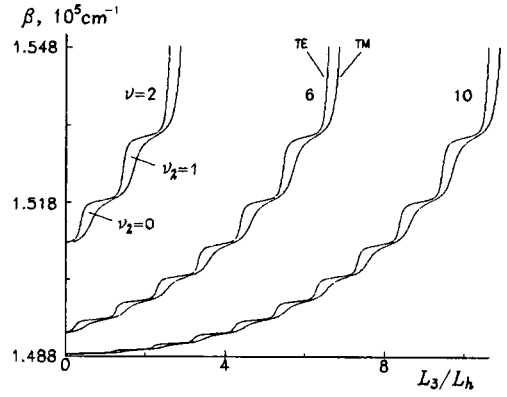


FIG. 2. Dependences of the propagation constant on the thickness of the cover layer.

[1] M. Adams, *An Introduction to Optical Waveguides* (Wiley, New York, 1981; Mir, Moscow, 1984, 512 pp.).
[2] Yu. P. Udoev, Opt. Spektrosk. **65**, 1327 (1988) [Opt. Spectrosc. **65**, 784 (1988)].
[3] P. V. Adamson, Opt. Spektrosk. **70**(1), 211 (1991) [Opt. Spectrosc. **70**, 121 (1991)].

[4] M. Born and E. Wolf, *Principles of Optics*, 4th ed. (Pergamon Press, Oxford, 1969; Nauka, Moscow, 1973, 856 pp.).
[5] *Handbook of Mathematical Functions*, edited by M. Abramowitz and I. A. Stegun (Dover, New York, 1965; Nauka, Moscow 1979, 839 pp.).
[6] N. F. Mott and E. A. Davis, *Electronic Processes in Non-Crystalline Materials* (Clarendon Press, Oxford, 1971; Nauka, Moscow, 1982, 658 pp.).

Translated by R. M. Durham

# Influence of acoustic treatment on the photoconductivity of zinc selenide crystals

I. A. Klimenko and V. P. Migal'

*N. E. Zhulovsky State Aerospace University, Kharkov*
(Submitted February 3, 1999)
Pis'ma Zh. Tekh. Fiz. **25**, 24–29 (December 26, 1999)

It is shown that acoustic treatment of piezoelectric zinc selenide crystals by exciting strong natural elastic vibrations can specifically alter their photoelectric and other properties. Irreversible changes in the stressed-strained state of the crystals under this treatment are responsible for characteristic features in the spectral dependences of the permittivity $\varepsilon'(\lambda)$ and the dielectric loss coefficient $\varepsilon''(\lambda)$. These dependences plotted in the form of $\varepsilon^*(\lambda)$ diagrams on the complex plane and also the spectrum of natural elastic vibrations can be used to monitor the treatment process. © *1999 American Institute of Physics.* [S1063-7850(99)02012-1]

Bulk piezoelectric crystals of zinc selenide grown from a flux are characterized by a wide range of structural defects, i.e., strain carriers and growth inhomogeneities, which form a complex stressed-strained state in these crystals. This state strongly influences their optical, photoelectric, and other properties. In particular, it is responsible for the individual nature of the low-frequency spectrum of elastic natural vibrations[1,2] and also for the difference between the spectral and temperature dependences of the permittivity $\varepsilon'$ and the dielectric loss coefficient $\varepsilon''$. Thus, a representation of these dependences in the form of $\varepsilon^*(\lambda)$ and $\varepsilon^*(T)$ diagrams on the complex plane reflects the self-consistent changes in the electric and elastic fields of the crystal under external influences.[3,4] Note that the irreversible changes in these spatially nonuniform fields in zinc selenide are difficult to reduce substantially by heat treatment. In the present paper we show that an effective method of changing the complex stressed-strained state of piezoelectric crystals involves treating these with a strong alternating electric field at frequencies of specific natural elastic vibrations which can specifically alter the photoelectric, dielectric, and other properties.

We investigated oriented samples in the form of rectangular parallelepipeds (having sides of $10\times8\times8$ mm and $12\times12\times11$ mm), fabricated from crystal ingots up to 50 mm in diameter. These were grown from a flux by the Bridgman method under argon pressure. After chemical-mechanical polishing, indium–gallium Ohmic contacts were deposited on opposite faces. The acoustic treatment was carried out by exciting natural elastic vibrations in the samples using an alternating electric field of strength 100–800 V/cm. The treatment involved systematically exciting between one and five low-frequency natural elastic vibrations. The duration of the acoustic treatment was determined from the rate of decrease in the intensity of the light during the treatment process after this had been passed through a polarizer–crystal–analyzer system. Torsional vibrations were excited using four electrodes, for which a quadrupole electric field was created in the sample. Topograms of the vibrations were visualized by an optical-polarization method. The presence of optical inhomogeneities in the samples was identified by a direct shadow method (luminous point method). The dielectric parameters were determined using an ac bridge at 1 kHz.

For the investigations we selected two groups of samples. The first group was formed by optically more perfect crystals whose absorption coefficient at 10.6 $\mu$m is better than $3.3\times10^{-3}$ cm$^{-1}$. The permittivity of the samples measured at 1 kHz is in the range 9.1–9.4 and is almost independent of the crystallographic direction. Their spectrum of natural elastic vibrations contains various strong vibrations whose number predominates over the secondary vibrations. In the second group of samples we identified numerous optical inhomogeneities created by two-dimensional structural defects (rotation twins, glide bands, twinning lamellae, and so on). These create bands of alternating birefringence which are randomly distributed in the [111] direction. In this direction the permittivity has the lowest values (10.4–11.4) whereas in other directions its values are in the range 12–18. In addition, the method of etch figures revealed layers containing a substructure in these samples. The spectrum of natural elastic vibrations has a complex structure of secondary resonances whose number and distribution over the spectrum are individual characteristics of the sample.[2] Characteristic features of the three-dimensional image of the shadow pattern of the samples (the ''deformation'' of the image of the sample surfaces, and so on) are shown in the insets to Figs. 1 and 2. These indicate the complexity of the processes accompanying the growth of plastic deformation. Note that in the shadow pattern of the more deformed samples in the second group we can seen ''traces'' of plastic rotations. A blurred image of the sample surfaces indicates macroscopic fluctuations of the refractive index (see inset to Fig. 2).

For the first group of samples, the most effective treatment involved systematically exciting between three and five of the strongest low-frequency natural vibrations using a strong alternating electric field. Figure 1 shows typical $\varepsilon^*(\lambda)$ diagrams for this group of samples before and after acoustic treatment (solid and dashed curves) plotted using the spectral dependences $\varepsilon'(\lambda)$ and $\varepsilon''(\lambda)$. We can see that after treatment, the permittivity increment to light decreases, which reduces the area enclosed by the curve $\varepsilon^*(\lambda)$. Note that similar changes in the diagrams were also identified for other directions of the external field.

 © 1999 American Institute of Physics

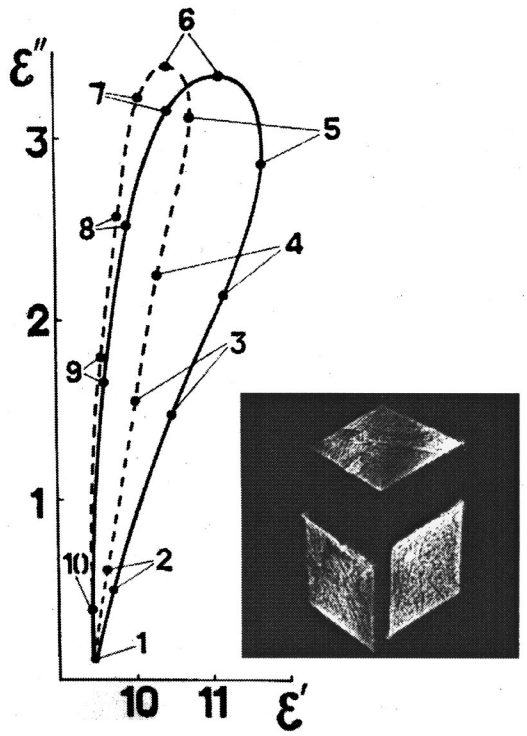


FIG. 1. Diagrams of $\varepsilon^*(\lambda)$ for zinc selenide ($E$ parallel to [111], $T=293$ K): *1* — 0.450, *2* — 0.475, *3* — 0.480, *4* — 0.490, *5* — 0.500, *6* — 0.510, *7* — 0.525, *8* — 0.550, *9* — 0.580, and *10* — 0.600 $\mu$m.

The efficiency of the acoustic treatment of samples in the second group depends strongly on the crystallographic orientation of the sample, the type of elastic vibrations excited, and the external electric field strength. The efficiency may decrease or increase the dielectric parameters, the absorption coefficient at 10.6 $\mu$m and other parameters, which confirms its close correlation with the stressed-strained state of the crystal. The most significant irreversible changes in the spectra $\varepsilon'(\lambda)$ and $\varepsilon''(\lambda)$ were identified after treating the samples using a quadrupole alternating electric field at the frequency of the torsional natural vibrations when the external electric field is perpendicular to the [111] direction. A comparison between the $\varepsilon^*(\lambda)$ diagrams obtained before and after acoustic treatment (solid and dashed curves in Fig. 2) shows that after treatment the range of variation of $\varepsilon'$ and $\varepsilon''$ under photoexcitation from the 0.47–0.62 $\mu$m range was almost doubled and the area enclosed by the curve on the $\varepsilon^*(\lambda)$ diagram was almost quadrupled. The photosensitivity in the infrared also dropped significantly. The change in the diagrams after acoustic treatment indicates that the relaxation processes undergo rearrangement. Under strong torsional vibrations the internal elastic and electric fields created mainly by two-dimensional structural defects undergo self-consistent changes in the crystals. This is confirmed by: a) a reduction in the local birefringence in some birefingence bands, b) a reduction in the dielectric loss coefficient, and c) the increased symmetry of the optical-polarization topograms and equalization of the contrast of the nodal lines on these topograms which indicates that the homogeneity of the samples is improved. Note also that after treatment the number of secondary resonances in the natural vibration spectrum decreased. The high efficiency of the acoustic treatment of cubic zinc selenide crystals in a quadrupole electric field may be explained by the fact that the [111] direction perpendicular to the twinning and glide planes is selected.

The strong influence of the acoustic treatment of the crystals on nonequilibrium carrier transfer processes and charge transfer between complex centers confirms the important role played by the elastic fields of structural defects in the formation of photoelectric, dielectric, and other properties. We also note that unlike the treatment of crystals in a traveling ultrasonic wave field,[5] the possibility of exciting various types of natural vibrations in samples means that the stressed-strained state of the crystal can be specifically and selectively altered. The $\varepsilon^*(\lambda)$ diagrams and the optical polarization topograms as well as the spectrum of natural elastic vibrations can be used to effectively monitor the treatment process. This method of treatment is particularly promising for materials grown under extreme conditions since other methods of treatment are ineffective for these.

The authors thank the Fund for Basic Research of the

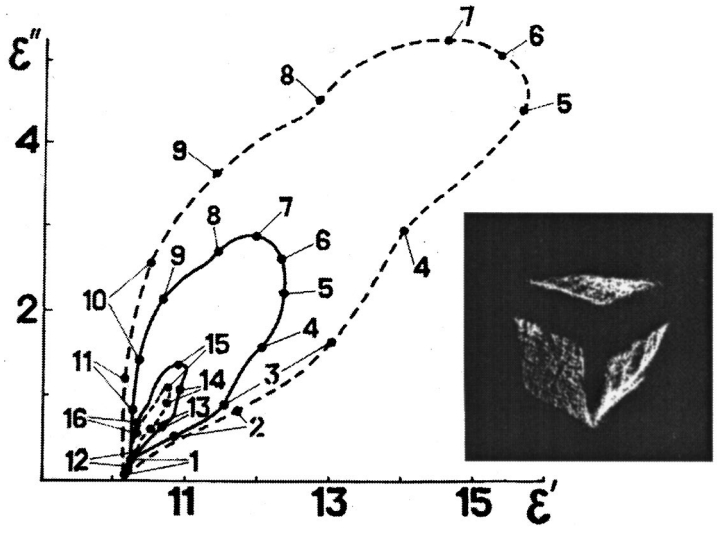


FIG. 2. Diagrams of $\varepsilon^*(\lambda)$ for zinc selenide ($E$ parallel to [111], $T=293$ K): *1* — 0.450, *2* — 0.475, *3* — 0.480, *4* — 0.490, *5* — 0.500, *6* — 0.510, *7* — 0.525, *8* — 0.550, *9* — 0.580, *10* — 0.600, *11* — 0.650, *12* — 0.700, *13* — 0.800, *14* — 0.900, *15* — 1.000, and *16* — 1.200 $\mu$m.

Ministry of Science of the Ukraine for financially supporting this work.

[1] V. K. Komar', V. P. Migal', V. A. Kornienko *et al.*, Pis'ma Zh. Tekh. Fiz. **20**(10), 71 (1994) [Tech. Phys. Lett. **20**, 419 (1994)].
[2] V. K. Komar', V. P. Migal', and O. N. Chugaĭ, Neorg. Mater. **34**, 800 (1998).
[3] Yu. A. Zagoruĭko, V. K. Komar', V. P. Migal' *et al.*, Fiz. Tekh. Poluprovodn. **29**, 1065 (1995) [Semiconductors **29**, 552 (1995)].
[4] Yu. A. Zagoruĭko, V. K. Komar', V. P. Migal' *et al.*, Fiz. Tekh. Poluprovodn. **30**, 1046 (1996) [Semiconductors **30**, 556 (1996)].
[5] I. V. Ostrovskiĭ and V. N. Lysenko, Fiz. Tverd. Tela (Leningrad) **24**, 1206 (1982) [Sov. Phys. Solid State **24**, 682 (1982)].

Translated by R. M. Durham

# Hysteresis and metastability of the transition from evaporative to droplet flow of a liquid through a capillary

A. V. Melkikh and V. D. Seleznev

*Urals State Technical University, Ekaterinburg*
(Submitted December 10, 1998; resubmitted April 22, 1999)
Pis'ma Zh. Tekh. Fiz. **25**, 30–36 (December 26, 1999)

A model is constructed for the transition from evaporative to droplet flow of a liquid through a capillary in a gravitational field allowing for the mutual influence of the droplets. An *S*-shaped dependence of the flow on the pressure drop at the capillary is obtained which for certain (critical) values of the control parameter gives a monotonic curve. Values of the pressure drop are determined for which the droplet flow regime and the droplet-free regime become unstable. It is shown that in a certain range of pressure drops in the presence of noise transitions may take place from evaporative to droplet flow and back (intermittence). © *1999 American Institute of Physics.* [S1063-7850(99)02112-6]

The phenomenon of the transition to droplet flow of a liquid in a capillary is used in various devices and technological processes, including inkjet printing, liquid dosing in chemical technology, in medical technology, and so on. The transition to droplet flow has been studied experimentally[1–3] and theoretically. Equations describing capillary surfaces for different types of droplet in a gravitational field have been examined in the literature and a linear analysis has also been made of the stability of a suspended droplet.[4,5] However, when the droplet has already formed, the droplets may influence each other, which may lead to nonlinear effects. The present paper is devoted to modeling the transition from evaporative to droplet flow allowing for the mutual influence of the droplets.

We shall consider a thin-walled vertical capillary containing a liquid. We shall denote by $\Delta p_{S0}$ the pressure drop of the liquid in the capillary for which a suspended droplet becomes unstable with respect to detachment from the capillary. The value of $\Delta p_{S0}$ can be approximately obtained using the formula

$$\Delta p_{S0}=\frac{2\sigma}{r}, \tag{1}$$

where $\sigma$ is the surface tension and $r$ is the capillary radius.

Quite clearly, after the droplet has fallen, the liquid surface at the end of the capillary does not immediately become equilibrium. We shall take $\tau$ to denote the pressure relaxation time at the free surface and $\omega_0$ to denote the frequency of the ensuing surface oscillations.

Clearly defined oscillations of the liquid surface at the end of the capillary will occur if

$$\tau \gg \omega_0^{-1}. \tag{2}$$

For $\tau \ll \omega_0^{-1}$ the initial perturbation decays monotonically. The values of $\tau$ and $\omega_0$ may be calculated similarly:[6]

$$\omega_0=\sqrt{\frac{8\sigma}{\rho r^3}}, \quad \tau=\frac{\rho r^2}{8\eta}, \tag{3}$$

where $\eta$ is the dynamic viscosity. An estimate of these values using the formulas (3) shows that for water for example ($r' \sim 0.25$ mm) at room temperature, condition (2) is reliably satisfied.

The third characteristic time for this problem is the reciprocal dripping frequency $J^{-1}$.

If the perturbation relaxation time $\tau$ becomes comparable with the dripping period $J^{-1}$, the stability conditions will differ for the first and subsequent droplets.

We shall make a more detailed study of the case when the liquid surface undergoes oscillations. The amplitude of these oscillations decays exponentially:

$$\Delta x=\Delta x_0 \exp\left(-\frac{t}{\tau}\right),$$

where $\Delta x_0$ is the initial perturbation.

At the instant when the droplet has become detached, the liquid surface is elongated by the force mg where m is the droplet mass. The amplitude of the residual pressure $p_1$ (as a result of the deformation of the surface after detachment of the droplet) will then decay with time as given by

$$p_1=\xi \rho g r \exp\left(-\frac{t}{\tau}\right),$$

where $\rho$ is the liquid density and $\xi$ is a dimensionless coefficient of the order of unity.

Quite clearly, the next droplet will occur under conditions different from the first. This difference will be that the residual pressure will allow the droplet to fall when $\Delta p < \Delta p_{S0}$.

In this case, the stability condition (1) is transformed to give:

$$\Delta p_S=\frac{2\sigma}{r}-\xi \rho g r \exp\left(-\frac{1}{J\tau}\right). \tag{4}$$

 © 1999 American Institute of Physics

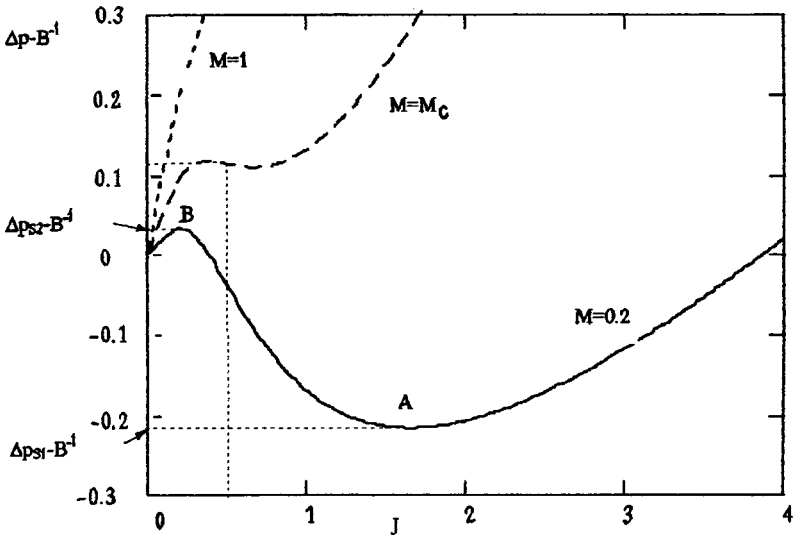


FIG. 1.

When the pressure difference at the capillary exceeds $\Delta p_S$ (4), this causes hydrodynamic transport of the liquid through the channel. The resulting flow velocity can then be estimated using the Poiseuille formula:

$$u=-\frac{\pi r^2}{8\eta L}(\Delta p-\Delta p_S), \tag{5}$$

where $\eta$ is the dynamic viscosity of the liquid and $L$ is the length of the capillary.

By averaging formula (5) over time over the period of droplet occurrence, we can easily derive an expression for the dripping frequency:

$$J=\frac{\rho\pi r^4}{8\eta L m}(\Delta p-\Delta p_S)=\frac{3r}{32\eta L}(\Delta p-\Delta p_S), \tag{6}$$

where $m=4\pi\rho\gamma r^3/3$ is the droplet mass, and $\gamma$ is a coefficient which allows for the difference between the droplet and capillary diameters.[2]

Expressions (6) and (4) then yield the expression for the dripping frequency:

$$\frac{32\eta\gamma L}{3r}J=\Delta p-\frac{2\sigma}{r}+\xi\rho g r\exp\left(-\frac{1}{J\tau}\right).$$

It is convenient to introduce the dimensionless pressure difference and dripping frequency:

$$\Delta p'=\frac{\Delta p}{\xi\rho g r}\quad\text{and}\quad J'=J\tau;$$

and omitting the primes we then obtain:

$$\frac{32\eta\gamma L}{3r^2\xi\rho g\tau}J=\Delta p-\frac{2\sigma}{\rho g r^2\xi}+\exp\left(-\frac{1}{J}\right),$$

$$MJ=\Delta\rho-B^{-1}+\exp\left(-\frac{1}{J}\right), \tag{7}$$

where $B=(\rho g r^2\xi/2\sigma)$ is the Bond number which characterizes the ratio of the gravitational forces to the surface tension forces and $M=(32\eta\gamma L/3r^2\xi\rho g\tau)$ is some dimensionless parameter which characterizes the ratio of the viscosity forces to the gravitational forces.

Graphs of $J$ as a function of $\Delta\rho$ are plotted in Fig. 1 for various values of $M$.

The curve is *S*-shaped. At points $A$ and $B$ the regime changes. For $M>M_c$ the curve is monotonic and the hysteresis disappears. From Eq. (7) by differentiating $\Delta p(J)$:

$$\frac{\partial\Delta p}{\partial J}=M-\frac{1}{J^2}\exp\left(-\frac{1}{J}\right)=0 \tag{8}$$

we can easily find the coordinates of points $A$ and $B$. These coordinates will correspond to a loss of stability by the system.

Equation (8) can either have two solutions or none at all. The stability boundary of the droplet [condition (1)] is assumed to be given. Both solutions correspond to the stability boundaries of the droplet regimes, i.e., ''fast'' and ''slow.'' In fact, if the droplets influence each other and can fall when $\Delta p<B^{-1}$, the flux cannot be infinitely small since the mutual influence of the droplets disappears in this case. That is to say, the transition from the droplet regime to the absence of droplets in the region $\Delta p_{S1}<\Delta p<B^{-1}$ should take place abruptly.

Equating the second derivative to zero

$$\frac{\partial^2\Delta p}{\partial J^2}=\exp\left(-\frac{1}{J}\right)\left[\frac{2}{J^3}-\frac{1}{J^4}\right]=0$$

and using equality (7), we obtain the parameters of the system at the critical point:

$$J_c=\frac{1}{2},\quad M_c=4e^{-2},\quad \Delta p_c=e^{-2}+B^{-1}.$$

If $M>4e^{-2}$ (for example, if the viscosity is high or the channel is long), hysteresis cannot occur in the system and the transition from droplet to evaporative flow (in Fig. 1 the line $J=0$ for $\Delta p<B^{-1}$) and back will take place continu-

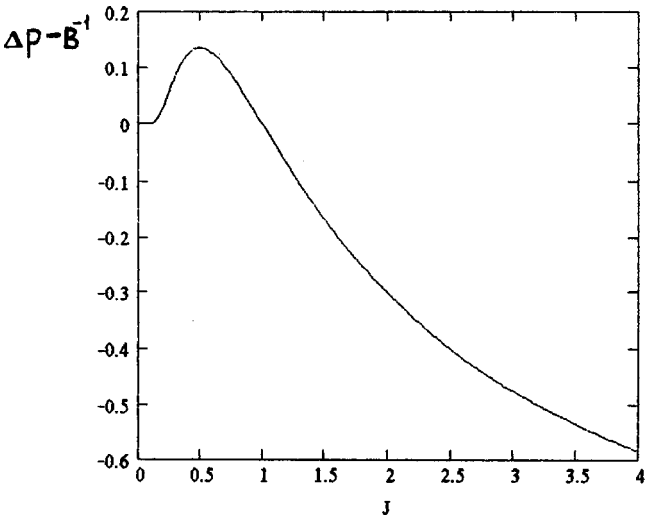


FIG. 2.

ously (without a jump). In this case, the droplets have little influence on each other (see, for example, Ref. 1).

If $M<4e^{-2}$, hysteresis may be observed in the system: if the pressure drop increases from the point $\Delta p<\Delta p_{S1}$, the system abruptly goes over to the upper branch of the curve $J(\Delta p)$, whereas if the system moves in the opposite direction from the point $\Delta p>\Delta p_{S2}$, at the point $\Delta p_{S1}$ it will drop abruptly to zero flux. Thus, we obtain an *S*-shaped curve for the system being modeled which is typical for example of trigger systems.[7]

The combination of all the points of stability loss (for various values of $M$) is a curve in coordinates $J$ and $\Delta p$. This curve is an analog of the spinodal for equilibrium phases.

In order to obtain the spinodal equation in the coordinates $J$ and $\Delta p$, we express $M$ from Eq. (8) and substitute into Eq. (7):

$$\Delta p=B^{-1}-\exp\left(-\frac{1}{J}\right)\left[1-\frac{1}{J}\right]. \tag{9}$$

This equation describes a curve, i.e., a set of all the spinodal points (Fig. 2).

In the presence of noise, the behavior of the system changes. Quite clearly, in the region $\Delta p_{S1}<\Delta p<\Delta p_{S2}$ the system is metastable, i.e., both possible states, being stable with respect to small perturbations, are unstable with respect to finite perturbations. In the presence of noise a transition will therefore take place from the lower curve $J=0$ to the upper curve and back. This behavior of the system is called intermittence.

Clearly, the specified interval must include a value $\Delta p=\Delta p_B$ for which both types of flow are equally probable. A parallel can be drawn between the two types of flow and the equilibrium phases (for example, for a vapor–liquid transition). The numbers $\Delta p_{S1}$ and $\Delta p_{S2}$ correspond to the spinodals of both phases and $\Delta p_B$ corresponds to the binodal.

This work was supported by the RFBR (Grant No. 98-01-00879).

[1] S. D. R. Wilson, J. Fluid Mech. **190**, 561 (1988).
[2] A. S. Skotnikov and T. B. Kholina, Khim. Promysh. No. 5, 44 (1985).
[3] V. F. Dunaĭskiĭ and N. V. Nikitin, Zh. Prikl. Mekh. Tekh. Fiz. No. 1, 49 (1980).
[4] A. I. Grigor'ev, A. A. Zemskov, and S. O. Shiryaeva, Nauch. Prib. **1**(2), 50 (1991).
[5] R. Finn, *Equilibrium Capillary Surfaces* (Springer-Verlag, New York, 1986; Mir, Moscow, 1989, 312 pp.).
[6] L. D. Landau and E. M. Lifshitz, *Fluid Mechanics*, (2nd ed. Pergamon Press, Oxford, 1987; 3rd ed., Nauka, Moscow, 1989, 733 pp.).
[7] W. Ebeling, *Strukturbildung bei Irreversiblen Prozessen* (Teubner, Leipzig, 1976; Mir, Moscow, 1979, 279 pp.).

Translated by R. M. Durham

# Growth of perfect-crystal Si–$Si_{1-x}Ge_x$–$(Ge_2)_{1-x}(InP)_x$ structures from the liquid phase

A. S. Saidov, É. A. Koshchanov, A. Sh. Razzakov, and Sh. K. Ismailov

*Physicotechnical Institute, Scientific Industrial Association ''Solar Physics,'' Uzbek Academy of Sciences, Tashkent*

(Submitted February 12, 1999)
Pis'ma Zh. Tekh. Fiz. **25**, 37–40 (December 26, 1999)

Structures comprising Si–$Si_{1-x}Ge_x$–$(Ge_2)_{1-x}(InP)_x$ with an intermediate $Si_{1-x}Ge_x$ buffer layer were grown on silicon substrates. Morphological examinations, scanning patterns and diffraction spectra, and also the electrophysical and luminescence properties of the heterostructures were used to show that the crystal perfection of these structures depends on the choice of liquid-phase epitaxy conditions. © *1999 American Institute of Physics.* [S1063-7850(99)02212-0]

It is well known that III–V semiconductors and solid solutions based on them and possessing their unique properties are among the most interesting materials for optoelectronics. Consequently, studies of the possibilities of obtaining these materials on relatively cheap substrates such as silicon are among the topical issues in semiconductor materials technology.

In Ref. 1 we showed that $(Ge_2)_{1-x}(InP)_x$ solid solutions can be obtained on silicon substrates and we described results of some preliminary investigations. In the present paper we report results of investigations to study the possibility of obtaining layers of semiconducting perfect-crystal $(Ge_2)_{1-x}(InP)_x$ substitutional solid solutions on silicon substrates with an intermediate $Si_{1-x}Ge_x$ buffer layer by epitaxial growth from an indium flux in a single growth cycle.

The layers are grown from a flux bounded by two horizontal substrates using the forced cooling method. Before growing the epitaxial layers of solid solutions, we searched the published data on the solubility of Si, Ge, and InP in various metal solvents and in various temperature ranges in order to select a suitable solvent. Since our flux is a multicomponent one, when selecting the composition we had to take into account the influence of intercomponent interaction on their solubility in the liquid phase. Since no such data are available in the literature, we carried out preliminary experiments to study the indium corner of the phase diagram of a multicomponent In–Si–Ge–InP system in order to refine the composition of the flux.

Thus, we selected a suitable In–Si–Ge–InP flux composition and temperature range to grow an $Si_{1-x}Ge_x$–$(Ge_2)_{1-x}(InP)_x$ epitaxial structure on silicon substrates in a single growth cycle. The structure was grown in the temperature range 700–850 °C and the rate of forced cooling was 1.0–1.5 deg/min.

The substrates were KÉF-grade ($n=5\times10^{17}\,cm^{-3}$) and KDB-grade ($p=1.1\times10^{17}\,cm^{-3}$) single-crystal silicon wafers ($d$ = 25–30 mm) having misorientations of between $0°15'$ and 3° relative to the [111] crystallographic direction. The thickness of the epitaxial layers varied between 15 and 25 $\mu$m depending on the crystallization initiation temperature and the growth interval, the composition of the liquid phase, the position of the substrates relative to the flux, and also the rate of forced cooling. Morphological examinations of a cleaved section of the structure and the surface of the epitaxial layers, carried out using an MIM-8M metallographic microscope, showed that other conditions being equal, mirror-smooth epitaxial layers grow on the silicon substrates having the smallest misorientation ($0^0 15'$).

The structural perfection of the as-grown layers also depended on the gap ($\delta$) between the horizontal substrates which could be varied in the range $\delta$ = 0.25–2.5 mm by using special graphite supports. The structurally most perfect layers of solid solutions were obtained on the upper and lower substrates for $\delta$ = 0.25–0.6 mm. For $\delta > 0.6$ mm the quality of the layers grown on the upper substrates deteriorated significantly. An investigation of the component distribution over the thickness of the epitaxial layer determined using a CAMECA microanalyzer showed that when a particular growth regime is maintained, an $Si_{1-x}Ge_x$ layer crystallizes initially on the silicon substrate, beginning with the silicon.

The intermediate $Si_{1-x}Ge_x$ layer then gradually gives way to a variable-gap layer of $(Ge_2)_{1-x}(InP)_x$ solid solution whose InP content increases in the direction of growth. The ratios of the $Si_{1-x}Ge_x$ and $(Ge_2)_{1-x}(InP)_x$ layer thicknesses may be varied depending on the growth conditions.

An x-ray diffraction analysis of the structural perfection of the layers using a DRON-UM1 device showed that the as-grown epitaxial layers of $Si_{1-x}Ge_x$–$(Ge_2)_{1-x}(InP)_x$ solid solutions possess extremely good single-crystal properties and extremely low stresses, as is evidenced by the absence of peaks corresponding to phases other than the initial ones on the diffraction pattern. The diffraction spectra were obtained by continuous recording using copper-anode radiation ($\lambda = 1.5418$ Å, $\lambda = 1.3922$ Å). The anode voltage and current were 30 kV and 10 mA, respectively. The exposure time was varied between 1 and 3 h. We estimated the crystal lattice constants of the substrate and the $Si_{1-x}Ge_x$ and $(Ge_2)_{1-x}(InP)_x$ epitaxial layers, which were 5.420, 5.653, and 5.743 Å, respectively (Fig. 1).

We investigated the spectral dependence of the photoluminescence at 77 K obtained from the surface of the epitaxial Si–$Si_{1-x}Ge_x$–$(Ge_2)_{1-x}(InP)_x$ structures. The edge emission band corresponded to the band gap of indium phosphide,

 © 1999 American Institute of Physics

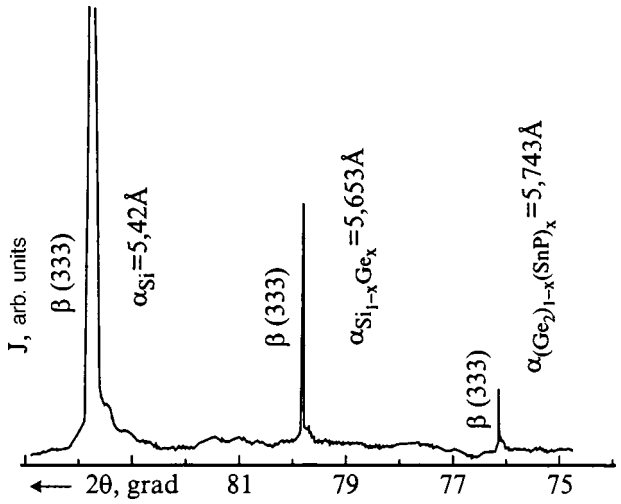


FIG. 1. Diffraction pattern of $Si–Si_{1-x}Ge_x–(Ge_2)_{1-x}(InP)_x$ heterostructures.

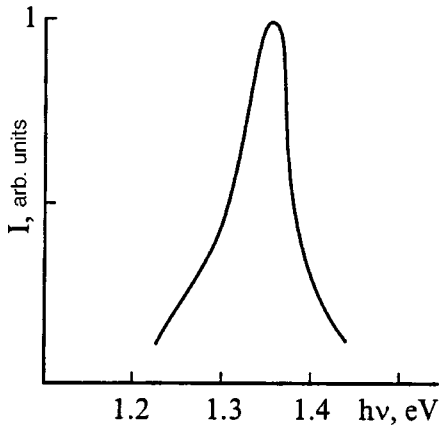


FIG. 2. Spectral dependence of the photoluminescence at 77 K obtained from the surface of $Si–Si_{1-x}Ge_x–(Ge_2)_{1-x}(InP)_x$ structures.

1.34 eV, which indicates that the surface of the epitaxial layer has an InP composition (Fig. 2).

We studied some electrophysical properties of films grown on high-resistivity substrates. We determined the resistivity, the type of conductivity, and the carrier concentration at 300 K ($\rho = 0.1–1\ \Omega \cdot$cm, $n = 2.8–5 \times 10^{17}$ cm$^{-3}$). The films possess *n*-type conductivity.

To sum up, we have shown that perfect-crystal epitaxial layers of $(Ge_2)_{1-x}(InP)_x$ solid solutions can be grown from the liquid phase on silicon substrates by suitably selecting the growth conditions.

[1] A. S. Saidov, Dokl. Akad. Nauk Uz. SSR. No. 1, 17 (1991).

Translated by R. M. Durham

# Inversion of acoustic emission asymmetry accompanying martensitic transformations in titanium nickelide alloys

V. A. Plotnikov

*Altai State University, Barnaul*
(Submitted April 16, 1999)
Pis'ma Zh. Tekh. Fiz. **25**, 41–49 (December 26, 1999)

Asymmetry of the acoustic emission indicates that the processes of nonchemical energy scattering differ in the direct and reverse martensitic transformations. An analysis of the inversion of the emission asymmetry with increasing nickel concentration in binary Ti–Ni alloys and in the course of multiple transformation cycles suggests that in a direct transformation nonchemical energy is dissipated by plastic relaxation whereas in a reverse transformation it is dissipated by dynamic relaxation. Significantly plastic relaxation degrades to saturation and dynamic relaxation begins to appear exclusively. © *1999 American Institute of Physics.* [S1063-7850(99)02312-5]

It has been reliably established experimentally that the acoustic emission produced in the course of martensitic transformations in alloys has various characteristic features: 1) the acoustic emission recorded for the direct and reverse martensitic transformations is highly asymmetric; 2) for multiple martensitic transformations the parameters of the acoustic emission are unstable.[1]

Figure 1 shows fragments of acoustic curves (the dependence of the mean-square acoustic-emission voltage recorded at the exit of a piezotransducer) obtained for a cycle of martensitic transformations in binary Ti–Ni alloys, which involves heating and cooling in a temperature range which includes the ranges for direct and reverse transformations. The direct transformation (under cooling) is a cooperative process involving rearrangement of the high-temperature $B2$ phase (CsCl-ordered body-centered cubic structure) to form the low-temperature $B19'$ phase. The transformation takes place directly as $B2 \rightarrow B19'$ in alloys having a low nickel concentration below 50.0 at.% or as $B2 \rightarrow R \rightarrow B19'$ in alloys having a nickel concentration higher than 50.0 at.% (Refs. 2 and 3). Here $R$ is a rhombohedral phase and $B19'$ is an orthorhombic phase with additional monoclinic distortion of the crystal structure. The reverse transformation (under heating) is also a cooperative process in the reverse order, i.e., $B19' \rightarrow B2$ or $B19' \rightarrow R \rightarrow B2$.

A characteristic feature of the curves plotted in Fig. 1 is the clear existence of two types of emission asymmetry for the direct and reverse martensitic transformations. The first type of asymmetry (the emission energy for the direct transformation is substantially higher than that for the reverse) is typical of alloys containing less than 51.0 at.% nickel. The second type of asymmetry (the emission energy for the reverse transformation is substantially higher than that for the direct one) is typical of alloys containing 51.0 at.% nickel. Thus, as the nickel concentration in binary Ti–Ni alloys increases, the type of asymmetry of the acoustic emission changes, i.e., an asymmetry inversion occurs.

Figure 2 gives the emission energy as a function of the number of martensitic transformation cycles for these alloys. It can be seen that the acoustic emission energy for the direct

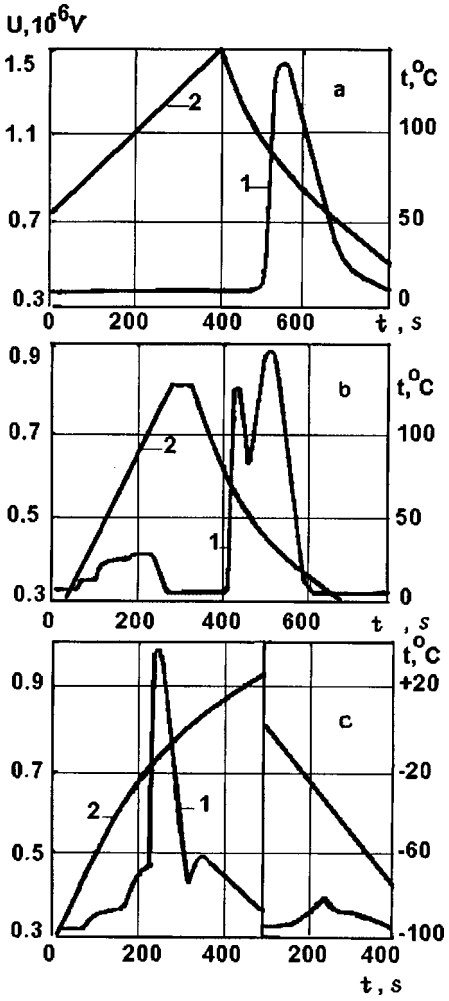


FIG. 1. Acoustic emission asymmetry during martensitic transformations in binary Ti–Ni alloys: *1* — fragments of acoustic curves, *2* — temperature line: a — Ti–49.8 at.% Ni alloy, b — Ti–50.3 at.% Ni alloy, and c — Ti–51.0 at.% Ni alloy.

 © 1999 American Institute of Physics

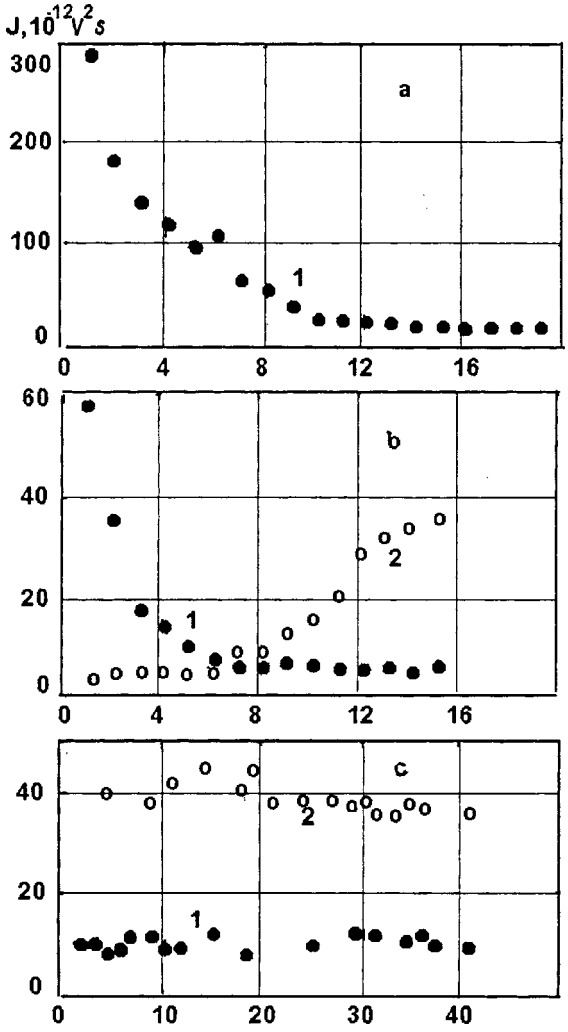


FIG. 2. Influence of cycling of martensitic transformations on the production of acoustic emission in Ti–Ni alloys: a — alloy containing 49.8 at.% Ni, b — alloy containing 50.6 at.% Ni, and c — alloy containing 51.0 at.% Ni; *1* — direct transformation; *2* — reverse transformation.

transformation decreases substantially (by approximately an order of magnitude) as the cycle number increases. For the reverse transformation, the acoustic energy increases during cycling (except for the alloy containing 49.8 at.% Ni). After an appreciable number of cycles the drop in the emission energy for the direct transformation and the increase in the emission energy for the reverse transformation reach saturation, i.e. cycling also leads to inversion of the acoustic emission asymmetry. For the alloy containing 51.0 at.% Ni, cycling barely influences the emission energy for the direct and reverse transformations, i.e., the initial asymmetry of the acoustic emission is conserved.

Thus, in experiments to record the acoustic emission we identified the following behavior: 1) two types of acoustic emission asymmetry appear; 2) inversion of the acoustic emission asymmetry occurs as the nickel concentration in the alloys increases and also in the course of multiple transformation cycles in alloys containing more than 50.0 at.% but less than 51.0 at.% nickel; 3) the initial asymmetry of the acoustic emission is conserved.

The relationship between the emission energy and the

TABLE I. Values of regression coefficients $f(\mathrm{Xi})=A+B\mathrm{Xi}$ and the coefficient $a$ (alloys initially annealed at 850 °C).

| No. | Alloy | $A$ | $B$ | $R$ | $a$ |
|---|---|---|---|---|---|
| 1 | Ti–49.8 at.% Ni | $16.9\pm0.03$ | $-0.14\pm0.04$ | 0.976 | $0.14\pm0.04$ |
| 2 | Ti–50.3 at.% Ni | $14.1\pm0.2$ | $-0.40\pm0.04$ | 0.988 | $0.40\pm0.04$ |
| 3 | Ti–50.6 at.% Ni | $15.2\pm0.2$ | $-0.48\pm0.02$ | 0.974 | $0.48\pm0.02$ |
| 4 | Ti–51.0 at.% Ni | – | – | – | – |

cycle number, at least for the direct martensitic transformation, can be fairly accurately approximated by the exponential dependence[4]

$$J_k=J_0\exp(-ak), \tag{1}$$

where $J_k$ and $J_0$ are the emission energy of the $k$th and some zeroth cycle, respectively, and $a$ is a parameter characterizing the rate of decrease in the emission energy to the saturation level. Reducing Eq. (1) to the linear form

$$\ln J_k=\ln J_0-ak, \tag{2}$$

we can determine the exponential coefficient $a$ and estimate the accuracy of approximating the experimental points by the linear dependence $f(\mathrm{Xi})=A+B\mathrm{Xi}$. Table I gives values of

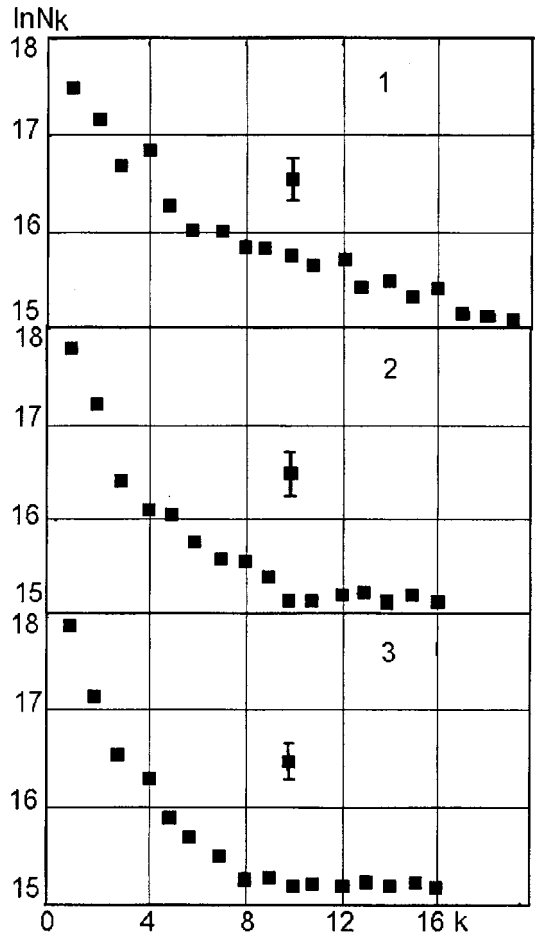


FIG. 3. Influence of multiple cycles of martensitic transformations and intermediate annealing on the production of acoustic emission in a single-crystal sample whose composition is similar to that of the alloy containing 49.8 at.% Ni: *1, 2,* and *3* — number of series of transformation cycles.

TABLE II. Comparison between acoustic emission parameters for a direct martensitic transformation and mechanical characteristics of the alloys (alloys initially quenched).

| No. | Alloy, Ni at.% | $a$ | $J_1$, $10^{-12}$ $B^2$ s/mol | Saturation cycle | $\sigma_m$, MPa | $\sigma_s-\sigma_m$, MPa | $\sigma_s$, MPa | |
|---|---|---|---|---|---|---|---|---|
| | | | | | | | 1 cycle | 11 cycles |
| 1 | 49.8 | $0.14\pm0.04$ | $26600\pm5000$ | 20 | 180 | 90 | 270 | 380 |
| 2 | 50.3 | $0.36\pm0.01$ | $5600\pm800$ | 12 | 100 | 250 | 350 | 450 |
| 3 | 50.6 | $0.63\pm0.03$ | $3400\pm770$ | 8 | 50 | 500 | 520 | 570 |
| 4 | 51.0 | − | $840\pm80$ | 0 | 30 | 930 | 960 | 960 |

the coefficients $A$ and $B$, the exponential coefficient $a$, and the correlation coefficient $R$.

It can be seen from the data presented in Table I that the experimental points can be approximated by the linear dependence (2) with a high degree of accuracy and a correlation coefficient $R$ close to one. The value of the coefficient $a$ increases with increasing nickel content in the alloys, from 0.14 in alloy No. 1 to 0.48 in alloy No. 3. The higher the coefficient $a$, the faster the curve $J_k=f(k)$ reaches saturation. It follows from this formal definition that the rate of saturation of the emission parameters in alloy No. 3 is approximately 3.5 times higher than that in alloy No. 1.

Heating the binary alloys to 600–850 °C after repeated cycles of martensitic transformations strongly influences the emission parameters in the following cycles. Figure 3 gives the integral acoustic emission parameter $N_k$ as a function of the number $k$ of transformation cycles, plotted in terms of the coordinates $\ln N_k$–$k$ for successive series of cycles and intermediate annealing using single-crystal samples whose composition is similar to that of alloy No. 1 (Ti–49.8 at.% Ni).

First, the initial acoustic emission asymmetry is restored, second the initial level of emission energy is restored, and third, after annealing the value of the coefficient $a$ in the argument of the exponential function (1) increases, which in turn reduces the number of transformation cycles required for the acoustic emission energy to reach saturation. A similar tendency was identified in polycrystalline samples of alloys Nos. 1, 2, and 3. In alloy No. 4, annealing does not change the type of acoustic emission asymmetry.

These dependences in the production of acoustic emission during a cycle of martensitic transformations are essentially related to the mechanical characteristics of the alloys, and particularly to the martensitic shear stress $\sigma_m$ and the yield point $\sigma_s$ (the dislocation yield point). Table II compares the mechanical characteristics of the alloys and the acoustic emission parameters.

It can be seen from the data presented in Table II that the higher the martensitic shear stress and the lower the yield point of the alloy, the higher is the probability of plastic relaxation (the local internal stresses reach the plastic flow stress) and the higher is the acoustic emission energy produced by a direct martensitic transformation in the first cycle. This may indicate some relationship between plastic relaxation and the production of acoustic energy in the direct martensitic transformation.

In the course of a martensitic transformation cycle, complete dislocations are generated and accumulate in the structure and an increase in the yield point is observed. This phenomenon is called phase hardening.[5] During cycling, phase hardening builds up and saturates. At the same time the acoustic emission energy produced by the direct transformation also saturates exponentially, i.e., the coefficient $a$ in the argument of the exponential function can characterize the alloy both in terms of its tendency to harden and in terms of the possibility of producing acoustic emission by plastic relaxation. Thus, the first type of acoustic emission asymmetry is strongly related to the plastic relaxation of the stresses which degrades as far as saturation during cycling.

This is confirmed by the fact that the initial acoustic emission asymmetry is restored by annealing. During heating the phase hardening is also annealed (the dislocation density and the stress fields are reduced), i.e., the structure of the alloy is transformed to its initial state. However, the increase in the coefficient $a$ during the series of transformation and annealing cycles indicates that the structure does not fully return to its initial state. The simultaneous aging process[6] changes the tendency of the alloys to plastic relaxation.

The inversion of the acoustic emission symmetry as the nickel concentration in the alloys increases to 51.0 at.% and during repeated transformation cycles indicates that two types of processes are responsible for producing the acoustic emission.

In the alloy containing 51.0 at.% Ni, the relationship between the martensitic shear stress and the yield point is such that plastic relaxation is impossible and no phase hardening was observed experimentally. Thus, the second type of acoustic emission asymmetry corresponding to asymmetry inversion predominates. It has been shown that a dynamic[7] acoustic emission mechanism strongly related to the growth–contraction microkinetics of a martensitic crystal is responsible for the second type of emission asymmetry. Unlike plastic relaxation which tends to degrade to saturation, dynamic relaxation is always present during a martensitic transformation. However, in the presence of plastic relaxation its role in the scattering of nonchemical energy during a direct martensitic transformation is only a minor one. During a reverse transformation no plastic relaxation occurs and dynamic relaxation is maximized.

[1] V. A. Plotnikov and Yu. I. Paskal', Fiz. Met. Metalloved. **84**(3), 142 (1997).
[2] D. B. Chernov, Yu. I. Paskal', V. É. Gyunter, L. A. Monasevich, and E. M. Savitskiĭ, Dokl. Akad. Nauk SSSR. **247**, 854 (1979) [Sov. Phys. Dokl. **24**, 664 (1979)].

[3] G. A. Sobyatina and V. I. Zel'dovich, Fiz. Met. Metalloved. **86**(1), 145 (1998).
[4] V. A. Plotnikov, L. A. Monasevich, and Yu. I. Paskal', Fiz. Met. Metalloved. **61**, 769 (1986).
[5] V. Ya. Erofeev, L. A. Monasevich, V. A. Pavskaya, and Yu. I. Paskal', Fiz. Met. Metalloved. **53**, 963 (1982).
[6] A. I. Lotkov and V. N. Grishkov, Izv. Vyssh. Uchebn. Zaved. Fiz. **5**, 68 (1985).
[7] V. A. Plotnikov, Pis'ma Zh. Tekh. Fiz. **24**(1), 31 (1998) [Tech. Phys. Lett. **24**, 14 (1998)].

Translated by R. M. Durham

# Influence of nitrogen on the tendency to packing defect formation and the temperature dependence of the thermoelectromotive force in Fe–Cr alloys

L. M. Kaputkina, V. V. Sumin, and K. O. Bazaleeva

*Moscow Institute of Steel and Alloys*
(Submitted April 13, 1999)
Pis'ma Zh. Tekh. Fiz. **25**, 50–54 (December 26, 1999)

The influence of nitrogen on the absolute coefficient of thermoelectromotive force in steel and the tendency of the material to form packing defects is studied. The absolute coefficient of the thermo-emf increases monotonically with increasing nitrogen concentration. The tendency to form packing defects increases monotonically with increasing nitrogen concentration in the range where the austenite solid solution is stable. Near the phase transition (austenite–martensite) this tendency increases sharply. The experiments described indicate that nitrogen influences the electron subsystem of the metal. © *1999 American Institute of Physics.* [S1063-7850(99)02412-X]

The introduction of nitrogen is an extremely promising method of modifying various properties of steel. The influence of nitrogen on the properties of iron alloys is in many respects comparable to the widely studied influence of carbon. However, many authors have noted substantial differences in the behavior of nitrogen and carbon in solid solutions of bcc and fcc iron and, specifically, different influences on the packing defect energy[1] and the nature of the interatomic bonds.[2] At the same time, specific data to estimate the structure and properties of iron–(substitutional dopant)–nitrogen solid solutions are clearly inadequate and frequently often contradictory.

In the present study we report an experimental assessment of the influence of the nitrogen concentration on properties closely related to the electron subsystem, i.e., the temperature dependence of the thermo-emf and the concentration of packing defects.

We investigated Fe–18%Cr–N alloys with nitrogen content varying between 0.42 and 1.68 wt.%.

After being quenched from 1100 °C the alloys were in various phase-structural states. Since nitrogen fairly strongly stabilizes austenite, the steel having the lowest nitrogen content, 0.42%, was in a two-phase state (martensite plus austenite) at room temperature. According to x-ray diffraction data, the sample containing 0.68% nitrogen possibly had a small quantity ($<2\%$) of martensitic phase and then, as the nitrogen content increased (0.96–1.68% N), the steel became completely single-phase and the austenite was more stable.

In order to determine the position of the nitrogen atoms in the alloy we measured the lattice period; the results are plotted in Fig. 1. It can be seen that the lattice period of the austenite increases monotonically with concentration and the slope of the curve agrees fairly accurately with the experimental data.[3,4]

This behavior is evidence that almost all the nitrogen is present in solid solution after quenching the steel.

Results of measuring the temperature dependence of the thermo-emf $E(T)$ of the alloys are plotted in Fig. 2. The measurements were made in the range 50–200 °C by an integral method[5] where the hot junction acted as the contact between the tungsten tip contained within a microfurnace and the surface of the sample. It can be seen that the slope of $E(T)$ increases monotonically with increasing nitrogen concentration. The absolute coefficient of the thermo-emf ($S=-dE/dT$) calculated using these data is plotted in Fig. 2b. The coefficient $S$ also increases with increasing nitrogen content and for pure austenitic alloys (0.94–1.68%) the dependence $S=f(N)$ is less steep and close to linear. We know that this coefficient is a function of the density of electron states at the Fermi surface ($S=\pi^2k^2T/(3|e|N_d(\varepsilon))\times(N_d(\varepsilon)/d\varepsilon)_{\varepsilon=\xi}$, where $N_d(\varepsilon)$ is the density of states as a function of energy and $\xi$ is the Fermi energy[5]) so that we are confident that this result qualitatively indicates that nitrogen influences the state of the metal electron subsystem.

The influence of nitrogen on the packing defect energy was estimated indirectly from the packing defect concentration $\alpha$ in these alloys under intensive deformation. The packing defect concentration was determined in austenite by measuring the shift of the x-ray peaks.[6] Results of numerous experiments show that, although this method does not give the correct absolute value of the packing defect energy in

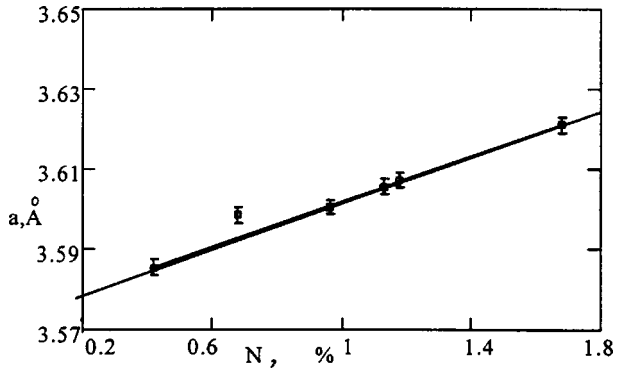


FIG. 1. Lattice period of austenitic solid solution as a function of nitrogen concentration.

 © 1999 American Institute of Physics

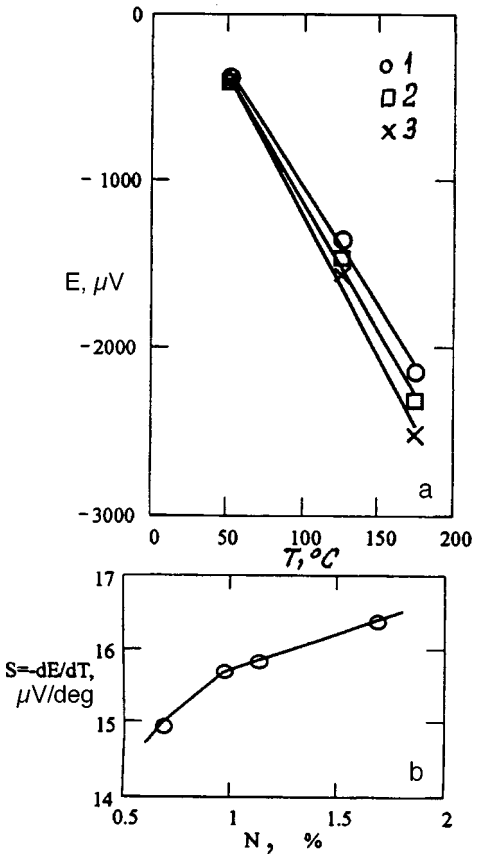


FIG. 2. Temperature dependence of the thermo-emf for alloys containing 0.677% N (*1*), 0.964% N (*2*), and 1.68% N (*3*) (a); absolute coefficient of thermo-emf (50–200 °C) for these alloys (b).

certain cases, it provides a qualitatively true reflection of the tendency to form packing defects. We assume that the packing defect energy and the inversely proportional parameter $\alpha$ in the solid solution are closely related to the density of electron states[7] so that we could predict a correlation between the values of $S$ and $\alpha$. However, the tendency to packing defect formation is also influenced by another factor, i.e., the packing defect energy decreases ($\alpha$ increases) near the

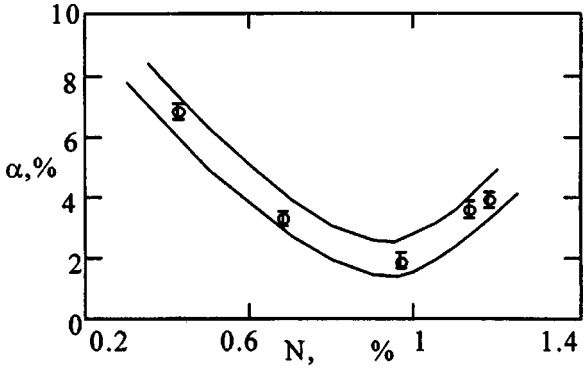


FIG. 3. Packing defect concentration for alloys having different nitrogen contents.

phase transition. Thus, in this case for two-phase alloys where the austenite solid solution is unstable (0.42 and 0.677% N) the values of $\alpha$ are exaggerated and they decrease on approaching the stable solid solution (0.964% N). The second ascending branch of the curve in Fig. 3 clearly reflects the influence of nitrogen on the electronic structure of the fcc solid solution and the increase in $\alpha$ here is caused by a reduction in the packing defect energy accompanying the nitrogen doping.

[1] R. M. Banov and G. Z. Zlateva, Izv. AN SSSR. Metall. No. 2, 176 (1977).
[2] H. Ino, K. Umezu, S. Kajiwara, and S. Uchawa, in *Proceedings of the International Conference on Martensite Transformations, Nara, Japan, 1986*, pp. 313–318.
[3] M. Hansen and K. Anderko, *Constitution of Binary Alloys*, 2nd ed. (McGraw-Hill, New York, 1958; Metallurgizdat, Moscow, 1962, 163 pp.).
[4] W. P. Pearson, *A Handbook of Lattice Spacings and Structures of Metals and Alloys* (Pergamon Press, Oxford, 1958), 258 pp.
[5] F. J. Blatt *et al.*, *Thermoelectric Power of Metals* (Plenum Press, New York, 1976; Metallurgiya, Moscow 1980, 248 pp.).
[6] Ya. D. Umanskiĭ, Yu. A. Skakov, A. N. Ivanov, and L. N. Rastorguev, *Crystallography, X-Ray Diffraction Analysis, and Electron Microscopy* [in Russian], Metallurgiya, Moscow (1982), 632 pp.
[7] Ya. D. Vishnyakov, *Packing Defects in Crystal Structure* [in Russian], Metallurgiya, Moscow (1970), 215 pp.

Translated by R. M. Durham

# Influence of defect diffusion on the radiation resistance of the heterogeneous photoconductor CdS–PbS

V. É. Bukharov and A. G. Rokakh

*N. G. Chernyshevskiĭ State University, Saratov*
(Submitted February 16, 1999)
Pis'ma Zh. Tekh. Fiz. **25**, 55–60 (December 26, 1999)

It is shown that the well-known fact that the radiation resistance of CdS improves considerably when PbS is added [A. G. Rokakh, E. V. Elagina, L. P. Matasova, and N. A. Novikova, *Composition to Fabricate Film Photoresistors*, Author's Certificate No. 1110351, publ. March 17, 1983] accompanied by the formation of the heterogeneous photoconductor CdS–PbS may be attributed to the gettering of radiation defects by narrow-gap phase inclusions. This gettering occurs because the radiation-stimulated diffusion is considerably more pronounced in the wide-gap CdS–PbS component compared with the narrow-gap component. A model is proposed to explain the radiation resistance of a CdS–PbS system and this is used to determine the steady-state defect concentration profile. © *1999 American Institute of Physics.* [S1063-7850(99)02512-4]

As we are well aware, degradation of the photoelectric and luminescence properties of II–VI compounds is caused by the formation of defects which lead to additional doping of the sample[2] and/or the establishment of new effective recombination channels.[3] It has been shown that the radiation resistance of CdS may be improved considerably by adding lead salts to the photoconductor, particularly PbS.[1] As a result of the limited mutual solubility of CdS and PbS, a heterogeneous material forms, conventionally designated CdS–PbS, which consists of a wide-gap matrix comprising a solid solution of PbS in CdS ($Pb_xCd_{1-x}S$) and narrow-gap, low-resistivity $Cd_yPb_{1-y}S$ inclusions. The presence of these inclusions is evidenced by a plasma resonance analysis of a CdS–PbS system.[1)] Since these narrow-band inclusions have low resistivity, the wide-gap matrix connected in series with the narrow-gap phase is the working material from the photoconductivity point of view.

Explanations for the radiation resistance of CdS–PbS have been forward using the idea that the recombination activity is extracted from the wide-gap to the narrow-gap phase.[4] The aim of the present study is to construct a model of the resistance of a CdS–PbS system from a slightly different point of view, based on the assumption that the diffusion of radiation defects is intensified by radiation to different degrees in the narrow-gap and wide-gap components.

The main mechanisms for radiation-stimulated diffusion were examined in Refs. 5–7. When applying these studies to CdS–PbS, we must take into account the characteristics of the material and the diffusants.

Mak[7] considered diffusion stimulated by recombination charge transfer between centers. However, formula (2) proposed by Mak only holds if each charge transfer event leads to a diffusion jump, i.e., after charge transfer the center is in an unstable position. In fact, charge transfer generally only reduces the energy barrier $U$ for defect migration by $\Delta U \approx 0.5$–$1$ eV (Ref. 8) so that in formula (2) from Ref. 7 we introduced the factor $\exp[-U-\Delta U/kT]$, where $k$ is the Boltzmann constant and $T$ is the temperature.

Stepanov[5] considered a mechanism for radiation-stimulated diffusion based on the transfer of energy to diffusing atoms as a result of particles in the radiation flux being scattered at these atoms. Since we are considering diffusion of recombination centers rather than the diffusion of atoms of the dominant material, in formula (17) from Ref. 5 we introduced the probability factor $P$ that a center will participate in a diffusion jump, which may be expressed as $P=N/N_a$, where $N$ is the concentration of centers and $N_a$ is the atomic concentration.

Vinetskiĭ and Chaĭka[6] examined the diffusion of recombination centers stimulated when the energy of free carriers is transferred to them as a result of recombination. Numerical calculations based on our own experimental data and the data given in Refs. 8–12 showed that this last mechanism of radiation-stimulated diffusion plays a dominant role in the wide-gap phase of CdS–PbS, and the coefficient of radiation-stimulated diffusion calculated for this mechanism under electron beam irradiation of $10^{13}\,\mathrm{cm^{-2}s^{-1}}$ (current density $10^{-6}\,\mathrm{A/cm^2}$, dose rate $10^6$ rad/s) is $D^*=2\times10^{-9}\,\mathrm{cm^2/s}$. This value seems fairly realistic since the experimentally determined coefficient of radiation-stimulated diffusion of the radiolysis products for x-ray irradiation of CdS at a dose rate of 250 rad/s was $D^*=10^{-12}$–$10^{-11}\,\mathrm{cm^2/s}$ (Ref. 13) and our radiation power was three orders of magnitude higher.

In the narrow-gap phase of CdS–PbS, none of these mechanisms gives any significant stimulation of diffusion. For instance, the recombination mechanism is ineffective here because of the low recombination energy which cannot exceed the band gap. This means that the field of the diffusion coefficient $D(r)$ in CdS–PbS can be considered to undergo a jump at the phase boundary.

 © 1999 American Institute of Physics

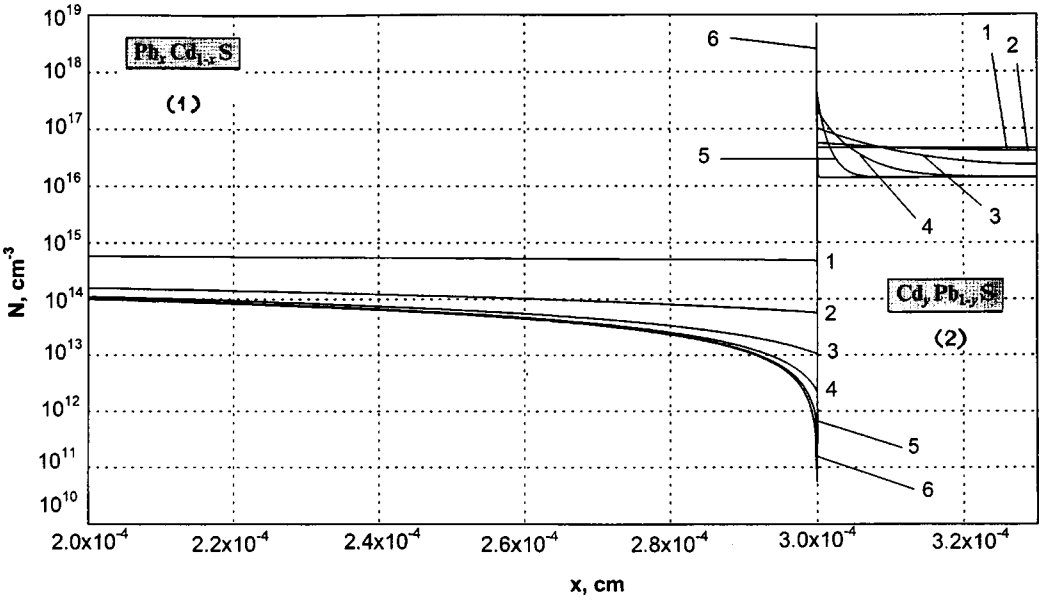


FIG. 1. Calculated profile of the steady-state concentration $N$ of defects in the heterogeneous photoconductor CdS–PbS for various rates of diffusion in the narrow-gap phase: $G=4\times10^{12}\,\mathrm{cm^{-3}\cdot s^{-1}}$, $\kappa=2\times10^{-20}\,\mathrm{cm^3\cdot s^{-1}}$, $l=3\times10^{-3}$ cm, $r=3\times10^{-5}$ cm, $D_1=10^{-9}\,\mathrm{cm^2/s}$. *1* — $D_2=10^{-11}\,\mathrm{cm^2/s}$; *2* — $D_2=10^{-12}\,\mathrm{cm^2/s}$; *3* — $D_2=10^{-13}\,\mathrm{cm^2/s}$; *4* — $D_2=10^{-14}\,\mathrm{cm^2/s}$; *5* — $D_2=10^{-15}\,\mathrm{cm^2/s}$; and *6* — $D_2=10^{-18}\,\mathrm{cm^2/s}$.

As our model problem we analyzed the generation, annihilation (recombination), and one-dimensional diffusion of defects in an infinite region where $D$ varies periodically as given by

$$D=\begin{cases} D_1, & -l+(2l+2r)k<x<l+(2l+2r), \\ D_2, & l+(2l+2r)<x<r+2l+(2l+2r), \end{cases} \quad (1)$$

where $k$ is an integer and $2l$ and $2r$ are the thicknesses of regions 1 and 2 with the diffusion coefficients $D_1$ and $D_2$ ($D_1>D_2$). This corresponds to the $Cd_xPb_{1-x}S$–$Pb_yCd_{1-y}S$ periodic superlattice under irradiation. Although strict periodicity is not always satisfied experimentally, this appreciably simplifies the analysis since on account of the symmetry we only need to analyze the region $0\leqslant x\leqslant l+r$, and the boundary conditions are simplified.

We analyzed the equation of continuity for the defects

$$\frac{\partial N}{\partial t}=D\frac{\partial^2 N}{\partial x^2}-R+G, \quad (2)$$

where $N$ is the defect concentration, $G$ and $R$ are their rates of generation and annihilation, which are given by[11]

$$G=\eta n, \quad R=\kappa N^2, \quad (3)$$

where $\eta$ and $\kappa$ are proportionality factors, and $n$ is the concentration of free electrons. The last expression in Eq. (3) implies that the concentrations of vacancies and interstitial atoms are equal.

The symmetry of $D(x)$ yields the boundary conditions

$$\partial N_1/\partial x|_{x=0}=0, \quad \partial N_2/\partial x|_{x=l+r}=0, \quad (4)$$

where the subscripts 1 and 2 refer to the corresponding regions.

In order to obtain ''matching'' conditions for the solutions at the boundary of the regions we shall analyze the defect fluxes $J_1$ and $J_2$ from the appropriate regions. By analogy with the kinetic theory of gases, we can obtain $J_i=N_i(l)v_i/6$, where the rates of displacement of the defects in the crystal are $v_i=a_i/\tau_i$ ($a_i$ is the lattice constant and $\tau_i$ is the average residence time of a defect in one of the equilibrium positions). Expressing $\nu_i$ in terms of $D_i$ [see formula (III, 6) from Ref. 8], we obtain $J_i=D_iN_i(l)/a_i$. The resultant flux $-D_1(\partial N_1/\partial x)|_{x=l}$, passing across the boundary of the regions is determined by the difference between $J_1$ and $J_2$:

$$-D_1\left.\frac{\partial N_1}{\partial x}\right|_{x=l}=D_2\left.\frac{\partial N_2}{\partial x}\right|_{x=l}=\frac{D_1}{a_1}N_1(l)-\frac{D_2}{a_2}N_2(l). \quad (5)$$

If $N_1(l)\approx N_2(l)$, $a_1\approx a_2$, and $D_1\gg D_2$, the right-hand side of Eq. (5) is positive and a flux of defects appears from region 1 to region 2, i.e., they are gettered by a narrow-gap inclusion. For a more accurate analysis we need to allow for the surface annihilation of defects which modifies condition (5).

Figure 1 gives the dependences $N(x)$ ($N_1$ and $N_2$) obtained by solving the problem (2)–(5) numerically for various values of $D_2$. It can be seen that the defect concentration in the working region (region 1) is 1.5–2.5 orders of magnitude lower than that in the gettering region and the higher the ratio $D_1/D_2$, the lower the steady-state defect concentrations in the working region, i.e., the more effective the gettering.

Thus, the radiation resistance of the heterogeneous photoconductor CdS–PbS may be attributed to the gettering of radiation defects which function as fast recombination centers, by narrow-gap, low-resistivity inclusions. This gettering occurs because the diffusion of defects in the narrow-gap and wide-gap phases of CdS–PbS is intensified by irradiation to different degrees.

[1)]The authors are grateful to N. B. Trofimova for supplying this data.

[1] A. G. Rokakh, E. V. Elagina, L. P. Matasova, and N. A. Novikova,*Composition to Fabricate Film Photoresistors* [in Russian], Author's Certificate No. 1110351, published March 17, 1983.
[2] V. T. Mak, Fiz. Tekh. Poluprovodn. **31**, 292 (1997) [*sic*].
[3] G. E. Davidyuk, N. S. Bogdanyuk, A. P. Shavarova, and A. A. Fedonyuk, Fiz. Tekh. Poluprovodn. **31**, 1013 (1997) [Semiconductors **31**, 866 (1997)].
[4] A. G. Rokakh, Pis'ma Zh. Tekh. Fiz. **10**, 820 (1984) [Sov. Tech. Phys. Lett. **10**, 344 (1984)].
[5] V. A. Stepanov, Zh. Tekh. Fiz. **68**(8), 67 (1998) [Tech. Phys. **43**, 938 (1998)].
[6] V. L. Vinetskiĭ and G. E. Chaĭka, Fiz. Tverd. Tela (Leningrad) **24**, 2170 (1982) [Sov. Phys. Solid State **24**, 1236 (1982)].
[7] V. T. Mak, Zh. Tekh. Fiz. **63**(3), 173 (1993) [Tech. Phys. **38**, 246 (1993)].
[8] B. I. Boltaks, *Diffusion and Point Defects in Semiconductors* [in Russian], Nauka, Leningrad (1972), 384 pp.
[9] R. E. Kholsted, in *Physics and Chemistry of II–VI Compounds* (Mir, Moscow, 1970), pp. 296–333.
[10] B. N. Klimov and N. M. Tsukerman, *Heterojunctions in Semiconductors* [in Russian], Saratov University Press, Saratov (1976), 180 pp.
[11] V. L. Vinetskiĭ and G. A. Kholodar', *Statistical Interaction of Electrons and Defects in Semiconductors* [in Russian], Naukova Dumka, Kiev (1969), 188 pp.
[12] A. Rose, *Concepts in Photoconductivity and Allied Problems* (Interscience, New York, 1963; Mir, Moscow, 1966, 192 pp.).
[13] V. S. Vavilov, A. E. Kiv, and O. R. Niyazova, *Mechanisms for Defect Formation and Migration in Semiconductors* [in Russian], Nauka, Moscow (1981), 368 pp.

Translated by R. M. Durham

# Superhardness of cast iron induced by copper under laser treatment

G. I. Kozlov

*Institute of Problems in Mechanics, Russian Academy of Sciences, Moscow*
(Submitted June 29, 1999)
Pis'ma Zh. Tekh. Fiz. **25**, 61–65 (December 26, 1999)

A new phenomenon has been observed, i.e., the copper-induced formation of superhard cast iron having a microhardness up to 22 000 MPa as a result of cw laser treatment of the surface of gray iron covered with a thin copper inductor layer. The induction phenomenon involves the inductor in close contact with the crystal structure specifically influencing the phase transition processes which take place in the surface layers of metals and alloys during cooling after laser treatment. © *1999 American Institute of Physics.* [S1063-7850(99)02612-9]

Laser thermal hardening is one of the most effective methods of hardening the surface of metals and alloys. A distinguishing feature of laser quenching compared with conventional methods is the highly nonequilibrium nature of the process, since the characteristic times for structural rearrangement in metals and alloys under laser treatment conditions become comparable with the heating and cooling times. From the physical point of view, the process of hardening alloys involves obtaining structures which impede the development of plastic deformation processes, i.e., creating obstacles to the migration of dislocations. In principle, this can be achieved by forming inhomogeneities in the crystal lattice of the alloys by means of impurity atoms or new-phase inclusions, and also by reducing the grain sizes.

In the present paper we report the first observation of an exceedingly interesting phenomenon, i.e., the copper-induced formation of a superhard structure in the surface layer of gray iron as a result of laser treatment of the surface on which a thin copper inductor layer had been preliminarily deposited.

For the laser treatment we used a system consisting of a 6 kW cw gas-discharge laser,[1] a focusing system, and a special device to scan the beam over the surface being treated. The intensity distribution over the beam cross section was fairly uniform in the central part of the beam with a slightly lower intensity toward the edge. A salt lens of 100 cm focal length was used to focus the laser radiation onto the surface.

At the first stage of the investigations we carried out experiments to study laser thermal hardening of gray iron samples in order to determine the optimum treatment conditions and obtain the maximum microhardness for this process. These data were important for a subsequent comparison with the results obtained using the new method of laser treatment developed in the present study. The optimum laser radiation intensity was $2\times10^4$ W/cm$^2$ which for an exposure time of 0.4 s, gives a hardened layer at least 0.8 mm deep with a microhardness in the range 8000–11 000 MPa.

The maximum microhardness of 11 000 MPa obtained for laser thermal hardening of the surface of gray iron shows good agreement with published data.[2] However, it appears that this is not the limit and superhard cast iron(!) may be obtained by using the idea of the induced action of a specific ''seed–inductor'' on the kinetics and mechanism of the phase transitions which take place during cooling of the cast iron after laser treatment. It is advisable to use copper as the inducing ''seed.''

In the experiments a thin copper layer was deposited on the surface of the gray iron immediately before the laser treatment. The layer thickness was 100–150 $\mu$m. The laser radiation power was kept constant at 5.5 kW during the treatment and the radiation intensity was selected so that the thickness of the molten layer on the surface was small and thus negligible mixing of the cast iron and copper took place in the melt. At this beam power this was achieved with a focusing spot of approximately 8 mm and a beam sweep rate over the surface of 40 cm/min.

After the laser treatment, the surface layer of copper was removed by milling to a depth of 0.5 mm (first stage) and 1.0 mm (second stage). Then, in order to reduce the influence of the deformed zone produced by the milling, a layer of around 10 $\mu$m was removed by chemical etching. The milling revealed a specular matrix which had an extremely high hardness, as was shown by the measurements. The phase composition, microstructure, and microhardness of the matrix were investigated.

The microhardness was measured over the width of the specular matrix zone using a PMT-3 tester. The values of the microhardness at the first stage reached record levels of 22 000 MPa, although the microhardness distribution over the width of the zone was slightly nonuniform and fluctuated in the range 22 000–19 000 MPa. In the deeper layer at the second stage the values of the microhardness were slightly lower but still remained high in the range 18 000–16 000 MPa which is almost unattainable for cw laser thermal hardening of cast iron.

These high values of the microhardness are undoubtedly related to the inducing influence of copper on the mechanism and kinetics of the phase transitions which take place during the cooling of cast iron after laser treatment. The structural components responsible for these high levels of microhardness need to be determined. With this aim in view, we analyzed the phase composition.

In order to study the phase composition, we compared the diffraction pattern of the treated zone with that of an

 © 1999 American Institute of Physics

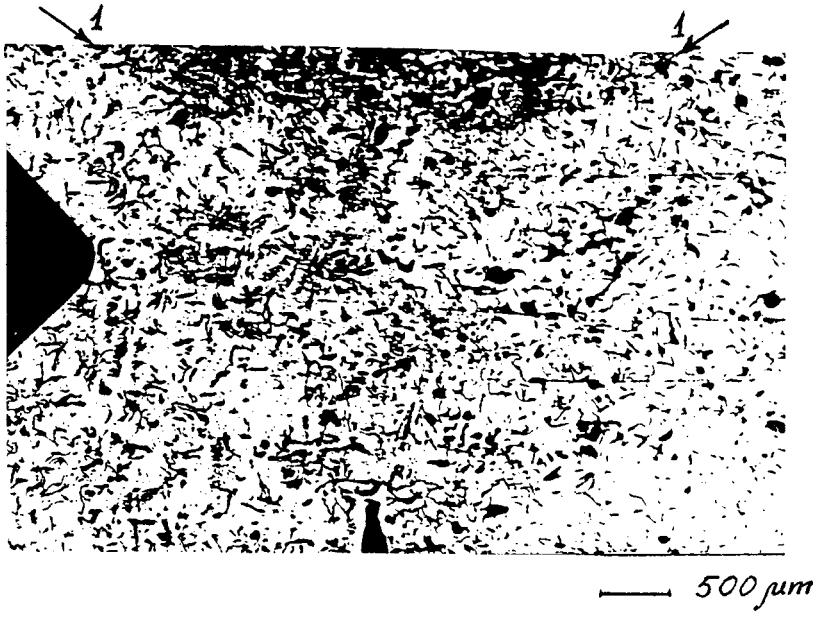


FIG. 1. Photograph of the microstructure of the specular matrix zone: *1* — boundary of molten region.

untreated zone which consisted predominantly of $\alpha$ Fe, $Fe_3C$, and carbon. The diffraction pattern obtained at the first stage from the specular matrix zone indicates that the phase composition corresponds to a mixture of ferrite, austenite, cementite, and carbon. Compared with the untreated zone, all the diffraction reflections are strongly broadened which indicates that the structure of these phase components exhibits appreciable dispersion. No distinct splitting of the diffraction reflection in the range of angles corresponding to the martensite doublet is observed. In the deeper layers (at the second stage) the reflection intensity of the martensite doublet increases and the broadening of the diffraction reflections decreases slightly. The measurements yield the important conclusion that the hardening of gray iron under laser treatment with an inducing seed is unrelated to the formation of martensite. However, the inducing influence of copper, which like $\gamma$ Fe has a face-centered cubic lattice, probably involves the copper acting as an austenite-stabilizing factor, lowering the austenite conversion temperature and thus appreciably reducing the size of the perlite formed during the cooling process. However, the reduction in the grain size may be just one of the factors responsible for the formation of superhard cast iron in these experiments.

A second important conclusion follows from a study of the microstructure which was made for the end surface of the sample. Figure 1 shows a photograph of the microstructure of the specular matrix zone which fairly clearly reveals the boundary of the molten region in which considerable release of globular-shaped carbon can be observed. In addition to the black inclusions associated with the carbon, we can also identify dark-gray regions having an acicular structure (probably bainite) and light ferrite regions containing rounded disperse cementite inclusions. However, no new structural component responsible for these high microhardness values could be detected on the basis of this analytical data.

To sum up, the formation of superhard cast iron with a record microhardness of 22 000 MPa as a result of laser treatment of the surface of gray iron on which a thin layer of copper had been previously deposited is undoubtedly related to the phenomenon of copper induction established in the present study, which influences the kinetics and mechanism of the phase transformations which take place during cooling of the cast iron after laser treatment.

[1] G. I. Kozlov and V. A. Kuznetsov, Kvantovaya Élektron. (Moscow) **16**, 1360 (1989) [Sov. J. Quantum Electron. **19**, 878 (1989)].
[2] Ya. B. Zel'dovich, G. I. Barenblatt, V. B. Librovich, and N. M. Makhviladze, *Mathematical Theory of Combustion and Explosion* [in Russian], Nauka, Moscow (1980).

Translated by R. M. Durham

# Scanning tunneling spectroscopy of amorphous carbon: tunneling model

V. I. Ivanov–Omskiĭ, A. B. Lodygin, and S. G. Yastrebov

*A. F. Ioffe Physicotechnical Institute, Russian Academy of Sciences, St. Petersburg*
(Submitted August 26, 1999)
Pis'ma Zh. Tekh. Fiz. **25**, 66–71 (December 26, 1999)

An analysis is made of a model of tunnel current flow through amorphous diamond-like carbon. It is shown that single-electron phenomena may occur in this medium which result in the appearance of specific features on the current–voltage characteristics of thin amorphous carbon films. The model is used to explain the tunnel spectra of diamond-like carbon and the size of a graphite-like cluster is estimated. © *1999 American Institute of Physics.* [S1063-7850(99)02712-3]

Amorphous carbon films initially attracted the attention of researchers because of their high mechanical strength, chemical resistance, hardness, and transparency over a broad spectral range. It has recently become apparent that these films are also promising as a material for cold cathodes because of their low field emission threshold.[1] The unique properties of amorphous carbon are associated with the characteristics of its mesoscopic structure (see, for example, Ref. 2). Amorphous carbon films consist of two mutually embedded phases, a diamond-like phase characterized by $sp^3$-hybridization of carbon atoms, a tetrahedral structure, and large (up to 4 eV) HOMO–LUMO spacing, and a graphite-like phase consisting of fragments of graphite planes and curved fullerene-like fragments. This graphite-like phase is characterized by $sp^2$-hybridization of carbon, comparatively high electrical conductivity, and a band gap which is either small or non-existent, depending on the cluster size. The diamond-like phase is usually called tetrahedral[2] to avoid confusion with diamond-like carbon which is the general term for solid carbon films. The phases are intermixed in fragments having characteristic dimensions of between a few and hundreds of angstrom. The cluster sizes in this structure have been determined in several studies, such as Ref. 3. Another important factor is that the properties of the graphite-like clusters depend very strongly on the fragment sizes of this component.

The most important method of directly studying mesoscopic structures is scanning tunneling spectroscopy, in which the tip of the tunneling microscope is fixed at a specific point above the surface of the film and the current–voltage characteristic of this tunnel structure is recorded. For materials having no mesoscopic structure the interpretation of these characteristics generally presents no difficulty. At moderate temperatures and voltages the differential conductivity of the tunnel contact is simply proportional to the product of the density of states at the Fermi level in the scanning tunneling microscope (STM) tip and the density of frees state (or for reversed polarity, filled states) in the material at a level shifted relative to the Fermi level according to the applied voltage:

$$\frac{\partial I}{\partial V} \propto \rho_{\mathrm{STM}}(E_{\mathrm{F\,STM}})\rho_{\mathrm{sam}}(V),$$

where $\rho_{\mathrm{STM}}(E_F)$ is the density of states in the STM tip at the Fermi level (it is assumed that the tip is metal and the density of states in it near the Fermi level is close to constant), and $\rho_{\mathrm{sam}}(V)$ is the density of states in the sample at the distance $V$ from the Fermi level. Having studied the function $\rho_{\mathrm{sam}}(V)$, we can use this to reconstruct the energy diagram of the density of states of the material. This approach to the study of the energy spectrum of amorphous carbon was applied in Ref. 4.

However, because of the characteristic features of the mesoscopic structure of amorphous carbon, another interpretation of the tunnel current–voltage characteristics is also possible. This is because the graphite-like clusters contained in the material are potential wells for the electrons and have sizes so small that their charging by a single electron leads to a substantial change in the electrostatic energy. Even at room temperature this change may substantially exceed $kT$. A structure consisting of a low-capacitance cluster and two tunnel junctions is called a single-electron transistor (SET).[5]

The charge at the base of this transistor can only vary in jumps with increments of the elementary charge $e$ (in an ordinary transistor this effect is suppressed by thermal noise and also by the ''spreading'' of charge because of the low resistance of the base–collector and base–emitter junctions). Thus, the conductivity of a single-electron transistor also varies abruptly (a so-called ''Coulomb staircase''). The step width of the staircase

$$\Delta\varphi = e^2/2C \tag{1}$$

corresponds to a change in the base charge by $1e$. When the base is a graphite-like cluster having characteristic dimensions of 2–3 nm (Ref. 3), its potential as a result of charging by a single electron can reach tenths of an electronvolt. An effect of this magnitude is quite noticeable even at room temperature. In particular, if the current flow path through the film contains a low-capacitance cluster separated by two tunnel junctions, the differential current–voltage characteristic will have regular steps unrelated to the overall modulation of the density of states of the material.

 © 1999 American Institute of Physics

Consequently, the classical approach and an approach associated with single-electron phenomena can be used to explain the current–voltage characteristics of amorphous carbon films. In the present paper we attempt to combine these two approaches to produce a combined model of tunnel effects in amorphous carbon.

The basic assumption of this model is that Coulomb repulsion forces in a nanosize cluster generate a correction to the electron energy at the lower edge of the conduction band in graphite-like carbon. A theoretical analysis of this possibility as applied to quantum dots was made by Averin in 1991 (Ref. 6).

Amorphous carbon films as a whole, i.e., including those containing graphite clusters, possess the band gap $E_g$ (for which their dimensions must not exceed $10^1$ nm) (Ref. 7). Assuming that in the absence of an external voltage, the Fermi level in the collector and emitter junctions, and also in the cluster is equalized, and in the cluster the Fermi level lies at the center of the band gap (which approximately corresponds to the real situation), we find that the following voltage must be applied to the transistor for the cluster to be charged by a single electron

$$U_1 = \frac{E_g}{2} + \frac{e^2}{2C}. \tag{2}$$

At the same time, when a photon is absorbed by the cluster in the fundamental absorption region, an electron–hole pair forms with zero total charge and in the optical absorption spectrum its edge will be located alongside $E_g$. The band gap is generally a macroscopic parameter so that $E_g$ for a cluster has the meaning of the HOMO–LUMO spacing. The capacitance of the cluster is determined using the formula

$$C = \varepsilon_0 \varepsilon r/2 \tag{3}$$

(a graphite-like cluster can be approximately assumed to be a flat disk of radius $r$).

Charging a cluster by an electron shifts its potential by $\Delta\varphi = e^2/2C$, and when the external voltage varies by this amount, the next differential conductivity peak appears, and so on. Thus, the first conductivity peak appears at the voltage given by formula (2) and the following peaks appear at intervals of $\Delta\varphi$. Taking into account formulas (1) and (3), which can independently determine the cluster size from these data, we can directly check the model for self-consistency.

We shall now consider the experimental tunnel spectra of amorphous carbon given in the literature. The first serious study of the tunnel spectra of amorphous carbon films was reported in Ref. 4. The graphs of the normalized differential conductivity plotted there contain clearly defined regular characteristics which begin around 1.2 V and follow at intervals of 0.4 V. The authors of Ref. 4 ascribe the characteristics visible on the differential conductivity graph to fluctuations of the density of states in the band gap and valence band of amorphous carbon. These fluctuations are possible because at low bias voltages the main contribution to the density of states is made by graphite-like clusters and their HOMO–LUMO spacing depends strongly on their size. Moreover, since these clusters generally consist of an integer number of six-membered graphite rings, this spacing varies abruptly in accordance with the following empirical formula:[7]

$$E_g\,(\mathrm{eV}) \approx 4.5/\sqrt{L}, \tag{4}$$

where $L$ is the number of rings in the cluster and this formula holds for $L < 100$. However, no quantitative explanation of the differential conductivity structure is given in Ref. 4.

The clearly defined periodic structure of the conductivity characteristics observed in Ref. 4 shows that the theory described above can be used to explain the curve profile. Numerical estimates for data given by Robertson give $E_g = 0.8$ eV and thus $L = 30$, cluster diameter 3.6 mm, $\Delta\varphi = 0.4$ eV, and $C = 2 \times 10^{-19}$ F which gives an estimate of the cluster radius of the order of 2 nm. Hence, the proposed model provides a satisfactory and noncontradictory explanation for the positions of the differential conductivity peaks on the tunnel spectra of amorphous carbon.

It should be noted that the real experimental picture differs from that assumed in the model. An STM tip has a much larger cross section than the characteristic spacing between the graphite-like carbon clusters so that several tunnel junctions could appear simultaneously beneath the tip. However, this is offset by the fact that tunneling in a disordered medium takes place initially along a single, more favorable, path (known as a puncture) whose resistance is much lower than the ambient resistance. This characteristic of tunneling in an inhomogeneous medium, of which amorphous carbon is one on the mesoscopic scale, was first considered by Raĭkh.[8] Along the length of this channel for low flowing currents the highest voltage reaches the junctions surrounding the lowest-capacitance cluster (this, like a switch, breaks the circuit when the applied voltage becomes less than $U_1$). All the other clusters presumably create an additional Ohmic correction to the resistance of the main ''working'' cluster and do not influence the form of the tunnel current–voltage characteristic. Thus, in this problem a fairly thick film can be considered to be a system with a single cluster.

This work was supported by the RFBR (Grant No. 97-02-18110).

[1] A. Hart, B. S. Satyanarayana, W. I. Milne, and J. Robertson, Appl. Phys. Lett. **74**, 1594 (1999).
[2] M.-L. Theye, V. Paret, and A. Sadki, Condens. Matter News **7**(1), 4 (1998).
[3] V. I. Ivanov–Omskii, A. B. Lodygin, S. G. Yastrebov, and V. E. Chelnokov, J. Chem. Vapor Dep. **5**, 198 (1997).
[4] C. Arena, B. Kleinsorge, J. Robertson, W. I. Milne, and M. E. Welland, J. Appl. Phys. **85**, 1609 (1999).
[5] D. V. Averin and K. K. Likharev, in *Single-electron Tunneling and Mesoscopic Devices*, edited by H. Koch and H. Lubbig (Springer-Verlag, Berlin, 1992), p. 3.
[6] D. V. Averin, A. N. Korotkov, and K. K. Likharev, Phys. Rev. B **44**, 6199 (1991).
[7] J. Robertson and E. P. O'Reilly, Phys. Rev. B **35**, 2946 (1987).
[8] M. É. Raĭkh and I. M. Ruzin, Fiz. Tekh. Poluprovodn. **19**, 1217 (1985) [Sov. Phys. Semicond. **19**, 745 (1985)].

Translated by R. M. Durham